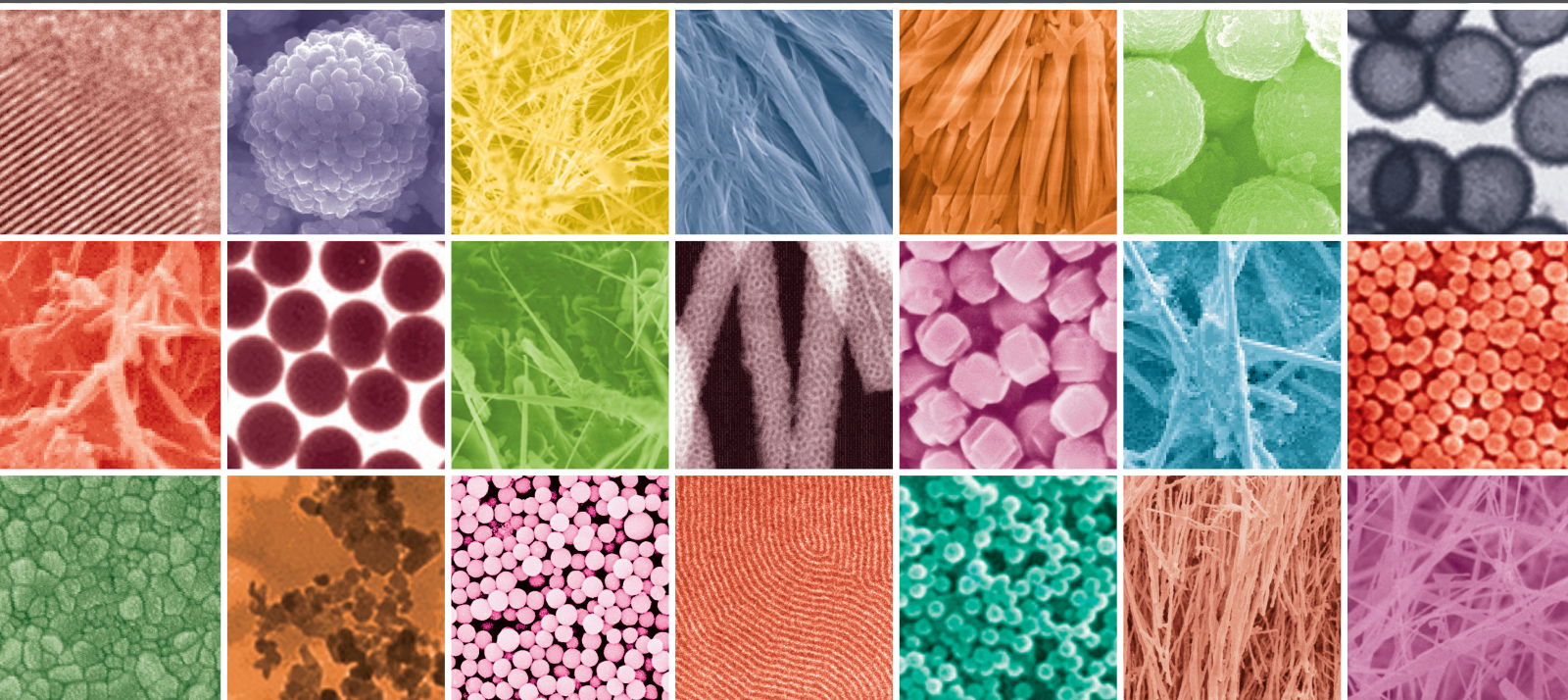


Nanomaterials for Energy Conversion and Storage

Guest Editors: Mauro Coelho dos Santos, Olivera Kesler,
and Arava Leela Mohana Reddy





Nanomaterials for Energy Conversion and Storage

Journal of Nanomaterials

Nanomaterials for Energy Conversion and Storage

Guest Editors: Mauro Coelho dos Santos, Olivera Kesler, and Arava Leela Mohana Reddy



Copyright © 2012 Hindawi Publishing Corporation. All rights reserved.

This is a special issue published in "Journal of Nanomaterials." All articles are open access articles distributed under the Creative Commons Attribution License, which permits unrestricted use, distribution, and reproduction in any medium, provided the original work is properly cited.

Editorial Board

Katerina Aifantis, Greece	Do Kyung Kim, Republic of Korea	Nairong Tao, China
Nageh K. Allam, USA	Kin Tak Lau, Australia	Titipun Thongtem, Thailand
Margarida Amaral, Portugal	Burtrand Lee, USA	Somchai Thongtem, Thailand
Xuedong Bai, China	Benxia Li, China	Alexander Tolmachev, Ukraine
Lavinia Balan, France	Jun Li, Singapore	Valeri P. Tolstoy, Russia
Enrico Bergamaschi, Italy	Xing-Jie Liang, China	Tsung-Yen Tsai, Taiwan
Theodorian Borca-Tasciuc, USA	Shijun Liao, China	Takuya Tsuzuki, Australia
C. Jeffrey Brinker, USA	Gong Ru Lin, Taiwan	Raquel Verdejo, Spain
Christian Brosseau, France	J. -Y. Liu, USA	Mat U. Wahit, Malaysia
Xuebo Cao, China	Jun Liu, USA	Shiren Wang, USA
Shafiu Chowdhury, USA	Tianxi Liu, China	Yong Wang, USA
Kwang-Leong Choy, UK	Songwei Lu, USA	Ruibing Wang, Canada
Cui ChunXiang, China	Daniel Lu, China	Cheng Wang, China
Miguel A. Correa-Duarte, Spain	Jue Lu, USA	Zhenbo Wang, China
Shadi A. Dayeh, USA	Ed Ma, USA	Jinquan Wei, China
Claude Estournes, France	Gaurav Mago, USA	Ching-Ping Wong, Hong Kong
Alan Fuchs, USA	Santanu K. Maiti, Israel	Xingcai Wu, China
Lian Gao, China	Sanjay R. Mathur, Germany	Guodong Xia, Hong Kong
Russell E. Gorga, USA	A. McCormick, USA	Zhi Li Xiao, USA
Hongchen Chen Gu, China	Vikas Mittal, UAE	Ping Xiao, UK
Mustafa O. Guler, Turkey	Weihai Ni, Germany	Shuangxi Xing, China
John Guo, USA	Sherine Obare, USA	Yangchuan Xing, USA
Smrati Gupta, Germany	Abdelwahab Omri, Canada	N. Xu, China
Michael Harris, USA	Edward Andrew Payzant, USA	Doron Yadlovker, Israel
Zhongkui Hong, China	Kui-Qing Peng, China	Ying-Kui Yang, China
Michael Z. Hu, USA	Anukorn Phuruangrat, Thailand	Khaled Youssef, USA
David Hui, USA	Suprakas Sinha Ray, South Africa	Kui Yu, Canada
Y.-Keun Jeong, Republic of Korea	Ugur Serincan, Turkey	William W. Yu, USA
Sheng-Rui Jian, Taiwan	Huaiyu Shao, Japan	Haibo Zeng, China
Wanqin Jin, China	Donglu Shi, USA	Tianyou Zhai, Japan
Rakesh K. Joshi, India	Vladimir Sivakov, Germany	Renyun Zhang, Sweden
Zhenhui Kang, China	Marinella Striccoli, Italy	Yanbao Zhao, China
Fathallah Karimzadeh, Iran	Bohua Sun, South Africa	Lianxi Zheng, Singapore
Alireza Khataee, Iran	Saikat Talapatra, USA	Chunyi Zhi, Japan

Contents

Nanomaterials for Energy Conversion and Storage, Mauro Coelho dos Santos, Olivera Kesler, and Arava Leela Mohana Reddy
Volume 2012, Article ID 159249, 2 pages

Lithium Ion Storage Characteristics of Mechanically Fractured Titanate Nanotubes, Jeongeon Kim, Minyong Eom, Yongsu Yoon, and Dongwook Shin
Volume 2012, Article ID 394089, 8 pages

Nafion Titania Nanotubes Nanocomposite Electrolytes for High-Temperature Direct Methanol Fuel Cells, Nonhlanhla Precious Cele, Suprakas Sinha Ray, and Lucky Sikkhivihilu
Volume 2012, Article ID 717913, 7 pages

Challenges Found When Patterning Semiconducting Polymers with Electric Fields for Organic Solar Cell Applications, Fernando A. de Castro, Frank Nüesch, Christian Walder, and Roland Hany
Volume 2012, Article ID 478296, 6 pages

Electrochemical Characterization of Li₄Ti₅O₁₂/C Anode Material Prepared by Starch-Sol-Assisted Rheological Phase Method for Li-Ion Battery, Zhenpo Wang, Guowei Xie, and Lijun Gao
Volume 2012, Article ID 876197, 7 pages

Influence of ITO-Silver Wire Electrode Structure on the Performance of Single-Crystal Silicon Solar Cells, Wern-Dare Jheng
Volume 2012, Article ID 654379, 7 pages

High-Efficiency CdS Quantum-Dots-Sensitized Solar Cells with Compressed Nanocrystalline TiO₂ Photoelectrodes, Yanan Wang, Ning Peng, Hongling Li, and Xuduo Bai
Volume 2012, Article ID 858693, 5 pages

Nanoporous ZnO Photoelectrode for Dye-Sensitized Solar Cell, Bayram Kılıç, Emre Gür, and Sebahattin Tüzemen
Volume 2012, Article ID 474656, 7 pages

PtRu/C Electrocatalysts Prepared Using Gamma and Electron Beam Irradiation for Methanol Electrooxidation, Dionisio F. Silva, Adriana N. Geraldes, Eddy S. Pino, Almir Oliveira Neto, Marcelo Linardi, and Estevam V. Spinacé
Volume 2012, Article ID 928230, 6 pages

Virus-Assembled Flexible Electrode-Electrolyte Interfaces for Enhanced Polymer-Based Battery Applications, Ayan Ghosh, Juchen Guo, Adam D. Brown, Elizabeth Royston, Chunsheng Wang, Peter Kofinas, and James N. Culver
Volume 2012, Article ID 795892, 6 pages

Synthesis of High-Quality Carbon Nanotube Arrays without the Assistance of Water, Yongfeng Luo, Xinjun Wang, Mengdong He, Xi Li, and Hong Chen
Volume 2012, Article ID 542582, 5 pages

Controlled Synthesis of Manganese Dioxide Nanostructures via a Facile Hydrothermal Route, Suh Cem Pang, Suk Fun Chin, and Chian Ye Ling
Volume 2012, Article ID 607870, 7 pages

Preparation and Characterization of Nano-Polyaniline Film on ITO Conductive Glass by Electrochemical Polymerization, Qi Qin and Yunxia Guo
Volume 2012, Article ID 519674, 6 pages

Editorial

Nanomaterials for Energy Conversion and Storage

Mauro Coelho dos Santos,¹ Olivera Kesler,² and Arava Leela Mohana Reddy³

¹ Laboratório de Eletroquímica e Materiais Nanoestruturados, Centro de Ciências Naturais e Humanas, Universidade Federal do ABC, Rua Santa Adélia, 166, Bairro Bangu, CEP 09210-170, Santo André SP, Brazil

² Department of Mechanical and Industrial Engineering, University of Toronto, 5 King's College Road, Toronto, ON, Canada M5S 3G8

³ Department of Mechanical Engineering and Materials Science, Rice University, Houston, TX 77005, USA

Correspondence should be addressed to Mauro Coelho dos Santos, mauro.santos@ufabc.edu.br

Received 13 November 2012; Accepted 13 November 2012

Copyright © 2012 Mauro Coelho dos Santos et al. This is an open access article distributed under the Creative Commons Attribution License, which permits unrestricted use, distribution, and reproduction in any medium, provided the original work is properly cited.

Progress [1] in the area of nanoscience and nanotechnology has pervaded almost all areas of science and technology. Over last couple of decades the ability to manipulate and control materials at an atomic and molecular level (nanometer range) and subsequent understanding of the fundamental processes at nanoscale have led to new avenues. The knowledge thus acquired can be translated into innovative processes, leading to design or fabrication of better products. More importantly, new scientific phenomena and processes have emerged that could provide either revolutionary or novel solutions to the energy, environmental, and sustainable mobility challenges that will face humanity in the 21st century.

With demand for clean and sustainable energy sources increasing at an exponential rate [1], new material technologies are being explored that could provide cost-effective and environmentally clean solutions to the world's energy problems. Developments in the areas of alternative fuels or energy storage technologies like advanced batteries, fuel cells, ultra capacitors, and biofuels are emerging as strong contenders to petroleum-based sources. Energy derived from clean and renewable sources like solar and wind power have tremendous potential, but the practical use of these sources of energy requires efficient electrical energy storage (EES) technologies that can provide uninterrupted power on demand. In all of these new technologies, nanomaterials are increasingly playing an active role by either increasing the efficiency of the energy storage and conversion processes or by improving device design and performance.

Lithium-ion batteries [2] are one of the great successes of modern materials electrochemistry. Their science and technology have been extensively reported. A lithium-ion battery

consists of a lithium-ion intercalation negative electrode (generally graphite) and a lithium-ion intercalation positive electrode (generally the lithium metal oxide, LiCoO_2), these being separated by a lithium-ion conducting electrolyte, for example, a solution of LiPF_6 in ethylene carbonate-diethylcarbonate. Although such batteries are commercially successful, we are reaching the limits in performance using the current electrode and electrolyte materials. For new generations of rechargeable lithium batteries, not only for applications in consumer electronics but especially for clean energy storage and use in hybrid electric vehicles, further breakthroughs in materials are essential, such as the use of nanomaterials devices.

Supercapacitors [2] are of key importance in supporting the voltage of a system during increased loads in everything from portable equipment to electric vehicles. There are two general categories of electrochemical supercapacitors: electric double layer capacitors (EDLC) and redox supercapacitors. In contrast to batteries, where the cycle life is limited because of the repeated contraction and expansion of the electrode on cycling, EDLC lifetime is in principle infinite, as it operates solely on electrostatic surface charge accumulation. For redox supercapacitors, some fast faradic charge transfer takes place and results in large pseudocapacitance. Progress in supercapacitor technology can benefit by moving from conventional to nanostructured electrodes. In the case of supercapacitors, the electrode requirements are less demanding than in batteries, at least in terms of electrode compaction, because power prevails over energy density. Thus, the benefits of nanopowders with their high-surface area (primary nanoparticles) are potentially more

important, hence the staggering interest in nanopowders and their rapid uptake for supercapacitor-based storage sources.

Fuel cell technologies [2] are now approaching commercialization, especially in the fields of portable power sources—distributed and remote generation of electrical energy. Already, nanostructured materials are having an impact on processing methods in the development of low-temperature fuel cells ($T < 200^{\circ}\text{C}$), the dispersion of precious metal catalysts, the development and dispersion of nonprecious catalysts, fuel reformation and hydrogen storage, and the fabrication of membrane-electrode assemblies (MEA). Polymer electrolyte membrane fuel cells (PEMFCs) have recently gained momentum for application in transportation and as small portable power sources; whereas phosphoric acid fuel cells (PAFCs), solid oxide fuel cells (SOFCs) and molten carbonates fuel cells (MCFCs) still offer advantages for stationary applications, and especially for cogeneration. Platinum-based catalysts are the most active materials for low-temperature fuel cells fed with hydrogen, reformat, or methanol. To reduce the costs, the platinum loading must be decreased (while maintaining or improving MEA performance), and continuous processes for fabricating MEAs in high volume must be developed. A few routes are being actively investigated to improve the electrocatalytic activity of Pt-based catalysts. They consist mainly of alloying Pt with transition metals or tailoring the Pt particle size.

Due to the potential applications in the field of environmental protection, the photochemistry of TiO_2 is a fast growing area both in terms of research and commercial activity [3]. Over the past decade, the level of research activity concerning TiO_2 can be appreciated through the exponential increase of relevant research literature produced (11 500 publications between 1993 and 2003) and the number of patents regarding, for instance, photocatalysis (3000 between 1996 and 2001, and more recently 2500 in Japan and 500 in USA). These features account for the intense fundamental research activity involving the scientific community. This particular interest is related to the remarkable photoactive properties of TiO_2 and therefore to its numerous applications, which are related to two main environmental priorities: environmental protection through heterogeneous catalysis (water purification, air cleaning, and self cleaning materials) and renewable energy production in photoelectrochemical solar cells, dye sensitised solar cells (DSSC). In addition to this the use of TiO_2 nanostructures has enhanced the photo electrochemical properties of these materials.

*Mauro Coelho dos Santos
Olivera Kesler
Arava Leela Mohana Reddy*

References

- [1] Jagjit Nanda Technical Expert, Materials and Nanotechnology Department Research and Advanced Engineering Ford Motor Company, USA, http://www.autofocusasia.com/production-manufacturing/nanotechnology_for_automotives.htm.

- [2] A. S. Aricò, P. Bruce, B. Scrosati, J. M. Tarascon, and W. Van Schalkwijk, “Nanostructured materials for advanced energy conversion and storage devices,” *Nature Materials*, vol. 4, no. 5, pp. 366–377, 2005.
[3] <http://www.cnrs-imn.fr/index.php/en/research-topics-ceses/nanomaterials-for-solar-energy-conversion-and-storage>.

Research Article

Lithium Ion Storage Characteristics of Mechanically Fractured Titanate Nanotubes

Jeongeun Kim,¹ Minyong Eom,² Yongsub Yoon,¹ and Dongwook Shin^{1,2}

¹Department of Materials Science and Engineering, Hanyang University, 222 Wangsimni-ro, Seongdong-gu, Seoul 133-791, Republic of Korea

²Department of Fuel Cells and Hydrogen Technology, Hanyang University, 222 Wangsimni-ro, Seongdong-gu, Seoul 133-791, Republic of Korea

Correspondence should be addressed to Dongwook Shin, dwshin@hanyang.ac.kr

Received 8 February 2012; Revised 30 July 2012; Accepted 30 July 2012

Academic Editor: Mauro Coelho dos Santos

Copyright © 2012 Jeongeun Kim et al. This is an open access article distributed under the Creative Commons Attribution License, which permits unrestricted use, distribution, and reproduction in any medium, provided the original work is properly cited.

The effect of mechanical milling on the formation of short titanate nanotube and structural change induced is investigated. Mechanical milling produces the short nanotubes with the length of 30–160 nm. The lithium ion intercalation characteristics of the obtained short titanate nanotube were studied to verify the effect of the newly formed cross-sections of nanotubes. It was found that the protonated titanate nanotubes maintained long shapes until 30 min of mechanical milling and were transformed into agglomerated nanosheets and finally anatase granules depending on the treatment duration. Through galvanostatic investigation, the nanotubes with milling of 15 min exhibited the highest discharge capacity of 336 mAh·g⁻¹ in first cycle, 12.4% larger than pristine.

1. Introduction

Nanostructured electrodes fabricated from nanotubes, nanowires, or nanofibers have shown unique rate capability for lithium ion batteries since the distance Li⁺ ions penetrate is as small as several nanometers in the radius direction which is significantly smaller than that in the usual power. As a result, there is tremendous research interest in the development of nanostructured Li-ion battery electrode with high capacity and excellent cycling stability [1–6].

Many researchers have recently prepared titanate nanotubes and developed their electrochemical properties by precise control over their morphology for various applications. It has been found that the properties of these nanomaterials depend strongly on their size and shape. Therefore, it is important to control their size and the morphology to make use of them in suitable applications. Especially much attention has been paid to nanotubes for electrochemical lithium storage due to their open, mesoporous structure, large specific surface, efficient transport of lithium ions, and impressive ion-exchange properties, which result in a high value of charge/discharge capacity [7–12].

Li et al. and Zhou et al. reported on the effect of the titanate morphology produced by changing process

parameters on the battery performance [13–16]. Bavykin et al. reported the rate of ion exchange along length of titanate nanotubes [17]. For the shortest nanotubes (having an average length ca. 50 nm), the characteristic time of the ion exchange was shorter than that for long nanotubes, suggesting that the diffusion of ions along the length of the tube could be the rate-limiting step. Although this finding was pioneering, they did not investigate the effect of titanate nanotube length on the electrochemical characteristics as an anode material for lithium battery. It is our main objective to carry out the basic estimation on the battery performance of titanate nanotubes with various lengths and verify the possibility of improving the poor cyclability of titanate nanotubes, by changing the nanotube length.

For an anode for lithium ion battery, it was confirmed that, at the first discharge stage, lithium intercalation occurred at inner and outer surface of nanotube. Some of these intercalated lithium ions could not be extracted from deep interlayer sites on inner surface of the nanotube and, hence, electrochemical reactions occur actively only at the both end of nanotubes [15, 16, 18]. In the interests of large surface area for electrochemical reaction sites of Li_xTiO₂ and short nanochannel for easy and fast transport

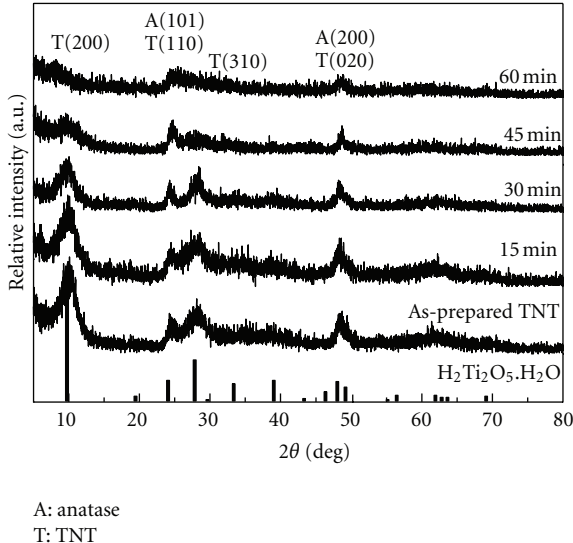


FIGURE 1: XRD patterns of the as-prepared titanate nanotubes and the produce of mechanical milling.

of Li ion for lithium intercalation, we synthesized the short length of nanotubes by low-energy mechanical milling from the hydrated titanate nanotubes synthesized via alkaline hydrothermal treatment of TiO_2 and subsequent acid treatment [19, 20]. To verify the effect of mechanical milling treatment on titanate nanotube for battery performance, the length of the titanate nanotube was controlled by various milling condition, and basic charging-discharging behavior of nanotubes as anode was estimated.

2. Experimental Methods

Titanate nanotubes were prepared by alkali hydrothermal method. Commercial titanium oxide powder (P25, Degussa AG) was used as a precursor to synthesize titanate nanotubes (TNTs). 4 g of the TiO_2 precursor and 180 mL of 10 M NaOH (98%, SAMCHUN) aqueous solution were mixed under stirring for 3 h. The suspension was poured into a Teflon vessel and placed in autoclave for hydrothermal treatment at 130°C for 24 h and cooled to room temperature. The synthesized solution was washed for 24 h with HCl (35%, DAEJUNG) acid solutions in pH 1 and then washed continuously with distilled waters to pH 7 to remove to extract sodium. The samples were filtered and dried at 60°C for 24 h. Titanate nanotubes were treated in a mechanical ball milling using identical milling parameters. The milling performed in air using a Fritsch planetary ball mill, with balls made of zirconium dioxide. The powder-to-ball weight ratio was chosen to be 1 (powder): 15 (ball), while the milling time was varied from 15 to 60 min under the rotational speed of 100 rpm.

The morphology and structural changes of titanate nanotubes with various milling conditions were characterized using BET (Surface Characterizing Analyzer, ASAP2010 & TriStar3000, USA), (X-ray diffraction XRD, Rigaku d-max 3000, Japan), (High Resolution Transmission Electron Microscopy TEM, JEM-2100F, Japan), and (Field Emission Scanning Electron Microscopy FE-SEM, Hitachi S-4800, Japan).

(Thermogravimetric-differential thermal analysis TG-DTA, TGA7, PERKIN ELMER) was performed with a temperature range of room temperature to 500°C.

For fabrication of electrodes, the active materials prepared with the mixture of carbon black, and isopropyl alcohol, and the obtained titanate nanotubes were coated on copper foil and, then, dried at 120°C for 12 hours to remove the solvents. The tests were performed on a coin-type cell assembled with as-prepared electrode, lithium metal as the counter, separator, and an electrolyte. The electrolyte solution was LiPF_6 dissolved in a mixture of EC (ethylene carbonate) and (dimethyl carbonate DMC) with the volume ration of 1 : 1.

Electrochemical properties measuring were using TOSCAT cell test instrument (Toyo system, Japan). Charge and discharge were conducted between 3 and 1 V versus Li^+ reference electrode at 0.1 C rate. Cyclic voltammogram was measured from 3 and 1 V range at $0.2 \text{ mV}\cdot\text{s}^{-1}$, using electrochemical interface (SI 1287, UK).

3. Results and Discussion

Figure 1 shows the XRD patterns of the as-prepared titanate nanotubes and the mechanically milled in condition of 100 rpm for 15, 30, 45, and 60 min. All the powders exhibited characteristic peaks at around $2\theta = 10^\circ$, 24° , and 28° , which are assigned to the diffraction of $\text{H}_2\text{Ti}_2\text{O}_5\cdot\text{H}_2\text{O}$ (JCPDS, Card 47-0124) with peak broadening by nanometer size [20–23]. It was known that the nanotubes showed weak diffraction lines because of their tubular structure and poor crystallinity [24]. The gradual changes in the major diffraction peaks suggest that the mechanical milling affected both the length and the structure of nanotubes. The intensities of main peaks at $2\theta = 10^\circ$ and 28° of titanate nanotubes were slightly decreased and broadened with increasing milling time, which suggests that nanotube structure was gradually distorted along with shortening by mechanical milling process. Unlike main peaks of nanotube, the peaks at $2\theta = 24^\circ$ and 48.5° were maintained under whole milling conditions. Plodinec et al. confirmed that during the mechanical milling treatment the phase transitions from titanate nanotubes to anatase phase and finally rutile phase were observed since the high-energy ball milling generated defects, and it influenced the composition and the stoichiometry [25]. Similar phase change was observed in this work; nanotube structure was distorted and converted into anatase phase gradually. After milling for 60 min, most of nanotubes seemed to collapse into anatase crystalline granules.

The variation of surface area of the mechanically milled product is summarized in Table 1. The surface area increases with milling and reached the highest value of $550 \text{ m}^2\cdot\text{g}^{-1}$ at 15 min and then decreases with an increase in the milling time. This is believed to be due to the agglomeration of fractured nanotubes and the anatase granules. At 60 min of milling the surface area was decreased to $273 \text{ m}^2\cdot\text{g}^{-1}$, suggesting that the highly agglomerated anatase granules were formed as supported from XRD data in Figure 1.

Figures 2 and 3 show the HRTEM and FESEM images of the titanate nanotubes. As-prepared titanate nanotubes were

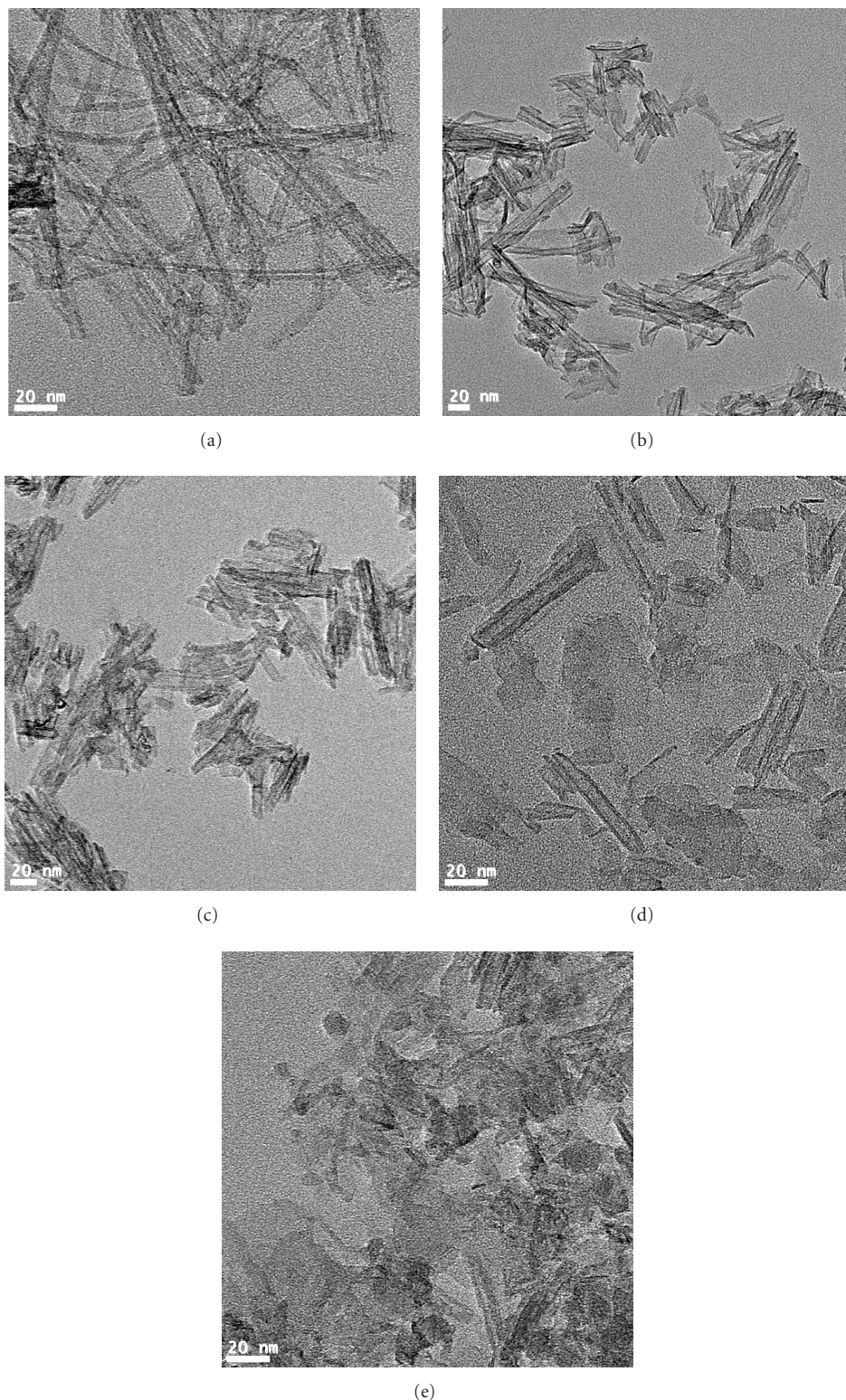


FIGURE 2: TEM images of (a) the as-prepared protonated titanate nanotubes, and the titanate nanotubes with mechanical milling in condition of (b) 15, (c) 30, (d) 45, and (e) 60 minutes at 100 rpm.

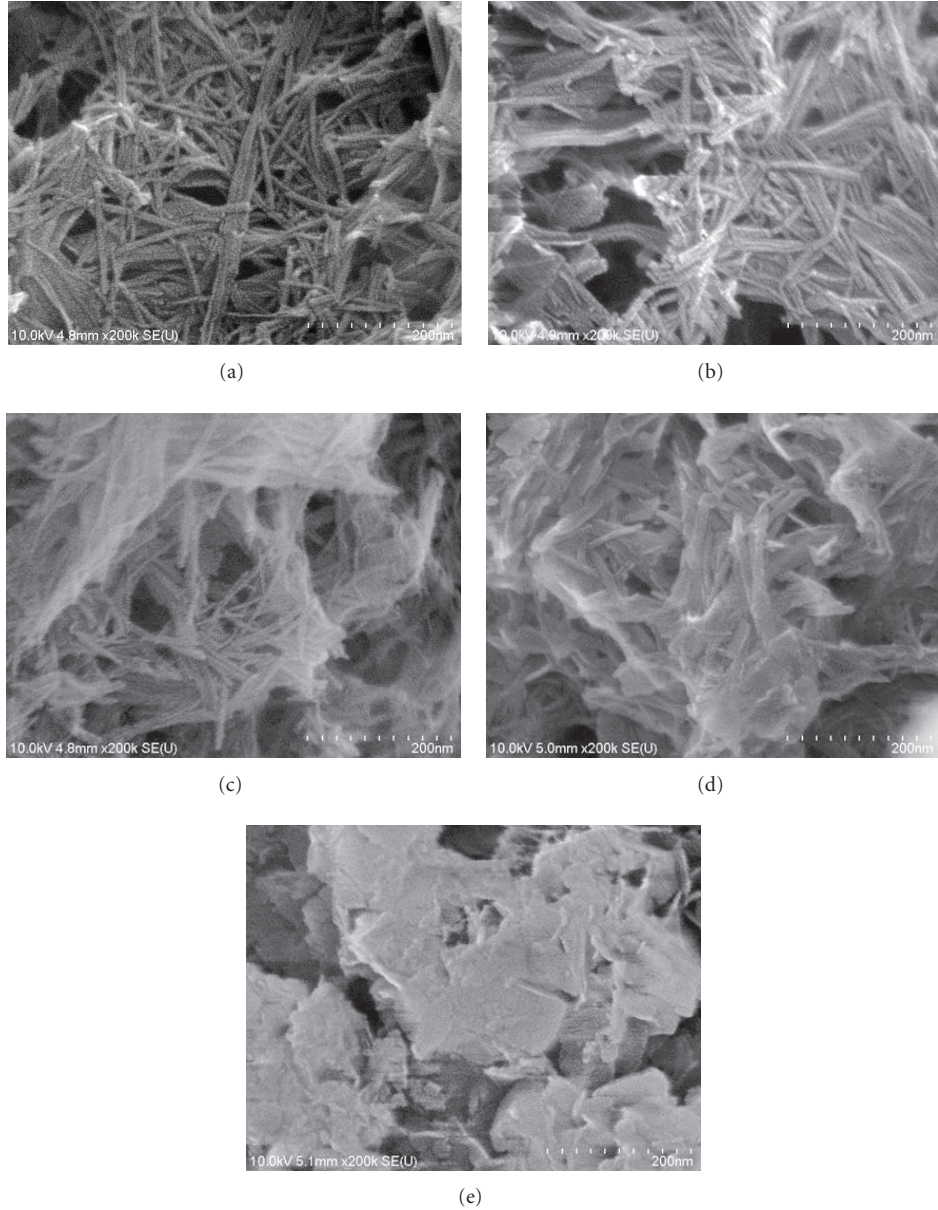


FIGURE 3: SEM images of (a) the as-prepared protonated titanate nanotubes, and the titanate nanotubes with mechanical milling in condition of (b) 15, (c) 30, (d) 45, and (e) 60 minutes at 100 rpm.

TABLE 1: Surface area of the starting material, the as-prepared, and mechanically milled.

Condition of milling (min)	P25	0	15	30	60
Surface area, S_{BET} ($m^2 \cdot g^{-1}$)	55–60	500	550	513	273

long and slim tubular shape, whose diameter was around 10 nm and length was several hundred nanometers. HRTEM image in as-prepared protonated titanate nanotubes shows that the synthesized nanotubes have 4–5 layers with open ends. The nanotubes were slightly shortened by milling for 15 min to approximately ~100 nm in length and milling for 30 min to 30–100 nm. However, the number of wall layers and the size of interspacing remained similar to

those of the as-prepared long titanate nanotubes. After 45 min, the particle type granules were observed that the titanate nanotubes were fractured and transformed to anatase particles with excessive milling treatment. XRD data in Figure 1 support that short titanate nanotubes maintained the $H_2Ti_2O_5 \cdot H_2O$ structure up to 30 min of milling. Figure 3 shows that the partial change of powder morphology took place with milling treatment. It is clear that the degree of agglomeration is slightly intensified with milling time. After 60 min, tubular type morphology is not shown as TEM image, and anatase granules were agglomerated by increased treatment duration.

Figure 4 shows the initial charge/discharge behavior of lithium intercalation in the titanate nanotubes before

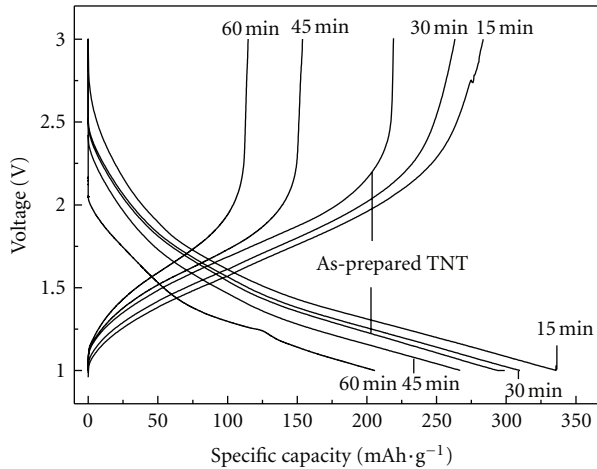


FIGURE 4: Initial charge/discharge profile of titanate nanotubes with the milling condition of 0, 15, 30, 45 and 60 minutes at a current rate of $10 \text{ mA}\cdot\text{g}^{-1}$ between 1.0 and 3.0 V.

and after milling treatments at current rate of $10 \text{ mA}\cdot\text{g}^{-1}$ between 1.0 V and 3.0 V. The initial discharge capacities were varied from $335 \text{ mAh}\cdot\text{g}^{-1}$ to $210 \text{ mAh}\cdot\text{g}^{-1}$, and initial charge capacities were varied from $280 \text{ mAh}\cdot\text{g}^{-1}$ to $114 \text{ mAh}\cdot\text{g}^{-1}$ depending on milling duration. As-prepared titanate nanotubes exhibited the initial charge and discharge capacity of $219 \text{ mAh}\cdot\text{g}^{-1}$ and $299 \text{ mAh}\cdot\text{g}^{-1}$, respectively, with a reversible efficiency of 73.2%. However, charge and discharge capacities were increased to $280 \text{ mAh}\cdot\text{g}^{-1}$ and $336 \text{ mAh}\cdot\text{g}^{-1}$ for milling of 15 min with a reversible efficiency of 83.3%. After milling of 15 min, the capacities rapidly decreased with increasing milling time. One can see that morphological and structural change, controlling the length of titanate nanotubes, seems to have a noticeable effect on the cell performance. At the initial stage of milling treatment, long nanotubes were fractured into short nanotube that had the highest value of surface area for the absorption of Li ion and short nanochannel for easy and fast transfer of Li^+ for lithium intercalation. Further milling treatment, however, starts to produce nanosheets with lower intercalation capability. Due to the increase of less active phases, even though nanotubes are shorten further, the charge/discharge capacities decrease. After 30 min of milling, the nanotubes transformed to anatase granular structure, and consequently a distinguishing characteristic of nanotubes was disappeared.

Figure 5 shows the cyclic voltammograms of the samples at a scan rate of $0.2 \text{ mV}\cdot\text{s}^{-1}$. In the first cycle, there is only a pair of broad redox peaks for nanotubes as prepared and milling 13 and 30 min. The pseudocapacitive behavior of this peak is explained in terms of the interaction taking place on the nanosheet surface, hence curved one. The TiO_2 nanotubes hold the curved nanosheet-like morphology with thin-wall structure and high specific surface area.

In the case of the nanotubes with milling 45 min, a pair of shoulder redox peaks near the larger broad redox peaks appears at 1.75 and 1.95 V (versus Li^+/Li , depending on the scan rate), which is characteristic for lithium insertion into anatase lattice, revealing the possible phase transition from titanate to anatase. Obviously, the pair of shoulder

redox peaks related to lithium insertion/extraction in anatase becomes larger with increasing milling time, accompanied by a decrease of the broad redox peaks and a structural transformation from titanate to anatase [26].

Figure 6 shows the galvanostatic charge/discharge recyclability for the titanate nanotube and the materials produced by milling treatments. The cutoff potentials for the charge/discharge were set to be 1.0 V to 3.0 V versus Li^+/Li . All samples exhibited an obvious drop of discharge capacity during first several cycles that may be due to the formation of LiO_2 or LiOH by left remained water in nanotubes on the surface of electrode [27]. The electrochemical discharge capacities of titanate nanotubes with milling decreased gradually and showed poor cycle stability for lithium insertion and extraction compared to nanotube. In spite of highest value of initial charge and discharge capacities, the short titanate nanotubes produced by milling contain defects in composition and structure, and these defects cause irreversible capacities accumulating every cycles.

4. Conclusion

Titanate nanotubes were synthesized by the hydrothermal method and treated in a high-energy ball milling in various duration conditions. The structure of nanotubes was $\text{H}_2\text{Ti}_2\text{O}_5\cdot\text{H}_2\text{O}$ with inner and outer diameter of 5 nm and 10 nm. Increasing milling duration, the titanate nanotubes were fractured into short length of nanotubes, and finally transformed to anatase structure. The 15 min sample shows that high initial charge and discharge capacities of $280 \text{ mAh}\cdot\text{g}^{-1}$ and $336 \text{ mAh}\cdot\text{g}^{-1}$ observed in the titanate nanotube, which shows an effect of shorted titanate nanotubes. The length of nanotubes had an effect on cell performance due to high specific surface area for absorption of Li ion and short nanochannel for easy and fast transfer of Li^+ for lithium intercalation; however, the cyclic stability was not greatly improved because of structural and compositional defects caused by high-energy ball milling. Further study is required the synthesis of short nanotube without structural

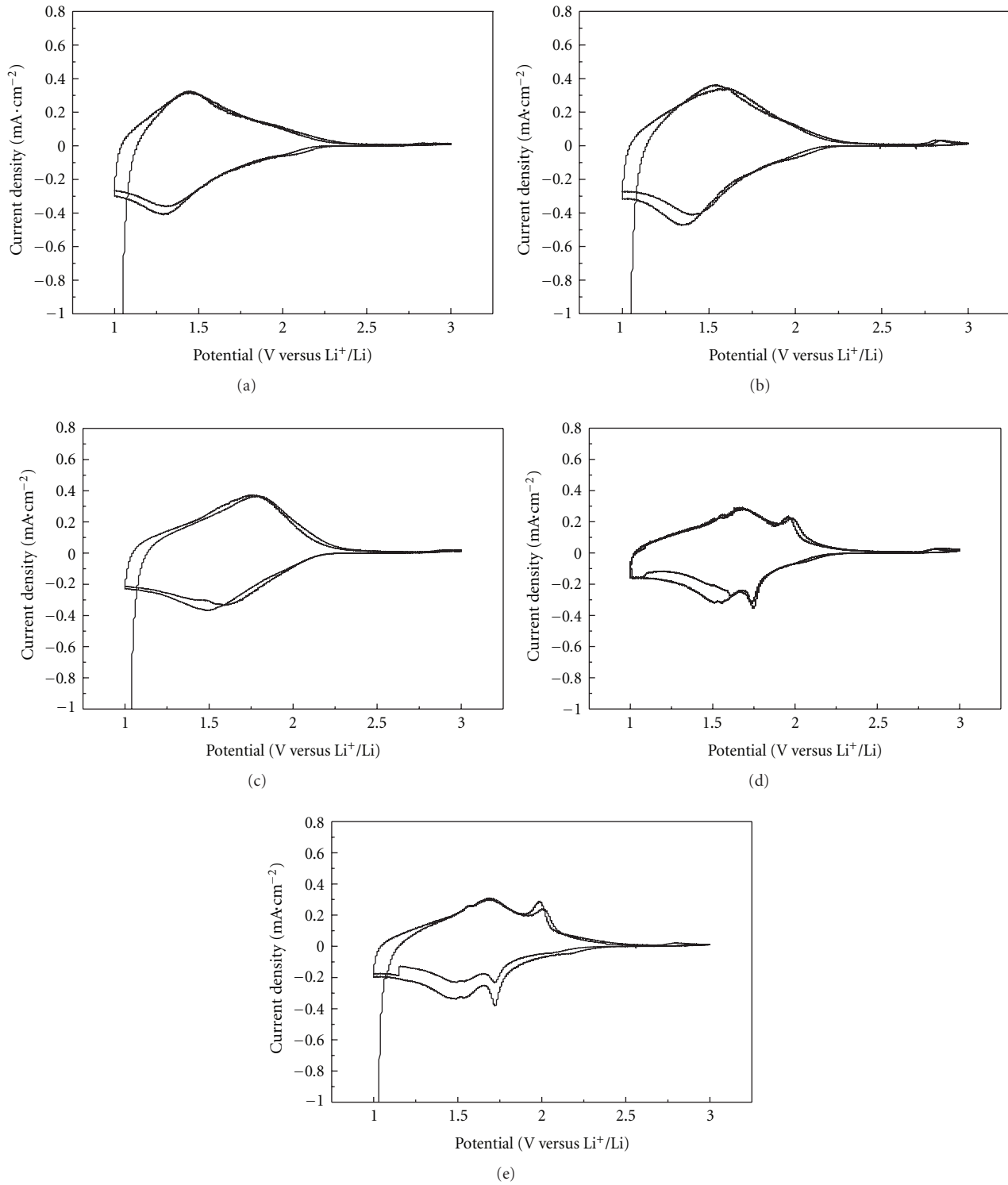


FIGURE 5: Cyclic voltammogram plots of TiO_2 nanotube electrodes (a) and with mechanical milling in condition of (b) 15, (c) 30, (d) 45, and (e) 60 minutes at $0.2 \text{ mV}\cdot\text{s}^{-1}$.

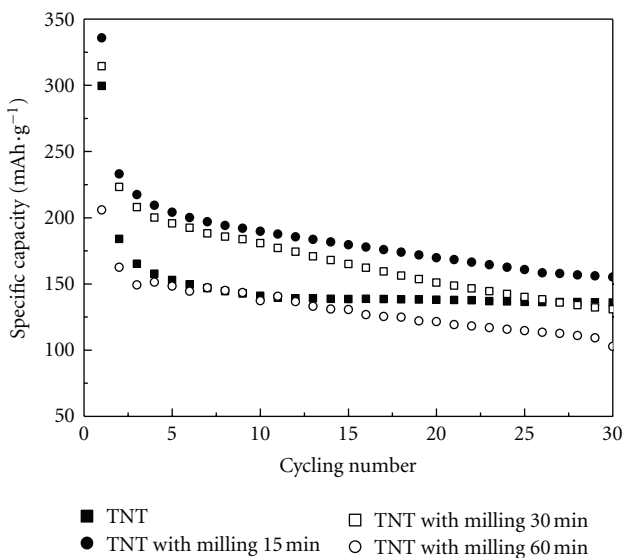


FIGURE 6: Charging-discharging curves of the coin cell composed of titanate nanotubes//1 M LiPF₆-EC/DEC//Li metal at a current rate of 10 mAh·g⁻¹ between 1 V and 3 V. The titanate nanotubes with the milling condition of 0, 15, 30, and 60 minutes were used as an anode-active materials.

change and defect, which can solve the problems of low initial capacity and poor cyclability of titanate nanotubes.

Acknowledgments

This research was supported by a grant from the Fundamental R&D Program for Core Technology of Materials funded by the Korean Ministry of Knowledge Economy (Grant no. 10037233).

References

- [1] T. Kasuga, M. Hiramatsu, A. Hoson, T. Sekino, and K. Niihara, "Formation of titanium oxide nanotube," *Langmuir*, vol. 14, no. 12, pp. 3160–3163, 1998.
- [2] D. S. Seo, J. K. Lee, and H. Kim, "Preparation of nanotube-shaped TiO₂ powder," *Journal of Crystal Growth*, vol. 229, no. 1, pp. 428–432, 2001.
- [3] Y. Q. Wang, G. Q. Hu, X. F. Duan, H. L. Sun, and Q. K. Xue, "Microstructure and formation mechanism of titanium dioxide nanotubes," *Chemical Physics Letters*, vol. 365, no. 5–6, pp. 427–431, 2002.
- [4] X. Zhang, B. Yao, L. Zhao, C. Liang, L. Zhang, and Y. Mao, "Electrochemical fabrication of single-crystalline anatase TiO₂ nanowire arrays," *Journal of the Electrochemical Society*, vol. 148, no. 7, pp. G398–G400, 2001.
- [5] Z. Y. Yuan, J. F. Colomer, and B. L. Su, "Titanium oxide nanoribbons," *Chemical Physics Letters*, vol. 363, no. 3–4, pp. 362–366, 2002.
- [6] J. J. Wu and C. C. Yu, "Aligned TiO₂ nanorods and nanowalls," *Journal of Physical Chemistry B*, vol. 108, no. 11, pp. 3377–3379, 2004.
- [7] X. P. Gao, Y. Lan, H. Y. Zhu et al., "Electrochemical performance of anatase nanotubes converted from protonated titanate hydrate nanotubes," *Electrochemical and Solid-State Letters*, vol. 8, no. 1, pp. A26–A29, 2005.
- [8] J. Li, Z. Tang, and Z. Zhang, "Preparation and novel lithium intercalation properties of titanium oxide nanotubes," *Electrochemical and Solid-State Letters*, vol. 8, no. 6, pp. A316–A319, 2005.
- [9] J. Li, Z. Tang, and Z. Zhang, "H-titanate nanotube: a novel lithium intercalation host with large capacity and high rate capability," *Electrochemistry Communications*, vol. 7, no. 1, pp. 62–67, 2005.
- [10] G. Armstrong, A. R. Armstrong, J. Canales, and P. G. Bruce, "Nanotubes with the TiO₂-B structure," *Chemical Communications*, no. 19, pp. 2454–2456, 2005.
- [11] G. Armstrong, A. R. Armstrong, J. Canales, and P. G. Bruce, "TiO₂ (B) nanotubes as negative electrodes for rechargeable lithium batteries," *Electrochemical and Solid-State Letters*, vol. 9, no. 3, pp. A139–A143, 2006.
- [12] Z. W. Zhao, Z. P. Guo, D. Wexler, Z. F. Ma, X. Wu, and H. K. Liu, "Titania nanotube supported tin anodes for lithium intercalation," *Electrochemistry Communications*, vol. 9, no. 4, pp. 697–702, 2007.
- [13] Y. K. Zhou, L. Cao, F. B. Zhang, B. L. He, and H. L. Li, "Lithium insertion into TiO₂ nanotube prepared by the hydrothermal process," *Journal of the Electrochemical Society*, vol. 150, no. 9, pp. A1246–A1249, 2003.
- [14] J. Li, Z. Tang, and Z. Zhang, "Preparation and novel lithium intercalation properties of titanium oxide nanotubes," *Electrochemical and Solid-State Letters*, vol. 8, no. 6, pp. A316–A319, 2005.
- [15] J. Li, Z. Tang, and Z. Zhang, "Controllable formation and electrochemical properties of one-dimensional nanostructured spinel Li₄Ti₅O₁₂," *Electrochemistry Communications*, vol. 7, no. 9, pp. 894–899, 2005.
- [16] J. Li, Z. Tang, and Z. Zhang, "Pseudocapacitive characteristic of lithium ion storage in hydrogen titanate nanotubes," *Chemical Physics Letters*, vol. 418, no. 4–6, pp. 506–510, 2006.
- [17] D. V. Bavykin, V. N. Parmon, A. A. Lapkin, and F. C. Walsh, "The effect of hydrothermal conditions on the mesoporous structure of TiO₂ nanotubes," *Journal of Materials Chemistry*, vol. 14, no. 22, pp. 3370–3377, 2004.
- [18] D. H. Kim, J. S. Jang, S. S. Han et al., "High electrochemical Li intercalation in titanate nanotubes," *Journal of Physical Chemistry C*, vol. 113, no. 31, pp. 14034–14039, 2009.
- [19] X. Sun and Y. Li, "Synthesis and characterization of ion-exchangeable titanate nanotubes," *Chemistry*, vol. 9, no. 10, pp. 2229–2238, 2003.
- [20] Q. Chen, W. Zhou, G. Du, and L. Peng, "Trititanate nanotubes made via a single alkali treatment," *Advanced Materials*, vol. 14, no. 17, pp. 1208–1211, 2002.
- [21] A. R. Armstrong, G. Armstrong, J. Canales, and P. G. Bruce, "TiO₂-B nanowires," *Angewandte Chemie*, vol. 43, no. 17, pp. 2286–2288, 2004.
- [22] R. Ma, Y. Bando, and T. Sasaki, "Nanotubes of lepidocrocite titanates," *Chemical Physics Letters*, vol. 380, no. 5–6, pp. 577–582, 2003.
- [23] Z. Y. Yuan and B. L. Su, "Titanium oxide nanotubes, nanofibers and nanowires," *Colloids and Surfaces A*, vol. 241, no. 1–3, pp. 173–183, 2004.
- [24] L. Qian, Z. L. Du, S. Y. Yang, and Z. S. Jin, "Raman study of titania nanotube by soft chemical process," *Journal of Molecular Structure*, vol. 749, no. 1–3, pp. 103–107, 2005.

- [25] M. Plodinec, I. Friščić, D. Iveković et al., “The mechanochemical stability of hydrogen titanate nanostructures,” *Journal of Alloys and Compounds*, vol. 499, no. 1, pp. 113–120, 2010.
- [26] L. Kavan, M. Kalbáč, M. Zukalová et al., “Lithium storage in nanostructured TiO₂ made by hydrothermal growth,” *Chemistry of Materials*, vol. 16, no. 3, pp. 477–485, 2004.
- [27] H. Zhang, G. R. Li, L. P. An, T. Y. Yan, X. P. Gao, and H. Y. Zhu, “Electrochemical lithium storage of titanate and titania nanotubes and nanorods,” *Journal of Physical Chemistry C*, vol. 111, no. 16, pp. 6143–6148, 2007.

Research Article

Nafion Titania Nanotubes Nanocomposite Electrolytes for High-Temperature Direct Methanol Fuel Cells

Nonhlanhla Precious Cele,¹ Suprakas Sinha Ray,² and Lucky Sikhwivhilu³

¹ Department of Electrical Engineering, Centre for Energy and Electric Power, Tshwane University of Technology, Staartelitelite Road, Pretoria 0001, South Africa

² DST/CSIR Nanotechnology Innovation Centre, National Centre for Nano-Structured Materials, Council for Scientific and Industrial Research, 1-Meiring Naude Road, Brummeria, Pretoria 0001, South Africa

³ Advanced Materials Division, DST/Mintek Nanotechnology Innovation Centre, Mintek, Private Bag X3015, Randburg, Johannesburg 2125, South Africa

Correspondence should be addressed to Nonhlanhla Precious Cele, nonhlanhla.cele@gmail.com

Received 10 November 2011; Revised 15 May 2012; Accepted 22 May 2012

Academic Editor: Mauro Coelho dos Santos

Copyright © 2012 Nonhlanhla Precious Cele et al. This is an open access article distributed under the Creative Commons Attribution License, which permits unrestricted use, distribution, and reproduction in any medium, provided the original work is properly cited.

Nafion-based nanocomposite membranes containing various amounts of titania nanotubes (TNTs) as an inorganic filler have been prepared using melt-mixing method and have been investigated for proton exchange membrane applications. The one-dimensional TNTs have been prepared from potassium hydroxide using hydrothermal route and conventional heating. Nafion R1100 in a protonated form was used, and TNT contents were in a range of 0.5–2.0 wt%. The acid-treated composite membranes, at lowest inorganic additive content, exhibited improved properties in terms of thermal stability and methanol (MeOH) permeability. The best performing nanocomposite was the membrane containing only 0.5 wt% TNTs showing ionic conductivity value of $7.2 \times 10^{-2} \text{ S} \cdot \text{cm}^{-1}$ at 26°C and 100% of relative humidity.

1. Introduction

Currently, titanium dioxide (TiO_2) or titania-derived nanotubes (TNTs) are examined in respect with their possible prominent applications such as catalyst supports [1], photocatalyst [2], gas sensing elements [3], and anode materials for batteries [4]. Titanium-dioxide-supported noble metal catalysts, such as gold [5], silver, or platinum [6, 7], are effective in many important processes, such as selective oxidation and hydrogenation and automobile engine exhaust systems [8].

Principal advantages of the nanotubular form seem to be related to the property that they have high specific surface area, which allows diffusion of active species. The crystal structure of TNTs seems to be a derivative for many photocatalytic applications. Another property is that TNTs are often open at the end and accessible for the interaction with gaseous substances. The TNTs are also thermally stable up to 600°C [6–9]. These are some of the essential criteria for fuel cell electrolytes membranes. This promotes to study

the Nafion/TNTs nanocomposite membranes behaviour with the aim to improve Nafion properties such as fuel permeability and thermal and mechanical stability.

Nafion, whose primary structure consists of acid tipped side chains dangling from a perfluorinated backbone, is expected to be compatible with TNTs, due to its reactive nature. The metal ions present in TNTs such as K^+ is expected to increase thermal stability of Nafion membrane. The resistance of TNTs in presence of H_2 is likely to improve swelling and mechanical properties of Nafion membranes at higher temperatures greater than 100°C. Therefore, to understand the effect of the interactions between Nafion and TNTs on the proton exchange membrane properties, further investigations were carried out. In this study, the effects of TiO_2 nanotubes on Nafion properties such as water uptake, thermal stability, methanol (MeOH) permeability, and ion conductivity were investigated. The nanocomposite membranes were prepared using melt-extrusion method by varying the nanofiller loadings. The mechanical, thermal properties, and ionic conductivity of membranes were

investigated using dynamic mechanical analyser (DMA), thermogravimetric analyser (TGA), and electrochemical impedance spectroscopy (EIS). The vibration studies were carried out by FTIR spectroscopy, providing information on the nanofiller/Nafion, nanofiller/H₂O, Nafion/H₂O interactions, and the conformation of fluorocarbon chains of Nafion hydrophobic domains. Methanol permeability was also investigated using the gas chromatography.

2. Experimental Details

2.1. Materials. Nafion precursor (R1100) was obtained from Ion Power. Potassium hydroxide (KOH) and titanium dioxide powder was purchased from Merck chemicals and used as received.

2.2. Synthesis of TiO₂ Nanotubes. TiO₂-derived nanotubes (TNTs) were synthesized using a procedure described elsewhere [9–11]. In a typical procedure about 23 g of TiO₂ powder, P25 Degussa, was mixed with 200 mL of 18 M of aqueous solution of KOH. The mixture was heated at 150°C in an autoclave with constant stirring for 24 hours. The product was then washed with deionized water and then dried in an oven at 120°C for 14 hours.

2.3. Membrane Preparation. The TNTs were used as filler during the preparation of polymer nanocomposite membranes. The nanocomposite membranes were prepared by melt-extrusion method using a microextruder Reomix OS (HAAKE) instrument. Nafion (R1100) and TNTs were melt-mixed at 250°C at a rotor speed of 60 rpm for 10 min. The TNTs were added after 2 min of melting Nafion inside the extruder. For each nanocomposite, the amount of TNTs loaded was varied from 0.5 to 2.0 wt% to study the effect of TNTs loading on the properties of Nafion. The nanocomposites samples were then converted into sheets or films with a thickness of about 0.2 mm using a Carver laboratory press at 2 MPa and 250°C. The nanocomposites were then hydrolysed, to introduce cation exchange properties into the membranes. The nanocomposites were immersed in a mixture of 15 wt% potassium hydroxide, 50 wt% of deionized water, and 35 wt% of dimethyl-sulfoxide at 80°C for 2 hours. This was followed by the repeated immersion (three times) in a fresh 3 M nitric acid (HNO₃) for 1 h to complete protonation process.

2.4. Characterisation Techniques

2.4.1. Scanning Electron Microscopy (SEM). Dry membranes were manually fractured after cooling in liquid nitrogen, to expose their cross section. The morphology of the fractured sample surfaces was analysed using SEM (LEO 1525), operating at an accelerating voltage of 3–10 kV.

2.4.2. The Fourier Transform Infrared. FTIR spectroscopy 800 from Perkin Elmer that was used to study the elementary composition of the nanocomposites studies were carried out from 500 to 4000 cm⁻¹.

2.4.3. X-Ray Diffraction. XRD patterns were measured on a Phillips X'Pert diffractometer using secondary graphite monochromatic CuK α radiation ($\lambda = 1.54060 \text{ \AA}$) at 40 kV/50 mA. Measurements were taken using angle of incidence detector at an angle of 2°, for 2θ values over 10–70° in steps of 0.05°.

2.4.4. The Thermogravimetric Analysis. TGA was conducted on a TGA Q500 (TA Instruments) at a heating rate of 10°C/min in air, from room temperature to 800°C.

Mechanical properties of pure Nafion and its TNTs containing composite membranes were studied by a Perkin Elmer DMA 8000 in the dual cantilever bending geometry. The temperature dependence of loss tangent ($\tan \delta$, loss modulus/storage modulus) of all samples were measured at a constant frequency of 1 Hz with the strain amplitude of 0.02% from room temperature to 180°C with a heating rate of 2°C/min.

2.4.5. Electrical Conductivity. The electrical resistivity was measured at room temperature using the four point collinear probe method. The equidistant tungsten carbide probes have a separation distance (s) and probe radius of 0.127 cm and 0.005 cm, respectively. The 1 × 1 cm² samples were prepared with a thickness of about 0.2 cm. The Keithley 4200-SCS Semiconductor Characterisation System, equipped with four supply and measure units (SMUs) and an amplifier, was used to perform high-precision direct current characterisation by supplying currents ranging from 1 fA to 1 mA. The resistivity changes as a function of probe spacing (0.127 cm) and is given by:

$$\rho = 2\pi s \frac{V}{I}, \quad \text{for } t \gg s, \quad (1)$$

where V is the measured voltage, I is the supplied current, and t is the thickness of the films [10, 12]. The electrical conductivity is then given by

$$\sigma = \frac{1}{\rho}. \quad (2)$$

2.4.6. Electrochemical Impedance. Proton conductivity of fuel cell membrane was measured using a galvanostatic four-point probe AC electrochemical impedance spectroscopy (EIS) technique, which is relatively so insensitive to the contact impedance that it could be adequate to accurately test membranes with high conductivity. A standard electrochemical conductivity cell was used as a reference. The experimental data was fitted to the equivalent circuits and the electrolyte resistance (R) was estimated from fitting procedure. The proton or ionic conductivity (σ) is calculated by

$$\sigma = \frac{d}{Rlt}, \quad (3)$$

where σ is the proton conductivity, d is the distance between the electrodes and R denotes the electrolyte resistance, respectively. l and t are the length and thickness of

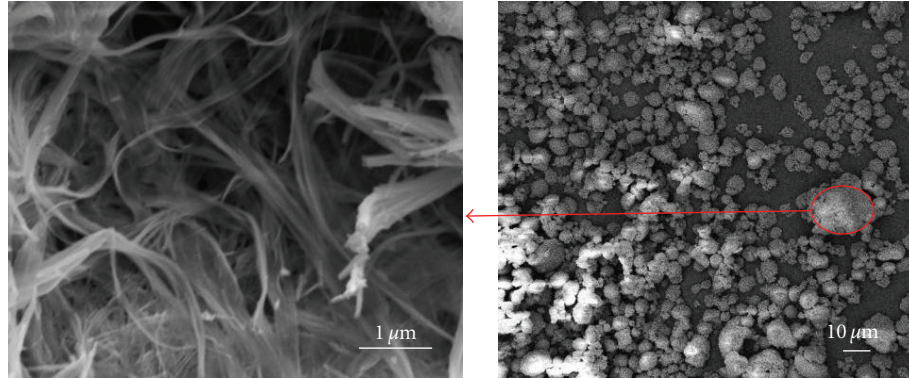


FIGURE 1: The SEM micrographs of titanium dioxide nanotubes synthesised using hydrothermal conventional heating method.

the membrane, respectively. The electrochemical cell was connected using a two-point probe technique to an Auto lab model 4.90006 potentiostat and Frequency Response Analyser (FRA). The home made cell was used with the electrode spacing of 1 cm, and the $3 \times 3 \text{ cm}^2$ membranes were used. The FRA electrochemical impedance software was used for the impedance measurements and analysis from 1 MHz to 1 Hz with the AC voltage amplitude of 5 mV.

2.4.7. Liquid Uptake. The nanocomposites films were completely dried in vacuum at 100°C for 24 hours and weighed (W_{dry}) and then placed in water/methanol (50/50) by volume solution at 25°C for 24 h. The nanocomposites films were then wiped dry quickly with filter paper and weighed (W_{wet}). The water/methanol uptake was then calculated as

$$\text{Water/methanol uptake (\%)} = \frac{W_{\text{wet}} - W_{\text{dry}}}{W_{\text{dry}}} * 100. \quad (4)$$

A methanol diffusion homemade cell was used based on previous reports [13]. Compartment A was filled with methanol solution and compartment B was filled with the same volume of deionized water. The membrane was clamped between the two compartments, and these were kept under stirring conditions during the experiment to avoid any concentration build-up in the two compartments. Methanol concentration profiles were determined over a period of time at different operating temperatures. Samples were kept for about 30 min between compartments. The concentration of methanol was determined by gas chromatography (GC).

2.4.8. Methanol (MeOH) Permeability. The measurements were carried out using a testing device constructed in our laboratories. The polymer membranes with surface area of $3 \times 3 \text{ cm}^2$ were inserted between vessels A and B. A 250 mL solution of MeOH (2 M) was transferred to vessel A, whilst vessel B was filled with 250 mL of deionised water (H_2O). After 24 h, the amount of methanol that crossed through the membrane to vessel B was determined by gas chromatography (GC 17A, Shimadzu model). The gas chromatograph was equipped with a capillary column (14% cyanopropyl phenyl methyl polysiloxane, $30 \text{ m} \times 0.25 \text{ mm} \times 1.0 \mu\text{m}$) and a flame ionisation detector (FID).

The permeability of methanol through the membrane can be expressed with diffusion coefficient, P ($\text{cm}^2 \cdot \text{s}^{-1}$) using equation (4) [14]

$$P = \frac{kVL}{A\Delta C}, \quad (5)$$

where k is the slope of the concentration profile ($\text{mol}/(\text{cm}^3 \cdot \text{s})$), V is the volume of a solution in compartment (cm^3), L is thickness of the membrane (cm), A is the active surface area of the membrane (cm^2), and ΔC is the difference of methanol concentration between two compartments (mol/cm^3).

3. Results and Discussions

3.1. Structure and Morphology of Titania Nanotubes. The SEM results of the TNTs samples are shown in Figure 1. The samples show the tubular structures with diameter ranging from 10 to 20 nm. Large bundles of TNTs structures agglomeration are observed (see low magnification). This is attributed to the presence of K^+ ions in the TNT structures, which can lead to an increase in the surface charge and electrostatic attraction between the tubes leading to agglomeration. This thermodynamic synthesis mechanism results in the formation of $\text{KTiO}_2(\text{OH})$ due to the presence of K^+ .

Figure 2(a) shows the FTIR spectra for TNTs that have been annealed at 300°C . The peaks corresponding to physically adsorbed water (O–H stretching mode at $\sim 3400 \text{ cm}^{-1}$ and O–H bending mode at $\sim 1640 \text{ cm}^{-1}$) all disappeared due to the higher annealing temperature of 300°C . This is consistent with the literature [15]. Only the Ti–O stretching mode is observed at $\sim 640 \text{ cm}^{-1}$ and 400 cm^{-1} ; this is attributed to the amorphous and anatase phase of TNT. XRD patterns for TNTs are shown in Figure 2(b) revealed the presence of both anatase and rutile phase. The additional peaks are ascribed to the interaction of K^+ ions and TiO_2 and have been previously reported [10, 15].

3.2. Structural Properties of Nanocomposite Membranes. The FTIR spectra showing vibration bands of Nafion and Nafion/TNTs nanocomposites are shown in Figure 3. The bands around 1200 – 620 cm^{-1} denote CF_2 – CF_2 stretching, and the bands around 1050 cm^{-1} denote the $-\text{SO}_3$ -symmetric

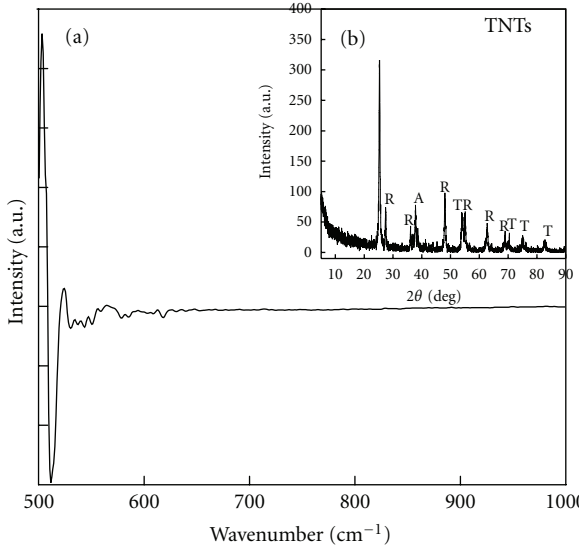


FIGURE 2: (a) FTIR spectra of TNTs and (b) XRD patterns of TNTs synthesised using hydrothermal conventional heating method and annealed at 300°.

stretching. All these bands are characteristics of the Nafion membrane [14, 16–18]. The vibration bands of Nafion and nanocomposite membranes are similar; this might be due to the very small amount of TNTs loading or poor interaction with polymer matrix.

3.3. Morphology. The SEM investigation was performed on the nanocomposite membranes, and micrographs are shown Figure 4. Samples were frozen and fractured to expose the cross-sectional surface of the nanocomposite membranes containing various amounts of TNTs in wt% 4(a) 0.5, 4(b) 1.0, and 4(c) 2.0. The micrographs show the presence of inorganic structures, homogeneously dispersed into polymer matrix. This indicates the presence of bundle TNTs into Nafion matrix. SEM images show similar dispersion for all TNTs loadings. This is in agreement with XRD results, demonstrating that TNTs nanocomposite had the same d-spacing independent of TNTs loadings. This good dispersion suggests that the number of accessible sites on the surface of TNTs is high contributing to the adhesion and electrostatic interaction.

3.4. Water/Methanol Uptake and Electrical Conductivity. The hydration of the Nafion membranes is crucial to maintain higher proton conductivity. However, the methanol or fuel crossover must be reduced to avoid the catalyst poisoning and improve the fuel cell performance. The water/methanol uptake was analysed to maintain higher fuel cell performance. The water uptake increases from 19% for pure Nafion to a maximum of about 22% for 1.0 wt% TNTs composite as shown in Figure 5. The water uptake of N-0.5 wt% TNTs and N-2 wt% TNTs remains at about 20%. The increase in water uptake with addition of TNTs suggests an increase in hydrophilic nature of Nafion.

The bulk electrical conductivity of Nafion and its TNTs-based nanocomposite membranes is shown in Figure 5.

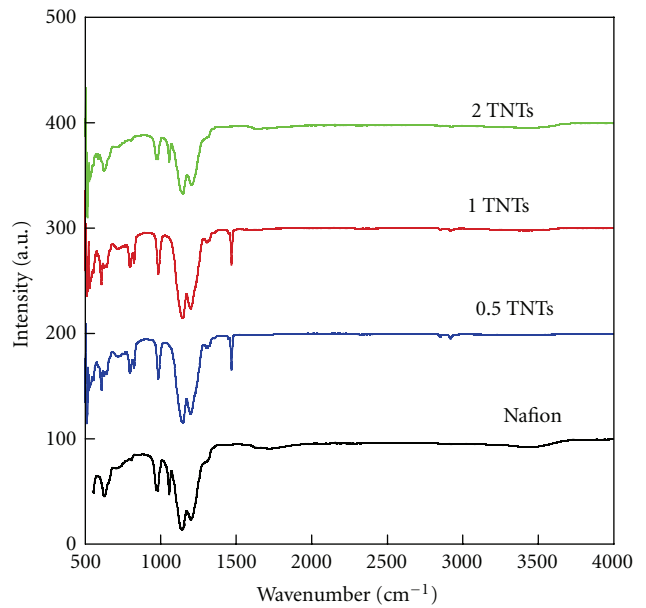


FIGURE 3: FTIR spectra of Nafion and its TNTs-based nanocomposite membranes with different TNTs loadings in wt% taken from 500 to 4000 cm^{-1} .

The electrical conductivity of Nafion increases from 0 to 0.06 S · cm⁻¹, when modified with 0.5 wt% of TNTs; it further increases to about 0.08 S · cm⁻¹, with 1.0 wt% incorporation. As the amount of TNTs into Nafion matrix increases to 2 wt%, the electrical conductivity decreases to zero, which is the same as that of pure Nafion. This decrease is associated with the electrical percolation threshold of Nafion and also the poor interaction between Nafion and TNTs as observed in FTIR spectra for 2 wt%.

3.5. Thermal Stability. Thermogravimetric analyses (TGA) of Nafion and its TNTs-based nanocomposite membranes are shown in Figure 6. Thermal degradation profiles of the nanocomposite samples are similar and show that the membranes are more thermally stable up to about 400°C compared to Nafion. The first degradation stage in a range of 30–120°C is assigned to the decomposition of physically adsorbed water present in the membranes. The weight loss in the range of 250–400°C is associated with the degradation of $-\text{SO}_3\text{H}$ -groups of Nafion [17]. This increase in thermal stability is attributed to the presence of TiO₂ nanostructures into Nafion. The results show a slightly higher thermal stability for 0.5 wt% of TNTs. This is attributed to the good interaction between Nafion matrix, which is in agreement with the SEM results.

3.6. Proton Conductivity and Methanol (MeOH) Permeability. To evaluate the influence of TNTs on the membranes electrochemical behaviour, electrochemical impedance spectroscopy measurements were performed. Figure 7 shows a Nyquist plot of Nafion and TNTs-based nanocomposites at 100% relative humidity. The plot gives electrolytes resistance (R) of the materials. The nanocomposite containing 0.5 wt% TNTs has the lowest $R = 210 \Omega$ (see Table 1). The electrolyte

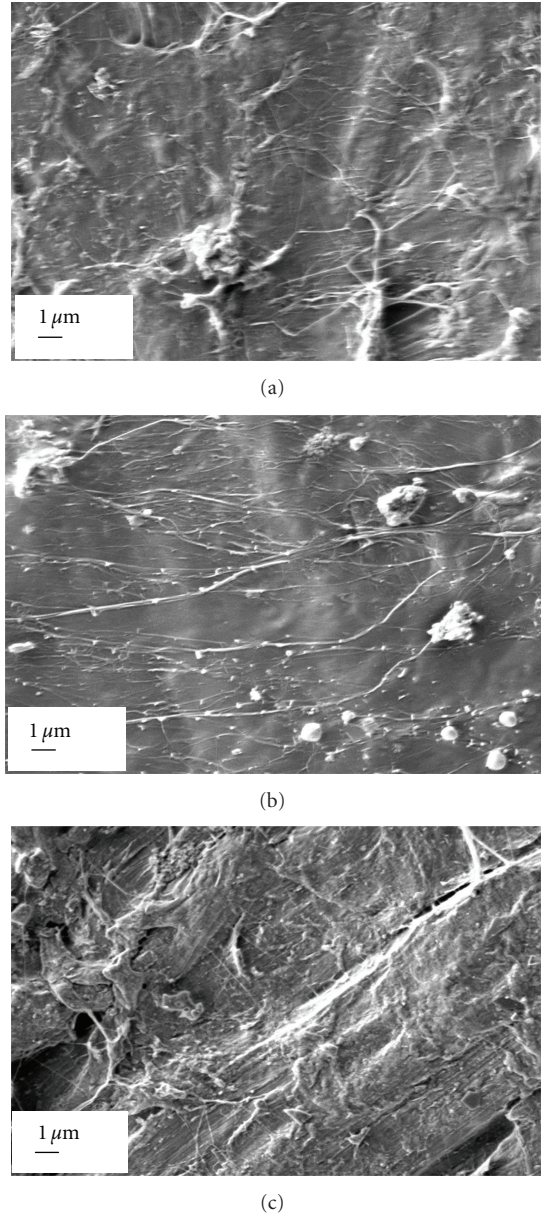


FIGURE 4: The SEM micrographs of the nanocomposite membranes containing various amounts of TNTs in wt% (a) 0.5, (b) 1.0, and (c) 2.0.

resistance increases as the TNTs loading increases to 1.0 and 2.0 wt%. This is indicative of a decrease in proton conductivity. This suggests that the amount of TNTs strongly influence the proton conductivity of Nafion. This decrease in proton conductivity can be due to the TNTs structures hindering the permeability of hydrogen ions. Whereas the electrolytes resistance decreases when 0.5 wt% TNTs was incorporated, indicating an increase in proton conductivity compared to pure Nafion. This increase in proton conductivity is related to the increase in water uptake observed with 1 wt% TNTs nanocomposite. The MeOH permeability was increased to $3 \times 10^{-8} \text{ cm}^2 \cdot \text{s}^{-1}$ with 1.0 wt% TNTs nanocomposite and sharply decreases to $1 \times 10^{-8} \text{ m}^2 \cdot \text{s}^{-1}$ as the amount of TNTs increases to 2 wt%. This behaviour is due to the

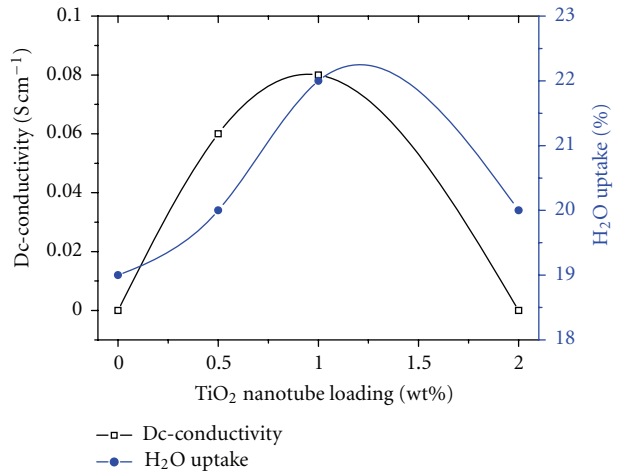


FIGURE 5: The bulk electrical conductivity and water-uptake plots of Nafion, and its TNTs-based nanocomposite membranes containing various amounts of TNTs.

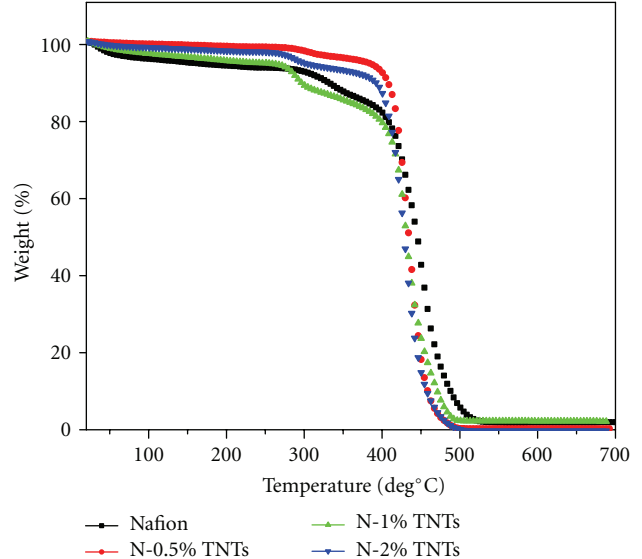


FIGURE 6: TGA plot of Nafion and TNTs-based nanocomposite membranes, with different loadings measured in nitrogen at 5°C per min.

MeOH permeability percolation threshold, which is affected by TNTs dispersed in Nafion.

The ratio of proton conductivity (σ) and methanol permeability (P) was calculated in order to estimate the performance of these nanocomposite membranes in fuel cell applications. The calculated values of proton conductivity and MeOH permeability are shown in Table 1. A decrease in the ratio was observed with an incorporation of TNTs in difference proportions.

4. Conclusion

In this paper, TNTs-based Nafion nanocomposite membranes were prepared in different proportions by melt-extrusion method. Water uptake of nanocomposite

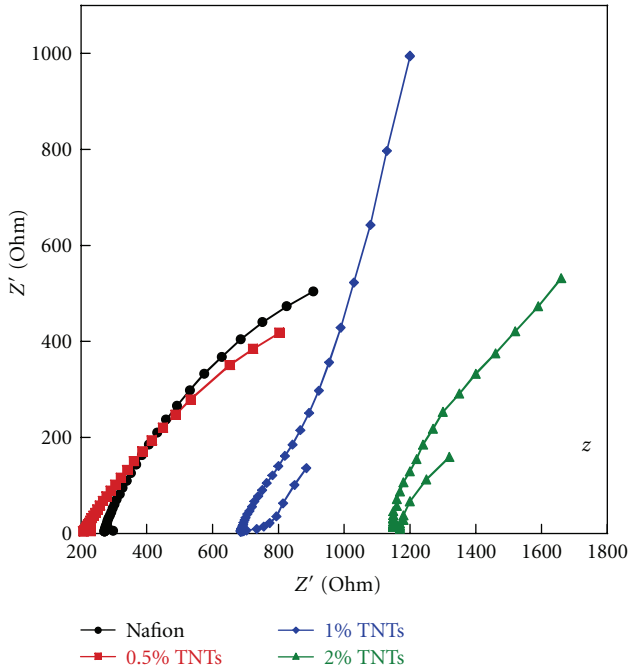


FIGURE 7: Nyquist plots of Nafion and its TNTs-based nanocomposite membranes, with different TNTs loadings ranging from 0.5 to 2.0 wt%, measurements done at room temperature (26°C) and 100% relative humidity.

TABLE 1: Parameters for circuit elements evaluated by fitting data to the equivalent circuit and calculated conductivity for prepared composite membranes. The average calculated error is about 8%.

Samples	t^a (cm)	R^b (Ω)	σ^c (S/cm)	P^d ($\text{cm}^2 \cdot \text{s}^{-1}$)	$(\sigma/P)^e$ ($\text{s} \cdot \text{S} \cdot \text{cm}^3$)
Nafion	0.020	230	0.070	2×10^{-8}	3.5×10^6
N-0.5 wt% TNTs	0.022	210	0.072	2×10^{-8}	3.6×10^6
N-1.0 wt% TNTs	0.022	690	0.022	3×10^{-8}	7.0×10^5
N-2.0 wt% TNTs	0.021	1150	0.014	1×10^{-8}	1.0×10^6

^aThickness of the membrane, ^belectrolyte resistance, ^cproton conductivity, ^dmethanol permeability of nanocomposite membranes, ^eratio of proton conductivity and water/MeOH uptake measurements.

membranes resulted higher than that of pure Nafion, with N-1.0 wt% TNTs reaching maximum of 21.5%. The highest electrical conductivity was observed with 1.0 wt% TNTs nanocomposite but remains at zero with 2.0 wt% TNTs nanocomposite. The thermal stability of Nafion increases with incorporation of TNTs. A reduced MeOH permeability was observed with 2.0 wt% TNTs nanocomposite membrane. The proton conductivity of Nafion slightly increases when 0.5 wt% TNTs and then decreases with an increase in the amount of TNTs. The best performing nanocomposite was the membrane containing only 0.5 wt% TNTs showing ionic conductivity value of $7.2 \times 10^{-2} \text{ S} \cdot \text{cm}^{-1}$ at 26°C and 100% of relative humidity.

Acknowledgments

The authors would like to thank the Department of Science and Technology (RSA), the Council for Scientific and

Industrial Research (CSIR), and the Tshwane University of Technology for financial support.

References

- [1] J. Z. Xu, W. B. Zhao, J. J. Zhu, G. X. Li, and H. Y. Chen, "Fabricating gold nanoparticle-oxide nanotube composite materials by a self-assembly method," *Journal of Colloid and Interface Science*, vol. 290, no. 2, pp. 450–454, 2005.
- [2] I. Paramasivam, J. M. Macak, and P. Schmuki, "Fabrication of titania nanomaterial and study characters of dye-sensitized solar cells: from one-dimension to silver surface modification of TiO₂," *Electrochemistry Communications*, vol. 10, no. 20, pp. 71–75, 2008.
- [3] S. K. Hazra and S. Basu, "High sensitivity and fast response hydrogen sensors based on electrochemically etched porous titania thin films," *Sensors and Actuators B*, vol. 115, no. 1, pp. 403–411, 2006.
- [4] J. Xu, C. Jia, B. Cao, and W. F. Zhang, "Electrochemical properties of anatase TiO₂ nanotubes as an anode material for lithium-ion batteries," *Electrochimica Acta*, vol. 52, no. 28, pp. 8044–8047, 2007.
- [5] L. Armelao, D. Barreca, G. Bottaro et al., "Recent trends on nanocomposites based on Cu, Ag and Au clusters: a closer look," *Coordination Chemistry Reviews*, vol. 250, no. 11-12, pp. 1294–1314, 2006.
- [6] G. M. Nuñez, R. J. Fenoglio, and D. E. Resasco, "Enhanced methane production from methanol decomposition over Pt/TiO₂ catalysts," *Reaction Kinetics and Catalysis Letters*, vol. 40, no. 1, pp. 89–94, 1989.
- [7] S. C. Chan and M. A. Bartaeu, "Preparation of highly uniform Ag/TiO₂ and Au/TiO₂ supported nanoparticle catalysts by photodeposition," *Langmuir*, vol. 21, no. 12, pp. 5588–5595, 2005.
- [8] Y. Ishibai, J. Sato, S. Akita, T. Nishikawa, and S. Miyagishi, "Photocatalytic oxidation of NOx by Pt-modified TiO₂ under visible light irradiation," *Journal of Photochemistry and Photobiology A*, vol. 188, no. 1, pp. 106–111, 2007.
- [9] M. M. Souza, N. F. Ribeiro, and M. Schmal, "SOFC using pure hydrogen considering air back diffusion phenomenon," *International Journal of Hydrogen Energy*, vol. 32, no. 2, pp. 423–425, 2007.
- [10] L. M. Sikhwivili, S. Sinha Ray, and N. J. Coville, "Influence of bases on hydrothermal synthesis of titanate nanostructures," *Applied Physics A*, vol. 94, no. 4, pp. 963–973, 2009.
- [11] T. Kasuga, M. Hiramatsu, A. Hoson, T. Sekino, and K. Niihara, "Formation of titanium oxide nanotube," *Langmuir*, vol. 14, no. 12, pp. 3160–3163, 1998.
- [12] S. Pavlidou and C. D. Papaspyrides, "A review on polymer-layered silicate nanocomposites," *Progress in Polymer Science*, vol. 33, no. 12, pp. 1119–1198, 2008.
- [13] N. P. Cele, S. Sinha Ray, S. K. Pillai et al., "Carbon nanotubes based nafion compositemembranes for fuel cell applications," *Fuel Cells*, vol. 10, no. 1, pp. 64–71, 2010.
- [14] S. Quezabo, J. C. T. Kwak, and M. Falk, "An infrared study of water-ion interactions in perfluorosulfonate (Nafion) membranes," *Canadian Journal of Chemistry*, vol. 62, no. 1, pp. 958–966, 1984.
- [15] U. Jeong and Y. Xia, "Synthesis and crystallization of monodisperse spherical colloids of amorphous selenium," *Advanced Materials*, vol. 17, no. 1, pp. 102–106, 2005.
- [16] M. Falk, "An infrared study of water in perfluorosulfonate (Nafion) membranes," *Canadian Journal of Chemistry*, vol. 58, no. 1, pp. 1496–1501, 1980.

- [17] H. L. Yeager and A. Steck, "Cation and water diffusion in nafion ion exchange membranes: influence of polymer structure," *Journal of the Electrochemical Society*, vol. 128, no. 9, pp. 1880–1884, 1981.
- [18] Xie, Q. Zhuang, Q. Wang, X. Liu, Y. Chen, and Z. Han, "In situ synthesis and characterization of poly(2, 5-benzoxazole)/ multiwalled carbon nanotubes composites," *Polymer*, vol. 52, no. 1, pp. 5271–5276, 2011.

Research Article

Challenges Found When Patterning Semiconducting Polymers with Electric Fields for Organic Solar Cell Applications

Fernando A. de Castro,¹ Frank Nüesch,² Christian Walder,² and Roland Hany²

¹ Materials Division, National Physical Laboratory, Hampton Road, Teddington TW11 0LW, UK

² Laboratory for Functional Polymers, Swiss Federal Institute for Materials Science and Technology, Empa, Ueberlandstrasse 129, 8600 Dübendorf, Switzerland

Correspondence should be addressed to Fernando A. de Castro, fernando.castro@npl.co.uk

Received 26 January 2012; Accepted 11 April 2012

Academic Editor: Mauro Coelho dos Santos

Copyright © 2012 Fernando A. de Castro et al. This is an open access article distributed under the Creative Commons Attribution License, which permits unrestricted use, distribution, and reproduction in any medium, provided the original work is properly cited.

A material-independent, contactless structuring method of semiconducting organic materials for the fabrication of interface-enhanced bilayer solar cells is not available so far. Patterning of thin films using electrohydrodynamic instabilities possesses many desired characteristics and has convincingly been used as a simple method to structure and replicate patterns of nonconducting polymers on submicrometer length scales. However, the applicability of this technique to a wider range of materials has not been demonstrated yet. Here, we report attempts to structure poly(*p*-phenylene vinylene) in a similar way. We found that thin films of poly(2-methoxy-5-(2'-ethylhexyl-oxy)-1,4-phenylene-vinylene) (MEH-PPV) and poly(2-methoxy-5-(3',7'-dimethyloctyloxy)-1,4-phenylene-vinylene) (MDMO-PPV) could not be destabilized at all in the limited accessible range of the experimental parameters set by the delicate chemical nature of these materials. We discuss failure origins and present possible loopholes for the patterning of semiconducting polymers using electric fields.

1. Introduction

Applications ranging from the medical science to the semiconductor industry require the control of polymer thin film structures on submicron length scales [1, 2]. A variety of techniques such as lithography or imprinting methods are used for polymer structuring [3]. Some of these methods are still expensive, however, when lower than 100 nm resolution is required, or may not be applicable for patterning of larger areas. Alternatively, polymers can be structured by self-assembly processes, such as pattern formation via instabilities in thin polymer films or polymer demixing of multicomponent blends [4].

The most efficient organic photovoltaic cells today are based on a bulk heterojunction device geometry consisting of a polymer donor/fullerene acceptor mixture, but the blend nanoscale morphology is difficult to control and depends largely on the processing conditions [5]. Therefore, new approaches that allow the controlled structuring of bicomponent mixtures of semiconducting materials are of general

interest [6]. For organic solar cells [7, 8], the targeted morphology consists of a bilayer structure (~200 nm thick, to absorb the entire incident light) of a donor and acceptor component that interdigitate markedly on a ~20 nm length scale to enable efficient charge generation within the diffusion length (~5–40 nm [9]) of the photoexcited electron-hole pair. At the same time, the active components should wet their respective electrode completely, to provide conduction paths for the selective extraction of charges [10] (Figure 1). Concepts for the creation of such nanostructured interface topographical features with high aspect ratios (feature heights : widths) using bottom-up (polymer demixing) or top-down (nanoimprint lithography) have been presented [11, 12] (among others), but a general low-cost and large-area compatible pattern method for organic solar cells is not available so far.

With the intention of fabricating such highly folded interpenetrating donor-acceptor bilayers for organic solar cells, we tested here electric fields to destabilize thin films of semiconducting polymers. An electric field applied normal

to an interface between two dielectric materials polarizes the dielectric, which results in an effective displacement charge density and an interfacial electrostatic pressure. This electrostatic pressure couples to the capillary wave spectrum of the liquid interface, selecting a narrow band of wavelengths that is amplified. Electrohydrodynamic patterning (EHP) has been shown to be an effective means of overcoming interfacial interactions and to produce arrays of nanoscale structures [13]. Using mainly classical, non-conducting polymers so far, electric fields have been applied to induce instability and pattern formation at a liquid/air or at a liquid/liquid interface [14, 15]. Electric fields have also been used to replicate patterned electrodes with submicron lateral dimensions [16].

2. Materials and Methods

Polystyrene (PS, $M_n = 150,000$, Aldrich) and poly(2-methoxy-5-(3',7'-dimethyloctyloxy)-1,4-phenylene-vinylene) (MDMO-PPV, $M_n = 50,000\text{--}500,000$, American Dye Source) were used as received, poly(2-methoxy-5-(2'-ethylhexyloxy)-1,4-phenylene-vinylene) (MEH-PPV, $M_n = 40,000\text{--}70,000$, Aldrich) was purified before use [11]. Films were spin coated from chlorobenzene (CB) on a first planar silicon electrode ($2.5 \times 2.5 \text{ cm}^2$) and were dried over night before use. On a second silicon electrode, LiF was evaporated as an x-shaped spacer pattern in high vacuum; afterwards, the two silicon plates were assembled into the capacitor geometry leaving a polymer/air gap. EHP was carried out under vacuum in an oven, with electrical feedthroughs to a Keithley source meter. Experiments were carried out at $T = 180^\circ\text{C}$, well above the glass transition temperatures and below the decomposition temperatures for both MEH-PPV and MDMO-PPV [17–19]. Rheology measurements (ARES Rheometric Scientific, parallel plate geometry, plate diameter 2.5 cm, plate gap 0.25 cm, shear rates 0.1–100 rad/s, under ambient air) were carried out for PS and MDMO-PPV in the temperature range of 160–240°C. AFM experiments were carried out on a Nanosurf Mobile S instrument. We used the software WsXM to analyse the AFM images [20].

3. Results and Discussion

Figure 2 shows a schematic view of the experimental setup. The polymer film is deposited onto the surface of a bottom electrode and covered with a top electrode, separated at a small distance using an insulating spacer. The whole setup is heated above the glass transition temperature (T_g) of the polymer, and an electric field is applied between the two electrodes. If the electrostatic pressure exceeds the capillary pressure generated by the curvature of the film due to thermal-induced surface fluctuations, the film is destabilized and pillars evolve with a characteristic separation distance $\lambda \propto \gamma^{1/2} H^{3/2} V^{-1}$ (for planar electrodes), where γ is the interfacial tension, V the applied voltage, and H the electrode spacing [13]. Decreasing the temperature below T_g finally freezes the morphology.

Since the electric field-induced instability is not material specific, it should be possible to destabilize essentially any

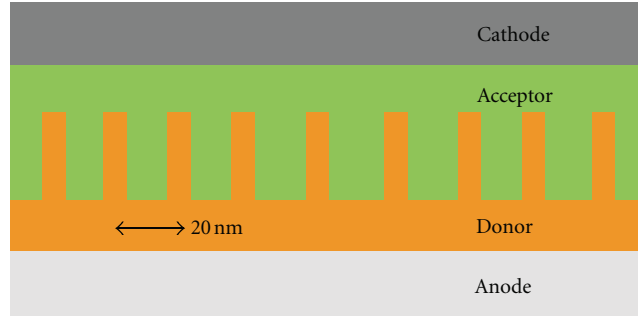


FIGURE 1: Sketch of an idealized (experimentally not yet realized on larger scale) organic heterojunction solar cell. The nature of the organic materials dictates the solar cell design criteria, which implies aspect ratios (height : width) of >1 for the nanostructured interface topography.

liquid with reasonably low viscosity, as long as the polymer does not degrade when heated to high temperatures. The experiment involves low-cost equipment and allows to pattern larger areas, provided that the electrodes can be arranged precisely parallel to each other. These are essential prerequisites for organic solar cell applications, where a proof-of-concept device would measure an active area of several square millimetres at least. As an important potential advantage for semiconducting polymers, patterning involves minimal contact between the material and the electrode, whereas lithographic or printing techniques can compromise optical and electrical properties [3].

We compared the effects of electric field-induced destabilization using both insulating (PS) and semiconducting polymers (MEH-PPV and MDMO-PPV). Figure 3(a) displays a destabilized PS film with characteristics closely resembling those reported when using similar experimental parameters. We used planar silicon electrodes separated by a 280 nm thick LiF spacer. The PS film had a thickness of 100 nm, and a voltage of 25 V was applied. During a total annealing time ($T = 180^\circ\text{C}$) of 22 hours, a small dielectric leakage current (9 mA) was flowing through the device [21].

This result indicates that the patterning method is robust and can easily be reproduced. Most often, destabilized features show a correlation over a length of several periods, beyond which domains with different orientations are found [13]. This would be of no concern for photovoltaic applications, where only the local heterojunction interface area should be maximised for charge transfer within the exciton diffusion length [9]. Enlarging the viewing angle for the PS sample, however, revealed that also the wavelengths of destabilized features varied considerably over a distance of $150 \times 150 \mu\text{m}^2$ (see Figure 3(b)). This is probably a signature of small lateral variations of the electric field, introduced by slight variations in the plate spacing [4]. We conclude that the precise electrode adjustment and control of the air gap and capacitor plate distances for larger areas requires a more sophisticated experimental setup than used here, for example, where a gap monitoring scheme is used to fix the electrodes at a constant distance and parallel to each other [22]. In addition, the strong dependence of the developing

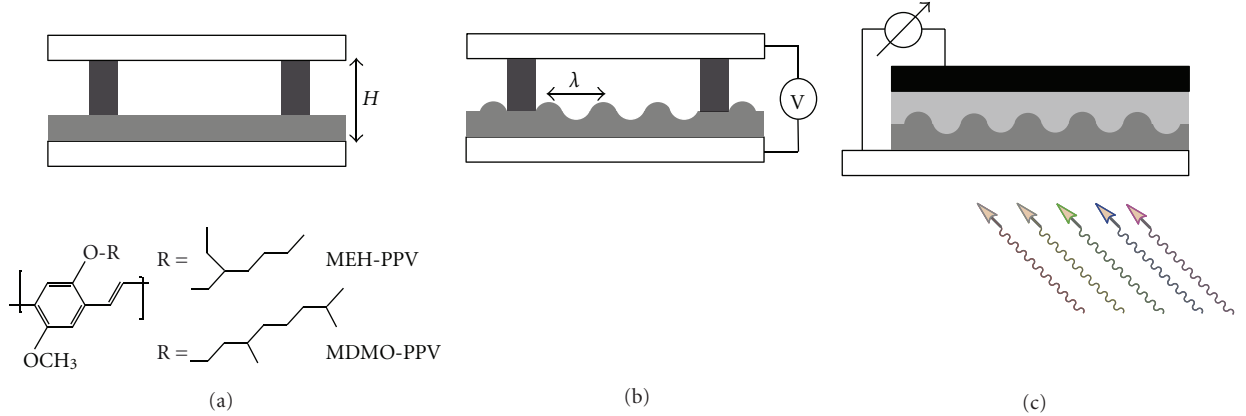


FIGURE 2: Molecular structure of the semiconducting polymers MEH-PPV and MDMO-PPV and the experimental EHP setup for the fabrication of organic solar cells. (a) A thin electron-donor polymer film is sandwiched between two electrodes separated by a distance H using insulating spacers. (b) A voltage applied across the electrodes induces instabilities in the film that evolve with a characteristic wavelength λ . (c) To complete the solar cell, the patterned polymer film is covered by an electron acceptor material and a top electrode. Arrows represent sunlight exciting the solar cell. More elaborated experimental setups could involve the destabilization of donor-acceptor polymer bilayers directly or the guided destabilization via patterned electrodes or prestructured polymer films [11].

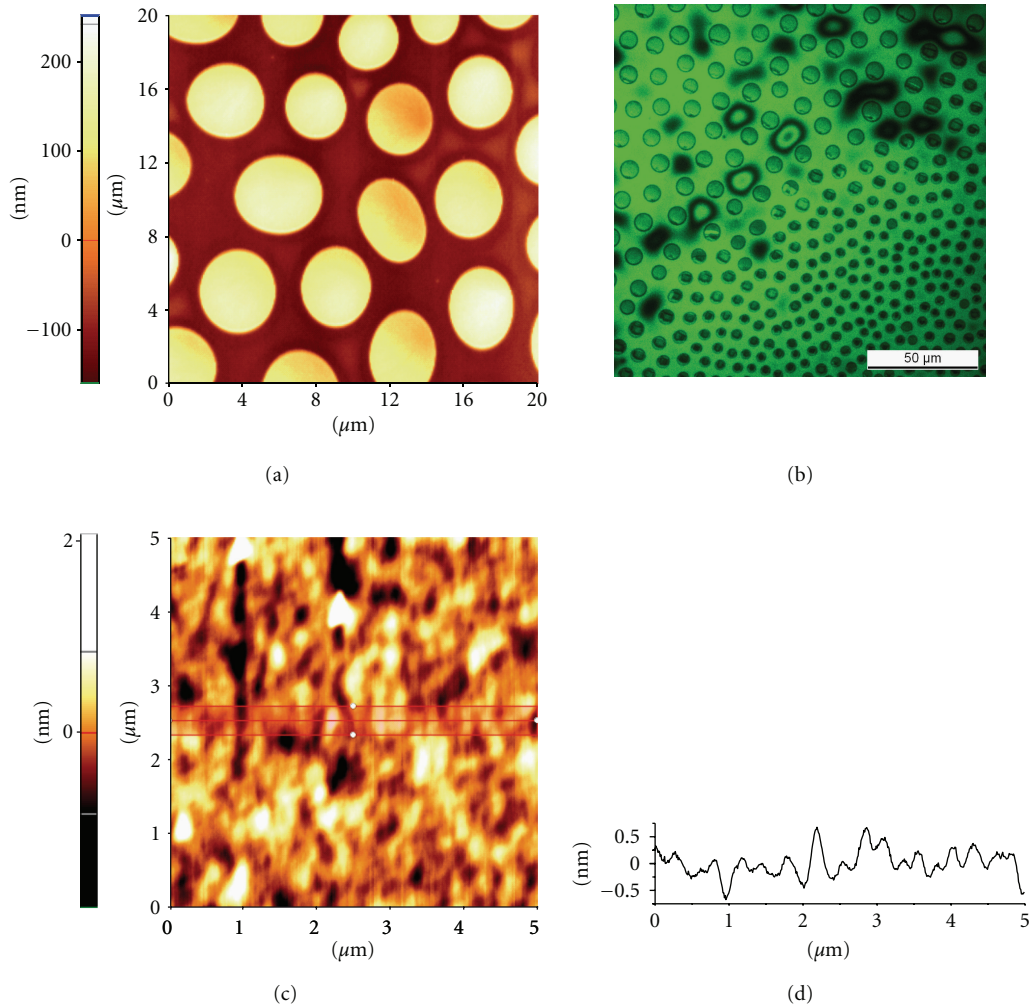


FIGURE 3: Atomic force microscope (AFM) images of (a) polystyrene (PS) and (c) MEH-PPV films after EHP using the same experimental conditions. Optical microscope image (b) of the patterned PS film. (d) Cross-section height profile of the MEH-PPV film shown in (c).

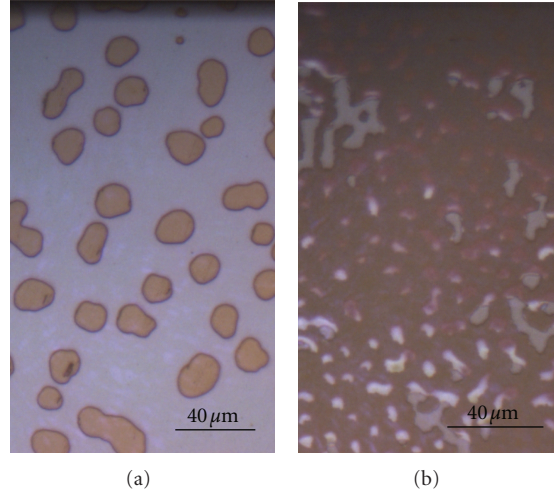


FIGURE 4: (a) Optical microscopy picture of MEH-PPV/PS bilayer film after EHP processing for 22 hours. PS droplets formed on an underlying MEH-PPV/PS film. (b) Removing PS with the selective solvent cyclohexane reveals that the MEH-PPV film has cracked erratically with no preferred wavelength; black spots indicating polymer degradation could visually be seen in such films.

wavelength on the local distance indicates that the electrodes must be precisely even. This might limit the substrate choice in actual organic solar cell devices, where cost-effective applications in various fields, such as portable electronics or smart textiles, are expected in the near future on flexible devices.

Figure 3(c) shows an AFM image of a treated MEH-PPV film using similar experimental parameters as for PS (100 nm thick film, LiF spacer 280 nm, $T = 180^\circ\text{C}$, $V = 20\text{ V}$, $t = 6\text{ h}$, leakage current $I = 9\text{ mA}$). Apparently, the film did not destabilize and remained essentially flat with roughness below 1 nm (Figure 3(d)). Attempts with different experimental parameters, such as film thickness (20, 30, 80 nm), airgap (130 nm), or reversed polarity and intensity of the applied electric field, were unsuccessful. The same was observed for the structurally closely related polymer MDMO-PPV. Both PPV polymers were much less stable than PS when exposed to higher voltage and longer destabilization times, what could be visually observed by the development of black spots in the films. This limited the range of parameters that could be used.

The inability to destabilize the semiconducting polymer films was unexpected since at high enough fields, the electrostatic driving force overpowers other interfacial pressures and the materials characteristics should no longer be determining [13]. One reason for the inability to induce instabilities in MEH-PPV and MDMO-PPV might be related to the semiconducting nature of these PPV polymers. While PS behaves to a good approximation as a dielectric and its pattern formation behaviour can be explained by the perfect dielectric models [13, 23], charges are more easily injected and rearranged in semiconducting materials. For such materials, the “leaky dielectric model” [24] predicts an additional tangential force at the surface due to the presence of free charges, which will tend to decrease charge concentration. If the normal electrostatic force is capable of overcoming this effect, the presence of free charges is expected to increase

the electrostatic stress at the surface, while lowering the electric field in the polymer. This would have little influence on the developing instability wavelength, but the temporal evolution of the instability would be accelerated by several orders of magnitude [13, 21]. Clearly, these predictions contradict with our experimental results and may suggest that tangential forces are important in these systems.

In a further attempt to destabilize the semiconducting film using EHP, we prepared a PS/MEH-PPV/air gap capacitor device [11]. Hierarchical structure formation using a polymer-polymer-air trilayer system has been convincingly shown using PMMA/PS [14]. Figure 4(a) shows the PS/MEH-PPV bilayer surface after 22 hour of EHP exposure, and Figure 4(b) displays the remaining MEH-PPV film after selective dissolution of PS. Apparently, PS in the bilayer polymer configuration destabilised in a similar pattern to a film that was coated directly on the silicon electrode (Figure 3(a)) [14]. Again, however, the MEH-PPV film did not follow the expected destabilisation (Figure 4(b)). For shorter process times (7 hours), the underlying MEH-PPV film remained flat (roughness below 1 nm, data not shown), while for longer process times the film breaks up erratically, with no preferential feature length scale emerging (not showing features that would suggest an EHP mechanism). In addition, such films changed visually colour and black spots appeared, suggesting that MEH-PPV has degraded.

A further reason that PPV films could not be destabilized might be due to the high viscosity of these stiff, backbone-conjugated materials. The developing pattern wavelength itself does not directly depend on the flow behaviour of the polymer melt, but the viscosity (η) influences the characteristic time (τ) for film destabilization strongly [13]. τ scales linearly with η [25] and patterning times ranging from seconds [21] to several days [14] have been reported for polymers with varying η values. For PS, the viscosity showed the characteristic thermoplastic flow behaviour, namely, a high

temperature dependence of η for low shear rates, a low temperature dependence of η for high shear rates, and a general decrease of η with increasing shear rate. On the other hand, MDMO-PPV behaved like a solid, and no meaningful rheological data could be obtained; we also observed that the polymer partly decomposed for temperatures above 200°C during the measurement. From this we conclude that MDMO-PPV could not be melted in the accessible temperature range without decomposition, which is probably a signature of the rodlike polymer backbone and the substantial polymer entanglement resulting from the synthesis [26]. Since the T_g of MDMO-PPV (~45°C) [18] is considerably lower than that of MEH-PPV (~66°C) [19], we argue that the latter would also have a similar solid-like behaviour.

4. Final Remarks

Electrohydrodynamic instabilities have been used during the last ten years as a powerful method to pattern polymers with submicron and ~100 nm features using planar and prestructured electrodes. To this end, mainly insulating polymers of low viscosity at higher temperatures have been used. Here, we tested EHP for the semiconducting polymers MEH-PPV and MDMO-PPV, two of the initial benchmark materials in the emerging field of organic solar cells. While PS could be readily structured using EHP in the most simple and large-area compatible approach, the semiconducting polymer thin films could not be destabilized at all. At the moment, we suspect this to be a combination of the semiconducting nature and/or the viscosity of these materials. The application of even higher temperature or voltage stress to induce destabilization is limited, since semiconducting polymers are labile and their optoelectronic performance degrades quickly with the formation of structural and chemical defects. It might be possible to use alternating electric fields to avoid the tangential movement of charges at the surface and to induce film destabilization. Another approach would be to reduce the polymer viscosity, for instance, by using plasticizers. For example, exposing PS to toluene vapour lowered T_g below room temperature and the viscosity was greatly reduced in the swollen film [25].

For possible solar cell applications, the more fundamental issues of creating destabilized features with dimensions well below ~100 nm and high aspect ratios need to be addressed in greater detail. The aspect ratio of the columnar structures is usually rather small (~0.05–0.2 [22]), meaning that the interfacial increase of the donor-acceptor area compared to the planar bilayer configuration in a solar cell would be limited. In principle, by using higher electric fields, both wavelengths can be decreased and the aspect ratio can be increased at the same time. However, due to the electrical breakdown of the capacitor device, this approach is clearly limited. Higher aspect ratios can be created by modulating the electric field distribution using topographically patterned masks. Possibly, this could also be achieved by combining flat electrodes with pre-structured polymer films [11]. In such cases, however, the spatial density of mask (or polymer) pillars is limited. This is because the effective electric field

modulation at a fixed distance decreases with increasing density of mask features; a smaller air gap would have to be used in these cases, finally limiting the attainable aspect ratios again [27].

Acknowledgments

The authors thank Jan Groenewold (University of Utrecht) and Jakob Heier (Empa) for helpful discussions. This paper was supported by Empa and by NPL's Material Research Programme (financed by the UK Department for Business, Innovation and Skills).

References

- [1] L. Jiang, X. Wang, and L. Chi, "Nanoscaled surface patterning of conducting polymers," *Small*, vol. 7, no. 10, pp. 1309–1321, 2011.
- [2] Y. Xu, F. Zhang, and X. Feng, "Patterning of conjugated polymers for organic optoelectronic devices," *Small*, vol. 7, no. 10, pp. 1338–1360, 2011.
- [3] Z. Nie and E. Kumacheva, "Patterning surfaces with functional polymers," *Nature Materials*, vol. 7, no. 4, pp. 277–290, 2008.
- [4] U. Steiner, "Structure formation in polymer films," in *Nanoscale Assembly*, W. T. S. Huck, Ed., vol. 1, pp. 1–24, Springer, 2005.
- [5] Y. Liang, Z. Xu, J. Xia et al., "For the bright future-bulk heterojunction polymer solar cells with power conversion efficiency of 7.4%," *Advanced Materials*, vol. 22, no. 20, pp. E135–E138, 2010.
- [6] M. Helgesen, R. Søndergaard, and F. C. Krebs, "Advanced materials and processes for polymer solar cell devices," *Journal of Materials Chemistry*, vol. 20, no. 1, pp. 36–60, 2010.
- [7] B. Walker, C. Kim, and T. Q. Nguyen, "Small molecule solution-processed bulk heterojunction solar cells," *Chemistry of Materials*, vol. 23, no. 3, pp. 470–482, 2011.
- [8] P. G. Nicholson and F. A. Castro, "Organic photovoltaics: principles and techniques for nanometre scale characterization," *Nanotechnology*, vol. 21, no. 49, Article ID 492001, 2010.
- [9] P. Peumans, A. Yakimov, and S. R. Forrest, "Small molecular weight organic thin-film photodetectors and solar cells," *Journal of Applied Physics*, vol. 93, no. 7, pp. 3693–3723, 2003.
- [10] P. K. Watkins, A. B. Walker, and G. L. B. Verschoor, "Dynamical monte carlo modelling of organic solar cells: the dependence of internal quantum efficiency on morphology," *Nano Letters*, vol. 5, no. 9, pp. 1814–1818, 2005.
- [11] F. A. Castro, H. Benmansour, C. F. O. Graeff, F. Nüesch, E. Tutis, and R. Hany, "Nanostructured organic layers via polymer demixing for interface-enhanced photovoltaic cells," *Chemistry of Materials*, vol. 18, no. 23, pp. 5504–5509, 2006.
- [12] X. He, F. Gao, G. Tu et al., "Formation of nanopatterned polymer blends in photovoltaic devices," *Nano Letters*, vol. 10, no. 4, pp. 1302–1307, 2010.
- [13] N. Wu and W. B. Russel, "Micro- and nano-patterns created via electrohydrodynamic instabilities," *Nano Today*, vol. 4, no. 2, pp. 180–192, 2009.
- [14] M. D. Morariu, N. E. Voicu, E. Schäffer, Z. Lin, T. P. Russell, and U. Steiner, "Hierarchical structure formation and pattern replication induced by an electric field," *Nature Materials*, vol. 2, no. 1, pp. 48–52, 2003.
- [15] P. S. G. Pattader, I. Banerjee, A. Sharma, and D. Bandyopadhyay, "Multiscale pattern generation in viscoelastic polymer

- films by spatiotemporal modulation of electric field and control of rheology," *Advanced Functional Materials*, vol. 21, no. 2, pp. 324–335, 2011.
- [16] E. Schäffer, T. Thurn-Albrecht, T. P. Russell, and U. Steiner, "Electrically induced structure formation and pattern transfer," *Nature*, vol. 403, no. 6772, pp. 874–877, 2000.
 - [17] R. F. Cossiello, L. Akcelrud, and T. D. Z. Atvars, "Solvent and molecular weight effects on fluorescence emission of MEH-PPV," *Journal of the Brazilian Chemical Society*, vol. 16, no. 1, pp. 74–86, 2005.
 - [18] B. Conings, S. Bertho, K. Vandewal et al., "Modeling the temperature induced degradation kinetics of the short circuit current in organic bulk heterojunction solar cells," *Applied Physics Letters*, vol. 96, no. 16, Article ID 163301, 3 pages, 2010.
 - [19] J. Y. Kim and C. D. Frisbie, "Correlation of phase behavior and charge transport in conjugated polymer/fullerene blends," *Journal of Physical Chemistry C*, vol. 112, no. 45, pp. 17726–17736, 2008.
 - [20] I. Horcas, R. Fernández, J. M. Gómez-Rodríguez, J. Colchero, J. Gómez-Herrero, and A. M. Baro, "WSXM: a software for scanning probe microscopy and a tool for nanotechnology," *Review of Scientific Instruments*, vol. 78, no. 1, Article ID 013705, 8 pages, 2007.
 - [21] P. Goldberg-Oppenheimer and U. Steiner, "Rapid electrohydrodynamic lithography using low-viscosity polymers," *Small*, vol. 6, no. 11, pp. 1248–1254, 2010.
 - [22] M. D. Dickey, A. Raines, E. Collister, R. T. Bonnecaze, S. V. Sreenivasan, and C. G. Willson, "High-aspect ratio polymeric pillar arrays formed via electrohydrodynamic patterning," *Journal of Materials Science*, vol. 43, no. 1, pp. 117–122, 2008.
 - [23] E. Schäffer, T. Thurn-Albrecht, T. P. Russell, and U. Steiner, "Electrohydrodynamic instabilities in polymer films," *Europhysics Letters*, vol. 53, no. 4, pp. 518–524, 2001.
 - [24] L. F. Pease and W. B. Russel, "Linear stability analysis of thin leaky dielectric films subjected to electric fields," *Journal of Non-Newtonian Fluid Mechanics*, vol. 102, no. 2, pp. 233–250, 2002.
 - [25] S. Harkema and U. Steiner, "Hierarchical pattern formation in thin polymer films using an electric field and vapor sorption," *Advanced Functional Materials*, vol. 15, no. 12, pp. 2016–2020, 2005.
 - [26] T. Schwalm, J. Wiesecke, S. Immel, and M. Rehahn, "The gilch synthesis of poly(p-phenylene vinylenes): mechanistic knowledge in the service of advanced materials," *Macromolecular Rapid Communications*, vol. 30, no. 15, pp. 1295–1322, 2009.
 - [27] J. Heier, J. Groenewold, and U. Steiner, "Pattern formation in thin polymer films by spatially modulated electric fields," *Soft Matter*, vol. 5, pp. 3997–4005, 2009.

Research Article

Electrochemical Characterization of $\text{Li}_4\text{Ti}_5\text{O}_{12}/\text{C}$ Anode Material Prepared by Starch-Sol-Assisted Rheological Phase Method for Li-Ion Battery

Zhenpo Wang,¹ Guowei Xie,² and Lijun Gao^{2,3}

¹ National Engineering Laboratory for Electric Vehicles, Beijing Institute of Technology, Beijing 100081, China

² Department of Chemistry, Nanchang University, Nanchang 330031, China

³ School of Energy, Soochow University, Suzhou 215006, China

Correspondence should be addressed to Zhenpo Wang, wangzhenpo@bit.edu.cn and Lijun Gao, lijungao@yahoo.com

Received 7 January 2012; Revised 13 May 2012; Accepted 13 May 2012

Academic Editor: Arava Leela Mohana Reddy

Copyright © 2012 Zhenpo Wang et al. This is an open access article distributed under the Creative Commons Attribution License, which permits unrestricted use, distribution, and reproduction in any medium, provided the original work is properly cited.

$\text{Li}_4\text{Ti}_5\text{O}_{12}/\text{C}$ composite was synthesized by starch-sol-assisted rheological phase method using inexpensive raw material starch as carbon coating precursor. The $\text{Li}_4\text{Ti}_5\text{O}_{12}/\text{C}$ powder was characterized using XRD, SEM, and TG techniques. The synthesized $\text{Li}_4\text{Ti}_5\text{O}_{12}$ crystallites are cohesively covered by conductive carbon from starch sol which leads to increased conductivity, and the particle size of $\text{Li}_4\text{Ti}_5\text{O}_{12}/\text{C}$ is about 500 nm. The electrochemical performance of $\text{Li}_4\text{Ti}_5\text{O}_{12}/\text{C}$ was characterized by galvanostatic charge/discharge and EIS methods, and the results show that the $\text{Li}_4\text{Ti}_5\text{O}_{12}/\text{C}$ presents a high discharge capacity, high rate capability, and long cycle life. The capacity retention was at 87% (500 cycles at 1C) and 73.0% (2000 cycles at 20C) indicating promising high rate performance of $\text{Li}_4\text{Ti}_5\text{O}_{12}/\text{C}$ as anode material for lithium ion battery.

1. Introduction

Lithium ion batteries have been promising to be used in electric vehicle (EV) or hybrid electric vehicle (HEV). Currently, graphite was widely used as anode material for commercial Li-ion batteries in cell phones, laptops, and cameras [1]. However, its performance has not been satisfactory for applications in power systems which require frequent high rate charge/discharge such as in EV or HEV [2, 3]. Owing to the low lithium intercalation voltage of approximately 0.1 V (versus. Li/Li^+), lithium metal is easily deposited on the surface of graphite anode forming dendritic lithium particularly during fast charge, resulting in safety issue [2, 4]. Spinel $\text{Li}_4\text{Ti}_5\text{O}_{12}$ has acquired much attention as alternative anode to graphite in Li-ion batteries, due to its excellent reversibility, zero-strain structure, and high lithium ion mobility in the $\text{Li}_4\text{Ti}_5\text{O}_{12}$ lattice [5~7]. Especially, the material has a high Li-insertion voltage operating at 1.55 V (versus. Li/Li^+), which could hinder dendritic lithium formation [1, 5]. However, the low electronic conductivity

($10^{-13} \text{ S cm}^{-1}$) of $\text{Li}_4\text{Ti}_5\text{O}_{12}$ has been the main obstacle limiting rate performance of the material [6].

To improve electronic conductivity and electrochemical performance of $\text{Li}_4\text{Ti}_5\text{O}_{12}$, extensive works have been taken to address the issue, and the common strategies are to reduce particle size [4, 5], coat conductive material on the surface of $\text{Li}_4\text{Ti}_5\text{O}_{12}$ [2, 6, 7], or dope with other metal ions [8, 9]. Reducing particle size can shorten lithium ion diffusion distance and enhance both the electrode capability of Li storage and kinetics; thus the rate capability and electrochemical performance of electrode material can be improved [10]. Various metal ions such as Ni^{3+} , Ca^{3+} , Ta^{5+} , V^{5+} , and Mg^{2+} were employed in doping to substitute a small quantity of Li^+ or Ti^{4+} to improve the electronic conductivity and rate capability [8, 11~13]. Coating conductive materials on the surface of $\text{Li}_4\text{Ti}_5\text{O}_{12}$ can improve surface conductivity and reduce contact resistance [2]. Conductive materials (carbon black, carbon nanotubes, grapheme, Ag, Cu, and Sn [6, 10, 14, 15]) have been reported to be used to modify the electric conductivity of $\text{Li}_4\text{Ti}_5\text{O}_{12}$.

Many kinds of carbon have been examined as coating source in synthesis of $\text{Li}_4\text{Ti}_5\text{O}_{12}/\text{C}$ composite material with excellent electrochemical performance by conventional methods (e.g., solid state reaction and sol-gel methods) [3, 16, 17]. Starch is not only a good template in synthesis of various function materials with excellent electrochemical performance [18, 19] but also a good carbon source of coating to improve electric conductivity and reduce particle size [20]. Starch-sol-assisted rheological phase method has been developed to synthesize LiFePO_4/C composite [20]. However, to the best of our knowledge, synthesis of $\text{Li}_4\text{Ti}_5\text{O}_{12}/\text{C}$ composite has not been reported previously by using this method. In this work, we have used inexpensive starch as carbon source and adopted rheological phase method to prepare high-capacity $\text{Li}_4\text{Ti}_5\text{O}_{12}/\text{C}$ material. The composite was characterized by XRD, SEM, and TG techniques, and galvanostatic charge/discharge and EIS methods were used to examine electrochemical performance. The results show that carbon is cohesively coated on the surface of $\text{Li}_4\text{Ti}_5\text{O}_{12}$, and the composite has demonstrated high rate performance with good cycle stability when it was tested as anode in Li-ion batteries.

2. Experimental

2.1. Preparation of $\text{Li}_4\text{Ti}_5\text{O}_{12}$ and $\text{Li}_4\text{Ti}_5\text{O}_{12}/\text{C}$. The starting raw materials, TiO_2 -anatase (Aldrich), LiOH (Aldrich), and starch, were analytical grade and used without further purification. Firstly, the soluble starch (3.0 g starch/0.02 mol $\text{Li}_4\text{Ti}_5\text{O}_{12}$) was mixed with appropriate amount of deionized water; the resultant mixture was heated initially at 110°C until the solution became transparent under stirring in oil bath. Then the starch sol was mixed with stoichiometric amount of LiOH and TiO_2 (molar ratio of Ti:Li = 4.2:5) under vigorous agitation to obtain a solid-liquid rheological body, which appears to be a mushy slurry. Finally, the mushy slurry was transferred to tubular furnace and heated at the rate of 15°C min⁻¹ to 850°C and sintered at 850°C for 4 h in N_2 atmosphere and then cooled to room temperature to obtain a grey $\text{Li}_4\text{Ti}_5\text{O}_{12}/\text{C}$ powder. For comparison, pure $\text{Li}_4\text{Ti}_5\text{O}_{12}$ without carbon coating was synthesized by solid state method, which was prepared by mixing TiO_2 -anatase and LiOH (mole ratio of Li:Ti = 4.2:5); the mixture was heated at 850°C for 4 h in air to obtain well-crystallized white powder $\text{Li}_4\text{Ti}_5\text{O}_{12}$.

2.2. Electrode Fabrication. The electrochemical characterization was carried out by galvanostatic charge and discharge using a two-electrode type of 2025 coin cell. The working electrode was prepared with 84 wt.% active material $\text{Li}_4\text{Ti}_5\text{O}_{12}$ or $\text{Li}_4\text{Ti}_5\text{O}_{12}/\text{C}$, 10 wt.% super-P-Li carbon black, and 3 wt.% CMC (carboxymethyl cellulose sodium), and 3 wt.% SBR (styrene butadiene rubber) dissolved into deionized water to form mixed slurry. The slurries were dispersed in a planetary mixer and then spread uniformly on an aluminum foil by using doctor blade. Finally, the laminates were dried under vacuum at 100°C for 24 h before electrochemical evaluation. Electrode disks were punched

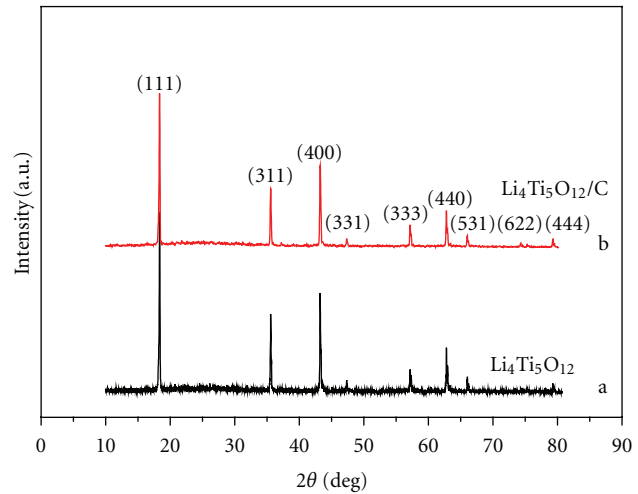


FIGURE 1: XRD pattern of pure spinel $\text{Li}_4\text{Ti}_5\text{O}_{12}$ (a) and $\text{Li}_4\text{Ti}_5\text{O}_{12}/\text{C}$ (b).

out of the laminates for the half-cell. The cells were assembled based on the configuration of Li/electrolyte/ $\text{Li}_4\text{Ti}_5\text{O}_{12}/\text{C}$ (or $\text{Li}_4\text{Ti}_5\text{O}_{12}$) with a liquid electrolyte (1.3 M LiPF_6 in a mixture (1:3 by mass) of ethylene carbonate and dimethyl carbonate), metallic Li foil was used as the counter electrode in 2-electrode cell, and Celgard 2320 was used as the separator; the coin cells were assembled in a glove box (Braun, $[\text{O}_2] < 1 \text{ ppm}$, $[\text{H}_2\text{O}] < 1 \text{ ppm}$) filled with pure argon.

2.3. Characterization. The samples of $\text{Li}_4\text{Ti}_5\text{O}_{12}/\text{C}$ and $\text{Li}_4\text{Ti}_5\text{O}_{12}$ were characterized by X-ray diffraction (XRD) with D/Max-III A instrument using $\text{Cu K}\alpha$ ($\lambda = 1.54056 \text{ \AA}$) as radiation source at a scanning rate 2° min^{-1} for 2Θ in the range of 10–80° to identify the structure and phase. The morphologies of the samples were investigated by scanning electron microscopy (SEM, Hitachi S4800) and transmission electron microscopy (TEM, JEOL JEM-2010). Thermogravimetric and differential thermal analyses (TG/TGA) were performed on a TG/TGA instrument (Pyris Diamond) using a heating rate of 5°C/min.

The charge/discharge behavior and rate capacity of the cell were tested at various current densities in the range 1.0~2.0 V using land battery test station at room temperature. The AC impedance spectrum was employed at a constant potential of 1.55 V against Li metal electrode, the voltage amplitude of the AC signal was 5 mV, and the frequencies were scanned from 100 kHz to 100 mHz by using an electrochemical workstation IM6ex (Zahner).

3. Results and Discussion

3.1. Physicochemical Characterization. Figure 1 presents the XRD pattern of the two samples. Figure 1(a) is for the pure $\text{Li}_4\text{Ti}_5\text{O}_{12}$ prepared by solid-state method, and Figure 1(b) is for the $\text{Li}_4\text{Ti}_5\text{O}_{12}/\text{C}$ composite synthesized by starch-sol-assisted rheological phase method. According to JCPDS file

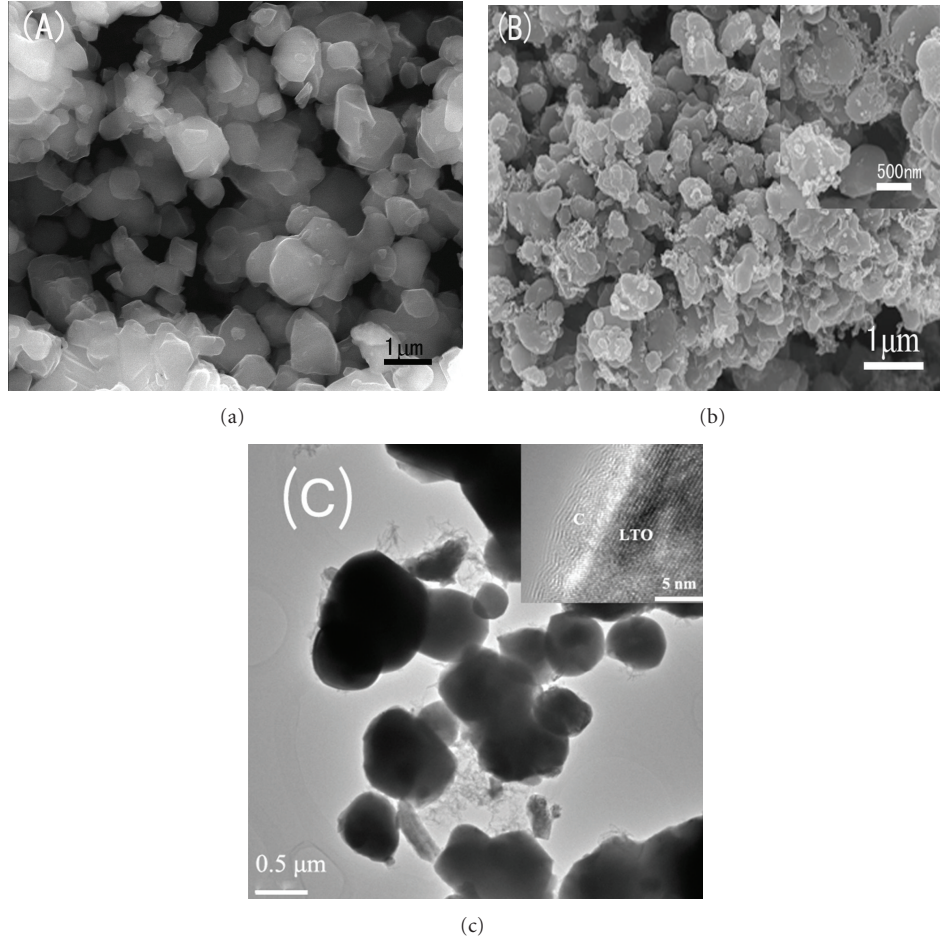


FIGURE 2: SEM images of pure $\text{Li}_4\text{Ti}_5\text{O}_{12}$ (a) and $\text{Li}_4\text{Ti}_5\text{O}_{12}/\text{C}$ composite (b). HRTEM image and the inset (c) clearly show the carbon coating on the $\text{Li}_4\text{Ti}_5\text{O}_{12}$ crystallites.

no. 49-0207, all the main peaks are investigated, which correspond to $\text{Li}_4\text{Ti}_5\text{O}_{12}$ without other impurity phases. The pattern could be indexed to spinel structure with $\text{Fd}3\text{m}$ space group. The lattice parameter of “ a ” for $\text{Li}_4\text{Ti}_5\text{O}_{12}/\text{C}$ composite is 8.359 Å, which is close to the reported value of the literature [21]. No carbon diffraction peak is observed in Figure 1(b) since the carbon generated from starch is in low content, and it is amorphous, which suggests that the addition of starch in the precursor does not influence the formation of spinel $\text{Li}_4\text{Ti}_5\text{O}_{12}$ crystal during heat treatment in the N_2 atmosphere. It was found through Scherrer equation that the average crystallite size was about 400~600 nm.

For comparison, Figure 2(a) shows the SEM image of pure $\text{Li}_4\text{Ti}_5\text{O}_{12}$ synthesized by solid-state method. The $\text{Li}_4\text{Ti}_5\text{O}_{12}$ crystallites have smooth sphere-like shape morphology, large blocks of particles at about 700 nm~1 μm in size. Figure 2(b) presents SEM image of the $\text{Li}_4\text{Ti}_5\text{O}_{12}/\text{C}$ composite. It is seen that the carbon uniformly covers the surface of $\text{Li}_4\text{Ti}_5\text{O}_{12}$ and links together forming a carbon network. The particles of $\text{Li}_4\text{Ti}_5\text{O}_{12}/\text{C}$ have a relatively less extent of agglomeration, and the average particle size is about 500 nm, which is consistent with the result from

XRD calculation. Figure 2(c) shows the high-resolution TEM image of the $\text{Li}_4\text{Ti}_5\text{O}_{12}/\text{C}$ composite; it is clearly seen that the $\text{Li}_4\text{Ti}_5\text{O}_{12}$ has sphere-like shape and the particle size ranges from 400 nm to 600 nm, consistent with the SEM observation in Figure 2(b). The inset HRTEM also shows a 5 nm thick carbon film coated on the surface of $\text{Li}_4\text{Ti}_5\text{O}_{12}$ crystallites. Due to the adhesive nature of starch sol, the carbon binds cohesively on the surface of reactants during calcination process, and the heating process further results in decomposition of the starch into a carbonaceous deposit on the surface of $\text{Li}_4\text{Ti}_5\text{O}_{12}$. The carbonization of starch precursor effectively restrains the growth of $\text{Li}_4\text{Ti}_5\text{O}_{12}$ crystallites into larger size.

In order to investigate the content of carbon in the composite $\text{Li}_4\text{Ti}_5\text{O}_{12}/\text{C}$, TG/DTA was carried out with $15^\circ\text{C min}^{-1}$ heating rate from 30°C to 1000°C in air. The profile of TG/DTA is given in Figure 3. A broad exothermic peak appears at about 580°C , which is owing to the combustion of the starch into carbonaceous species on the surface of $\text{Li}_4\text{Ti}_5\text{O}_{12}$, and the TG indicates that the content of carbon in the composite $\text{Li}_4\text{Ti}_5\text{O}_{12}/\text{C}$ is about 5%. The weight loss after 700°C is due to the loss of lithium during the high temperature process [22, 23].

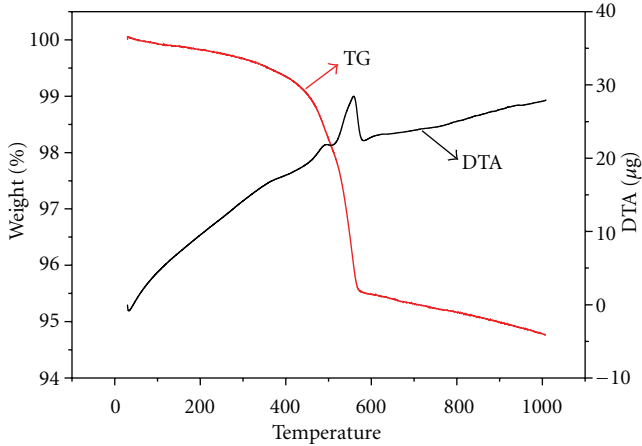


FIGURE 3: TG/TGA profile of $\text{Li}_4\text{Ti}_5\text{O}_{12}/\text{C}$ measured in air atmosphere.

3.2. Electrochemical Characterization. The electrochemical performance of $\text{Li}_4\text{Ti}_5\text{O}_{12}/\text{C}$ and $\text{Li}_4\text{Ti}_5\text{O}_{12}$ electrodes was examined in coin cells with metallic lithium as counter electrode. The cycle behavior of the cell was investigated in the range of 1.0~2.0 V. The initial charge-discharge curves of $\text{Li}_4\text{Ti}_5\text{O}_{12}$ (a) and $\text{Li}_4\text{Ti}_5\text{O}_{12}/\text{C}$ (b) at various charge/discharge rates are compared as shown in Figure 4. At the current density of 0.2C, the initial discharge capacity of $\text{Li}_4\text{Ti}_5\text{O}_{12}/\text{C}$ is 171.5 mAh g^{-1} , which is very close to its theoretical capacity (175 mAh g^{-1}), and at a 20C high rate, the capacity is 110 mAh g^{-1} . Furthermore, the profile shows very flat discharge/discharge plateau at around 1.55 V (versus. Li/Li^+). However, the initial specific capacity of pure $\text{Li}_4\text{Ti}_5\text{O}_{12}$ is only about 160 mAh g^{-1} at 0.2C and 34.5 mAh g^{-1} at 20C, the cell voltage is lower, and the polarization increases with the increasing of charge/discharge rate, as it is shown that the plateau voltage difference between charge and discharge is 60 mV at 0.5C and 440 mV at 20C. With carbon-coated $\text{Li}_4\text{Ti}_5\text{O}_{12}/\text{C}$, the polarization was obviously smaller as it is seen that the voltage gap between charge and discharge plateau is narrower as shown in Figure 4(b), and the plateau appears more flat especially at high rates. This improved high-rate discharge ability of $\text{Li}_4\text{Ti}_5\text{O}_{12}/\text{C}$ which may be attributed to the facts that (1) the carbon generated from starch was coated uniformly on the surface of $\text{Li}_4\text{Ti}_5\text{O}_{12}$ resulting in enhanced electrical conductivity and (2) the starch limited the growth of $\text{Li}_4\text{Ti}_5\text{O}_{12}$ crystallite size during calcination process, which benefits Li^+ diffusion with shortened distance in $\text{Li}_4\text{Ti}_5\text{O}_{12}$.

To investigate the rate capability, the $\text{Li}_4\text{Ti}_5\text{O}_{12}$ and $\text{Li}_4\text{Ti}_5\text{O}_{12}/\text{C}$ have been cycled at various rates from 0.2C to 20C, and the results are presented in Figure 5. The charge and discharge cycles were taken for 5 cycles at each rate. As shown in Figure 5(a), the specific discharge capacity is gradually decreased with increased rates. However, the degree of capacity decay of $\text{Li}_4\text{Ti}_5\text{O}_{12}/\text{C}$ sample is in less extent in comparison with the pure $\text{Li}_4\text{Ti}_5\text{O}_{12}$. At 20C the capacity remains 75% of that at 0.2C for $\text{Li}_4\text{Ti}_5\text{O}_{12}/\text{C}$, but for pure $\text{Li}_4\text{Ti}_5\text{O}_{12}$ the capacity is about 24% between 20C

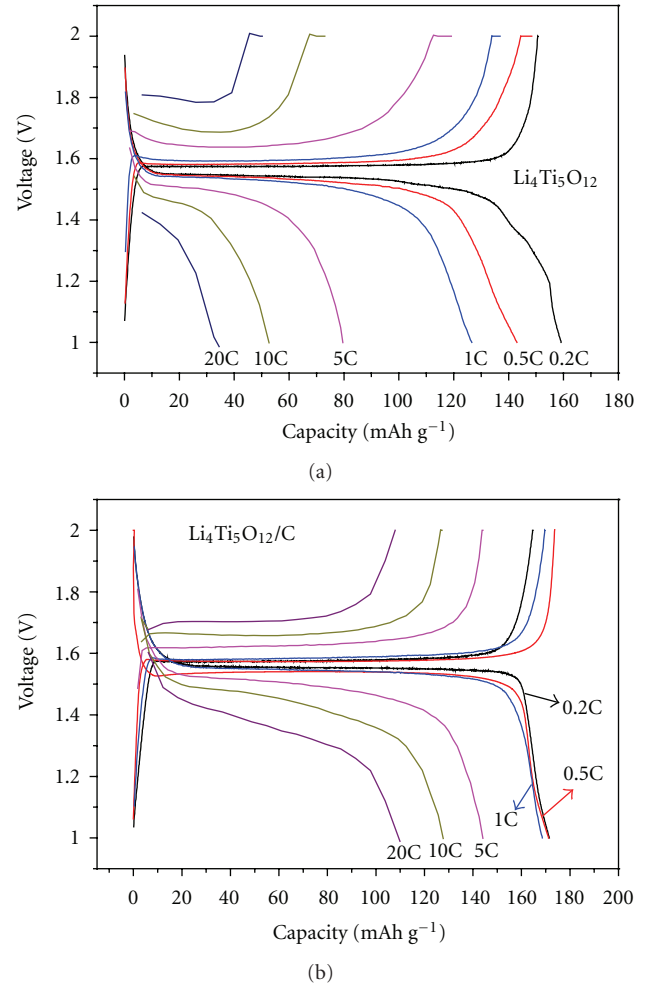


FIGURE 4: The initial charge/discharge profiles of spinel $\text{Li}_4\text{Ti}_5\text{O}_{12}$ (a) and $\text{Li}_4\text{Ti}_5\text{O}_{12}/\text{C}$ (b) at various rates from 0.2C to 20C.

and 0.2C rates. Figure 5(b) shows the cycle performance of the $\text{Li}_4\text{Ti}_5\text{O}_{12}/\text{C}$ electrode at 1C and 20C. The initial specific discharge capacity of $\text{Li}_4\text{Ti}_5\text{O}_{12}/\text{C}$ is 168.6 mAh g^{-1} at 1C, and it retains 87% after 500 cycles. At 20C cycle rate, the sample exhibits an initial discharge capacity of 110 mAh g^{-1} in Figure 5(b), and there is no apparent capacity fading in the 1st~1000th cycles at 20C, indicating excellent rate performance of the material. After 2000 cycles, the capacity remains 73% of initial value. Compared to the literature data, the performance of the $\text{Li}_4\text{Ti}_5\text{O}_{12}$ and $\text{Li}_4\text{Ti}_5\text{O}_{12}/\text{C}$ composites synthesized by starch-sol-assisted rheological phase method in this work is superior to those reported in [4, 6, 24–28]. This cycle performance can be ascribed to the fact that the $\text{Li}_4\text{Ti}_5\text{O}_{12}$ itself has a low volume expansion structure, and the cohesive carbon coating that resulted from the starch sol rheological phase method increased electrical conductivity in $\text{Li}_4\text{Ti}_5\text{O}_{12}/\text{C}$.

EIS technique has been considered as an effective way to identify diffusion phenomena in electronic and ionic conductors. To study conductivities of the $\text{Li}_4\text{Ti}_5\text{O}_{12}/\text{C}$ and $\text{Li}_4\text{Ti}_5\text{O}_{12}$, EIS measurements were carried out at 1.55 V at

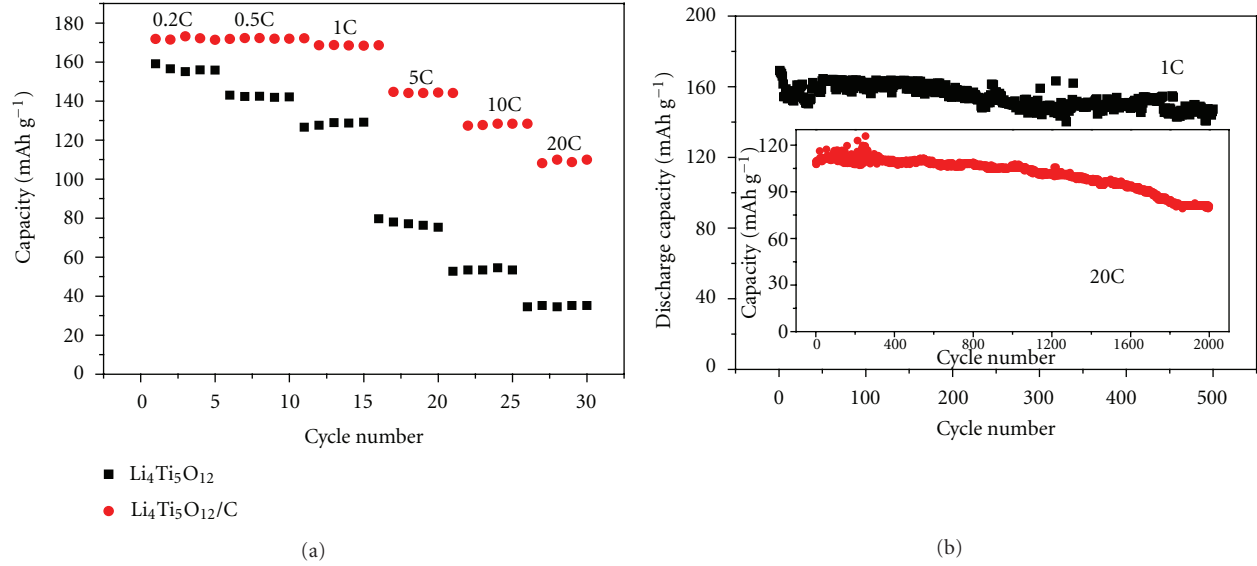


FIGURE 5: Comparison of rate capability of pure $\text{Li}_4\text{Ti}_5\text{O}_{12}$ and $\text{Li}_4\text{Ti}_5\text{O}_{12}/\text{C}$ at various rates (a). Cycle performance of the $\text{Li}_4\text{Ti}_5\text{O}_{12}/\text{C}$ electrode at 1C and 20C rates (b).

room temperature. The Nyquist plots of $\text{Li}_4\text{Ti}_5\text{O}_{12}/\text{C}$ and $\text{Li}_4\text{Ti}_5\text{O}_{12}$ electrodes as well as the fitting results using an equivalent circuit are given in Figure 6. Both Nyquist plots are composed of a depressed semicircle in high frequency and a straight line in low frequency region in Figure 6(a). The solution resistance R_s of the cell from Z' axis interception at high frequency includes both electrolyte and electrode contact resistance. The charge transfer resistance R_{ct} is determined by the semicircle in the middle frequency range, which is mainly related to the electrochemical reaction at the electrolyte/electrode interface. The straight line in low frequency range is attributed to the Warburg impedance Z_w , which is due to the solid-state diffusion of Li^+ ions into the bulk of active material. It can be seen from Figure 6(a) that the $\text{Li}_4\text{Ti}_5\text{O}_{12}/\text{C}$ electrode displayed a much lower impedance than that of pure $\text{Li}_4\text{Ti}_5\text{O}_{12}$ which is similarly observed in [16, 29].

The equivalent circuit model is depicted in Figure 6(b), where the R_s and R_{ct} are solution resistance and charge transfer resistance, respectively. CPE is the constant phase-angle element, involving double layer capacitance of the electrolyte-electrode interface. R_f is the surface polarization resistance, and the C_f is the surface capacitance. The equivalent circuit model is well suited to the fitting of experiment data, and the simulation results of the EIS data for the $\text{Li}_4\text{Ti}_5\text{O}_{12}/\text{C}$ and $\text{Li}_4\text{Ti}_5\text{O}_{12}$ electrodes are given in Table 1. It can be seen that the R_s and R_{ct} are much smaller for the $\text{Li}_4\text{Ti}_5\text{O}_{12}/\text{C}$ electrode ($R_s = 1.92 \Omega$, $R_{ct} = 24 \Omega$) than for the pure $\text{Li}_4\text{Ti}_5\text{O}_{12}$ ($R_s = 3.33 \Omega$, $R_{ct} = 107 \Omega$). This result indicates that the carbon coating has enabled easier charge transfer at electrode/electrolyte interface, and the overall battery internal resistance is also decreased. The electrode polarization resistance of $\text{Li}_4\text{Ti}_5\text{O}_{12}/\text{C}$ ($R_f = 0.184 \Omega$) is much smaller than that of $\text{Li}_4\text{Ti}_5\text{O}_{12}$ ($R_f = 1.08 \Omega$), which implies that the carbon reduced the polarization. The results

are also consistent with the charge/discharge curves shown in Figure 4. The two values of Z_w are almost identical; this is reasonable since the Li^+ diffusion rate in $\text{Li}_4\text{Ti}_5\text{O}_{12}$ crystal lattice should be independent of carbon coating. The *in situ* starch sol coating in the synthesis of $\text{Li}_4\text{Ti}_5\text{O}_{12}$ significantly enhances the conductivity of $\text{Li}_4\text{Ti}_5\text{O}_{12}$ material. The adhesive conductive carbon coating facilitates electronic conductive paths in the $\text{Li}_4\text{Ti}_5\text{O}_{12}$ particle surroundings, that is considered a key factor in improving the discharge capacity, rate capability, and cycle life of the $\text{Li}_4\text{Ti}_5\text{O}_{12}/\text{C}$ material.

4. Conclusions

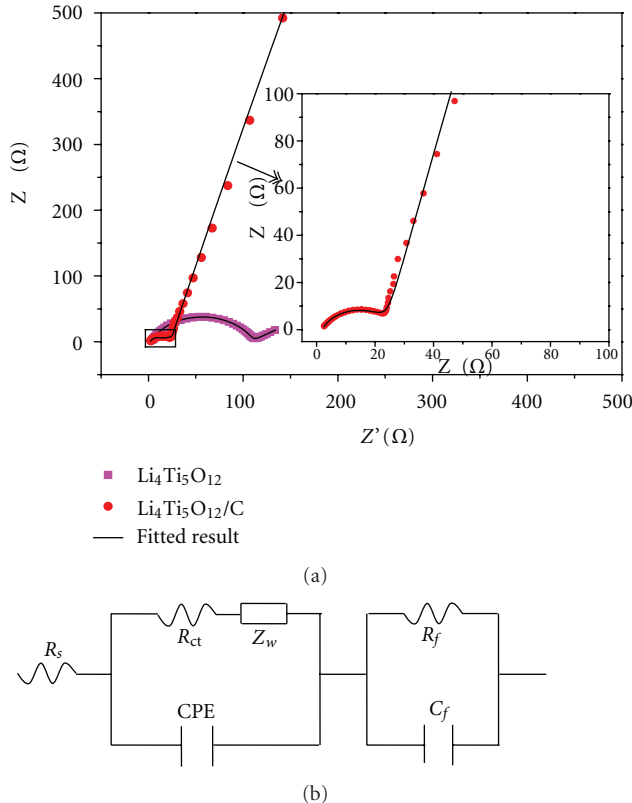
With the starch precursor as carbon source, the carbon was cohesively coated on the surface of $\text{Li}_4\text{Ti}_5\text{O}_{12}$ crystallites in the $\text{Li}_4\text{Ti}_5\text{O}_{12}/\text{C}$ composite by using starch-sol-assisted rheological phase method. This synthesis approach is relatively simple and effective to obtain the high electronic conductive material. The electrochemical characterization indicates that the $\text{Li}_4\text{Ti}_5\text{O}_{12}/\text{C}$ exhibits high rate capability and long cycle life compared to pure $\text{Li}_4\text{Ti}_5\text{O}_{12}$ from solid-state method. The $\text{Li}_4\text{Ti}_5\text{O}_{12}/\text{C}$ anode shows specific capacity of 168.6 mAh g^{-1} at 1C and 110 mAh g^{-1} at 20C, and the discharge capacity retains 73% after 2000 cycles at 20C cycle rate. The excellent rate capability and cycling performance of $\text{Li}_4\text{Ti}_5\text{O}_{12}/\text{C}$ are mainly attributed to the cohesive carbon coating that enhances conductivity and to the intrinsic structural stability of $\text{Li}_4\text{Ti}_5\text{O}_{12}$ that allows reversible Li^+ intercalation in charge-discharge process.

Acknowledgments

The authors are grateful for funding support from the Natural Science Foundation of China (project no. 61004092).

TABLE 1: EIS simulation parameters of $\text{Li}_4\text{Ti}_5\text{O}_{12}$ and $\text{Li}_4\text{Ti}_5\text{O}_{12}/\text{C}$ from the equivalent circuit.

Sample	R_s ($\Omega \text{ cm}^2$)	R_{ct} ($\Omega \text{ cm}^2$)	CPE ($S^n \text{ cm}^{-2}$)	W ($\text{S}^{0.5} \text{ cm}^{-2}$)	R_f ($\Omega \text{ cm}^2$)	C_f ($\text{S}^n \text{ cm}^{-2}$)
$\text{Li}_4\text{Ti}_5\text{O}_{12}$	3.33	107	2.5×10^{-4}	2.55×10^{-4}	1.08	8.66×10^{-6}
$\text{Li}_4\text{Ti}_5\text{O}_{12}/\text{C}$	1.92	24	2.45×10^{-4}	2.2×10^{-4}	0.184	2.72×10^{-6}

FIGURE 6: EIS Nyquist plots of the $\text{Li}_4\text{Ti}_5\text{O}_{12}$ and $\text{Li}_4\text{Ti}_5\text{O}_{12}/\text{C}$ electrode (a) and the corresponding equivalent circuit model that is used to fit the experimental data (b).

References

- [1] L. Yuan, R. Cai, P. Gu, and Z. Shao, "Synthesis of lithium insertion material $\text{Li}_4\text{Ti}_5\text{O}_{12}$ from rutile TiO_2 via surface activation," *Journal of Power Sources*, vol. 195, no. 9, pp. 2883–2887, 2010.
- [2] L. Zhao, Y.-S. Hu, H. Li, Z. Wang, and L. Chen, "Porous $\text{Li}_4\text{Ti}_5\text{O}_{12}$ coated with N-doped carbon from ionic liquids for Li-ion batteries," *Advanced Materials*, vol. 23, no. 11, pp. 1385–1388, 2011.
- [3] M. M. Rahman, J.-Z. Wang, M. F. Hassan, D. Wexler, and H. K. Liu, "Amorphous carbon coated high grain boundary density dual phase $\text{Li}_4\text{Ti}_5\text{O}_{12}\text{-TiO}_2$: a nanocomposite anode material for Li-ion batteries," *Advanced Energy Materials*, vol. 1, no. 2, pp. 212–220, 2011.
- [4] Y. Wang, H. Liu, K. Wang, H. Eiji, Y. Wang, and H. Zhou, "Synthesis and electrochemical performance of nano-sized $\text{Li}_4\text{Ti}_5\text{O}_{12}$ with double surface modification of Ti(III) and carbon," *Journal of Materials Chemistry*, vol. 19, no. 37, p. 6789, 2009.
- [5] K. Amine, I. Belharouak, Z. Chen et al., "Nanostructured anode material for high-power battery system in electric vehicles," *Advanced Materials*, vol. 22, no. 28, pp. 3052–3057, 2010.
- [6] L. Shen, C. Yuan, H. Luo, X. Zhang, K. Xu, and F. Zhang, "In situ growth of $\text{Li}_4\text{Ti}_5\text{O}_{12}$ on multi-walled carbon nanotubes: novel coaxial nanocables for high rate lithium ion batteries," *Journal of Materials Chemistry*, vol. 21, no. 3, pp. 761–767, 2011.
- [7] K.-S. Park, A. Benayad, D. J. Kang, and S. G. Doo, "Nitridation-driven conductive $\text{Li}_4\text{Ti}_5\text{O}_{12}$ for lithium ion batteries," *Journal of the American Chemical Society*, vol. 130, no. 45, pp. 14930–14931, 2008.
- [8] J. Wolfenstine and J. L. Allen, "Electrical conductivity and charge compensation in Ta doped $\text{Li}_4\text{Ti}_5\text{O}_{12}$," *Journal of Power Sources*, vol. 180, no. 1, pp. 582–585, 2008.
- [9] S. Huang, Z. Wen, X. Zhu, and Z. Lin, "Effects of dopant on the electrochemical performance of $\text{Li}_4\text{Ti}_5\text{O}_{12}$ as electrode material for lithium ion batteries," *Journal of Power Sources*, vol. 165, no. 1, pp. 408–412, 2007.
- [10] L. Cheng, J. Yan, G.-N. Zhu, J.-Y. Luo, C.-X. Wang, and Y.-Y. Xia, "General synthesis of carbon-coated nanostructure $\text{Li}_4\text{Ti}_5\text{O}_{12}$ as a high rate electrode material for Li-ion intercalation," *Journal of Materials Chemistry*, vol. 20, no. 3, pp. 595–602, 2010.
- [11] A. D. Robertson, L. Trevino, H. Tukamoto, and J. T. S. Irvine, "New inorganic spinel oxides for use as negative electrode materials in future lithium-ion batteries," *Journal of Power Sources*, vol. 81–82, pp. 352–357, 1999.
- [12] S. Shi, C. Ouyang, M. Lei, and W. Tang, "Effect of Mg-doping on the structural and electronic properties of LiCoO_2 : a first-principles investigation," *Journal of Power Sources*, vol. 171, no. 2, pp. 908–912, 2007.
- [13] P. Kubiak, A. Garcia, M. Womes et al., "Phase transition in the spinel $\text{Li}_4\text{Ti}_5\text{O}_{12}$ induced by lithium insertion-influence of the substitutions Ti/V, Ti/Mn, Ti/Fe," *Journal of Power Sources*, vol. 119–121, pp. 626–630, 2003.
- [14] S. Huang, Z. Wen, B. Lin, J. Han, and X. Xu, "The high-rate performance of the newly designed $\text{Li}_4\text{Ti}_5\text{O}_{12}/\text{Cu}$ composite anode for lithium ion batteries," *Journal of Alloys and Compounds*, vol. 457, no. 1–2, pp. 400–403, 2008.
- [15] A. Sivashanmugam, S. Gopukumar, R. Thirunakaran, C. Nithya, and S. Prema, "Novel $\text{Li}_4\text{Ti}_5\text{O}_{12}/\text{Sn}$ nano-composites as anode material for lithium ion batteries," *Materials Research Bulletin*, vol. 46, no. 4, pp. 492–500, 2011.
- [16] T. Yuan, X. Yu, R. Cai, Y. Zhou, and Z. Shao, "Synthesis of pristine and carbon-coated $\text{Li}_4\text{Ti}_5\text{O}_{12}$ and their low-temperature electrochemical performance," *Journal of Power Sources*, vol. 195, no. 15, pp. 4997–5004, 2010.
- [17] H.-G. Jung, J. Kim, B. Scrosati, and Y. K. Sun, "Micron-sized, carbon-coated $\text{Li}_4\text{Ti}_5\text{O}_{12}$ as high power anode material for

- advanced lithium batteries," *Journal of Power Sources*, vol. 196, no. 18, pp. 7763–7766, 2011.
- [18] W. Tang, S. Tian, L. L. Liu et al., "Nanochain LiMn_2O_4 as ultra-fast cathode material for aqueous rechargeable lithium batteries," *Electrochemistry Communications*, vol. 13, no. 2, pp. 205–208, 2011.
- [19] V. Singh, S. K. Singh, S. Pandey, and P. Kumar, "Sol-gel synthesis and characterization of adsorbent and photoluminescent nanocomposites of starch and silica," *Journal of Non-Crystalline Solids*, vol. 357, no. 1, pp. 194–201, 2011.
- [20] Y. Huang, H. Ren, S. Yin, Y. Wang, Z. Peng, and Y. Zhou, "Synthesis of LiFePO_4/C composite with high-rate performance by starch sol assisted rheological phase method," *Journal of Power Sources*, vol. 195, no. 2, pp. 610–613, 2010.
- [21] S. C. Lee, S. M. Lee, J. W. Lee et al., "Spinel $\text{Li}_4\text{Ti}_5\text{O}_{12}$ nanotubes for energy storage materials," *Journal of Physical Chemistry C*, vol. 113, no. 42, pp. 18420–18423, 2009.
- [22] M. Hirayama, K. Kim, T. Toujigamori, W. Cho, and R. Kanno, "Epitaxial growth and electrochemical properties of $\text{Li}_4\text{Ti}_5\text{O}_{12}$ thin-film lithium battery anodes," *Dalton Transactions*, vol. 40, no. 12, pp. 2882–2887, 2011.
- [23] L. Kavan, J. Prochazka, T. M. Spitzler et al., "Li insertion into $\text{Li}_4\text{Ti}_5\text{O}_{12}$ (Spinel)," *Journal of The Electrochemical Society*, vol. 150, no. 7, pp. A1000–A1007, 2003.
- [24] L. Shen, C. Yuan, H. Luo, X. Zhang, K. Xu, and Y. Xia, "Facile synthesis of hierarchically porous $\text{Li}_4\text{Ti}_5\text{O}_{12}$ microspheres for high rate lithium ion batteries," *Journal of Materials Chemistry*, vol. 20, no. 33, pp. 6998–7004, 2010.
- [25] G. Xie, J. Ni, X. Liao, and L. Gao, "Filter paper templated synthesis of chain-structured $\text{Li}_4\text{Ti}_5\text{O}_{12}/\text{C}$ composite for Li-ion batteries," *Materials Letters*, vol. 78, pp. 177–179, 2012.
- [26] G. F. Yan, H. Fang, H. Zhao, G. Li, Y. Yang, and L. Li, "Ball milling-assisted sol-gel route to $\text{Li}_4\text{Ti}_5\text{O}_{12}$ and its electrochemical properties," *Journal of Alloys and Compounds*, vol. 470, no. 1-2, pp. 544–547, 2009.
- [27] J. Gao, C. Jiang, J. Ying, and C. Wan, "Preparation and characterization of high-density spherical $\text{Li}_4\text{Ti}_5\text{O}_{12}$ anode material for lithium secondary batteries," *Journal of Power Sources*, vol. 155, no. 2, pp. 364–367, 2006.
- [28] Y. Qiao, X. Luo, Y. Liu, and Y. Huang, "Li₄Ti₅O₁₂ nanocrystals for high-rate lithium-ion batteries synthesized by a rapid microwave-assisted solid-state process," *Electrochimica Acta*, vol. 63, no. 29, pp. 118–123, 2012.
- [29] L. Yang and J. Gao, " $\text{Li}_4\text{Ti}_5\text{O}_{12}/\text{C}$ composite electrode material synthesized involving conductive carbon precursor for Li-ion battery," *Journal of Alloys and Compounds*, vol. 485, no. 1-2, pp. 427–434, 2009.

Research Article

Influence of ITO-Silver Wire Electrode Structure on the Performance of Single-Crystal Silicon Solar Cells

Wern-Dare Jheng

Department of Mechanical Engineering, National Chin-Yi University of Technology, Number 57, Section 2, Chung-Shan Road, Taiping 411, Taichung, Taiwan

Correspondence should be addressed to Wern-Dare Jheng, jwd@ncut.edu.tw

Received 29 January 2012; Accepted 13 May 2012

Academic Editor: Arava Leela Mohana Reddy

Copyright © 2012 Wern-Dare Jheng. This is an open access article distributed under the Creative Commons Attribution License, which permits unrestricted use, distribution, and reproduction in any medium, provided the original work is properly cited.

This study aimed to explore the effect of various electrode forms on single-crystal silicon solar cells by changing their front and back electrode structures. The high light penetration depth of the Indium Tin Oxide (ITO) and the high conductivity of the silver wire that were coated on the single crystal silicon solar cells increased photoelectron export, thus increasing the efficiency of the solar cell. The experiment utilized a sol-gel solution containing phosphorus that was spin coated on single-crystal silicon wafers; this phosphorus also served as a phosphorus diffusion source. A p-n junction was formed after annealing at high temperature, and the substrate was coated with silver wires and ITO films of various structures to produce the electrodes. This study proposed that applying a heat treatment to the aluminum of back electrodes would result in a higher efficiency for single-crystal silicon solar cells, whereas single-crystal silicon solar cells containing front electrodes with ITO film coated with silver wires would result in efficiencies that are higher than those achieved using pure ITO thin-film electrodes.

1. Introduction

Since the industrial revolution, energy has been harnessed from petroleum and coal; however, these two sources are exhaustible. Moreover, large amounts of carbon dioxide emitted from fuel-generating energy have resulted in serious consequences, such as global warming [1]. As a result of countries around the world also beginning to place importance on this issue, the Kyoto Protocol was passed on December 11, 1997. The Protocol requested that 37 industrial countries and European Nations follow the 1990 standards to achieve a 5% reduction in greenhouse gas emissions from 2008 to 2012, and it was the first step in addressing global warming. The Copenhagen Summit in December, 2009 determined the global carbon reduction target for 2012–2017 in an attempt to prevent an irreversibly damaged climate. Presently, clean, renewable energy is the best solution to the global warming issues addressed by these initiatives. Because solar power is currently the cleanest and most feasible solution, several researchers are studying the solar cell for its potential in addressing these problems [2, 3].

Currently, commercial single-crystal silicon solar cells use silver grid electrodes as front electrodes [4, 5], which have

a light obscuration rate of approximately 5–9%. Moreover, when electrons iterate to the surface of n-type semiconductors, they are susceptible to capture by dangling bonds. Silica is most commonly used as the passivation layer and the antireflection layer for single-crystal silicon solar cells [6]. However, because it lacks a conducting path for electrons, it cannot be used for electrodes. Therefore, this study employs ITO with high transmittance and conductivity characteristics [7–10] as the antireflection layer and conducting electrodes for single-crystal silicon solar cells. This study also explores the effect of adding high-conductivity silver wire on single-crystal silicon solar cells.

2. Experiment

2.1. p-n Diode Production

2.1.1. Specimen Pretreatment [11]. The substrate was a silicon wafer (p-type) with the dimensions of $156 \times 156 \text{ mm}^2$ (lattice directions 100, resistivity $0.5 \sim 3 \Omega\text{-cm}$, thickness $200 \mu\text{m}$) cut into silicon chips of size $1.5 \times 1.5 \text{ cm}^2$. The following cleaning steps were performed. First, the silicon

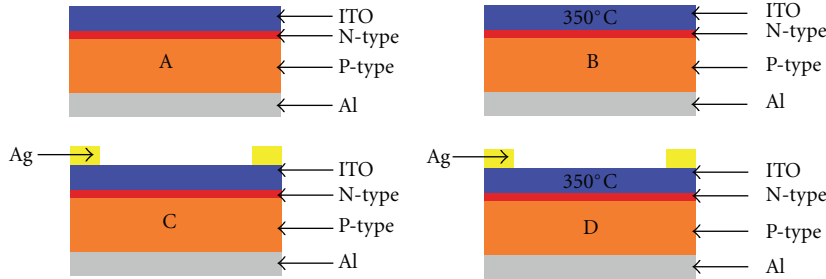


FIGURE 1: Single crystal silicon solar cells of different structure.

chips were immersed in a mixture of H_2SO_4 (98%) and H_2O_2 (30%) in a configured ratio of 3:1 for 10 minutes while the temperature was maintained at 80°C. The silicon chips were then removed and rinsed with deionized water. Next, the chips were immersed in a mixture of NH_4OH (29%), H_2O_2 (30%), and H_2O in a ratio of 1:1:5 for 10 minutes while the temperature was maintained at 80°C. The silicon chips were then rinsed again with deionized water for five minutes. Finally, the chips were immersed in buffer oxide etch (BOE) solution for one minute to remove the silicon oxide layer. The chips were blow-dried after cleansing.

2.1.2. Sol-Gel Configuration. This study used the sol-gel method for modulating phosphorus chemicals. The solution contained 4.69 g of polyethylene glycol, 18 g of ethanol, 0.563 g of H_2O , and 0.555 g of phosphorus pentoxide; the solution was stirred in a magnetic rotator for two hours to ensure that the solution was completely mixed.

2.1.3. Phosphorus Diffusion Process. The sol-gel configuration was spin coated onto single-crystal silicon. The spin coating was divided into two phases. The first phase consisted of a rotation speed of 2,000 rpm for a total of 10 seconds and was then followed by a second phase that consisted of a rotation speed of 6,000 rpm for a total of 10 seconds. The silicon was placed on a heating plate, where it underwent two-stage heating. During the first stage, a temperature of 120°C was maintained for 15 minutes to evaporate the solvent; during the second stage, a temperature of 200°C was maintained for 20 minutes. Subsequently, the silicon was placed inside a high-temperature furnace at a temperature of 900°C for 10 minutes so that it could undergo phosphorus diffusion. Upon completion of diffusion, a BOE solution was used to etch the phosphate glass for five minutes.

2.2. Electrode Production

2.2.1. Back Electrode Production. A magnetron sputter was used to coat the back of single-crystal silicon (of p-n structure) with aluminum. The sputtering power was 100 W, the work pressure was 5×10^{-3} Torr, and the sputtering time was 30 minutes; these parameters resulted in an aluminum thickness of 500 nm.

2.2.2. High-Temperature Sintering Process. The single-crystal silicon was thermally annealed to increase the bond strength

between the metal and silicon, to export electrons and to produce back surface field structure. The annealing was performed at 650°C for 20 minutes.

2.2.3. Preparation of Transparent Conductive Film. An RF magnetron sputter was used to produce a coat of ITO. The sputtering power was 80 W, the work pressure was 3×10^{-3} Torr, and the sputtering time was 20 minutes. These parameters resulted in a 450 nm thick ITO film.

2.2.4. Transparent Conductive Film Annealing. Single-crystal silicon covered with an ITO electrode underwent a thermal annealing treatment to increase its light penetration depth and conductivity. The annealing temperature was maintained at 350°C for 30 minutes.

2.2.5. Silver Wire Coating. The front of single-crystal silicon was sputtered with silver wire using a magnetic sputter. The sputtering power was 50 W, the work pressure was 1×10^{-3} Torr, and the sputtering time was 10 minutes; these parameters produced a silver thickness of 300 nm.

2.3. Electrode Structure. This study explored the effect of electrode structure on single-crystal silicon via changing the front and back electrode production processes. The study examined four different electrode structures: A, B, C, and D. Each structure contained a heat-treated aluminum electrode and an aluminum electrode that had not been heat-treated. Structure A used ITO film as the front electrode, structure B used annealed ITO film as the front electrode, structure C used ITO film covered with silver wire as the front electrode, and structure D used annealed ITO film covered with silver wire as the front electrode. A, B, C, and D are solar cell structures, as shown in Figure 1.

3. Results and Discussion

3.1. Analysis of p-n Junction Properties. The resistance of single-crystal silicon after phosphorus diffusion was approximately $40 \Omega/\text{sq}$. with a mixed concentration of $10^{19} \text{ atom}/\text{cm}^{-3}$. The n-type silicon work function (W_S) was 4.07 eV, and the ITO work function of the experiment (W_m) was 3.8 eV, which met the conditions for metal-semiconductor ohmic contact ($W_m < W_S$).

The p-n junction solar cells are diodes that may be used to speculate the characteristics of single-crystal silicon

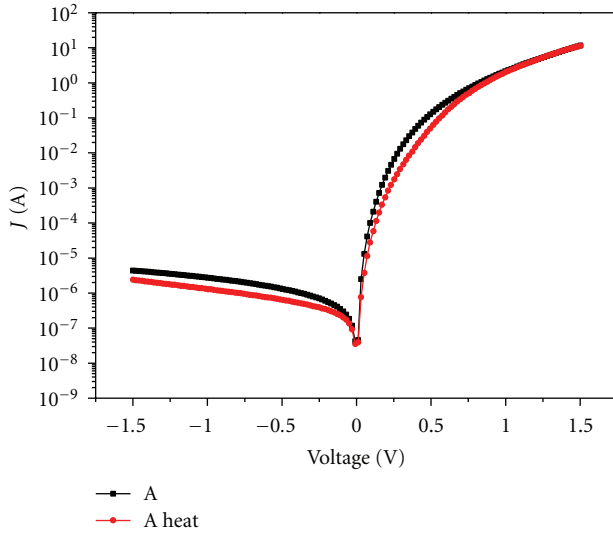


FIGURE 2: Dark current-voltage curve of structure A.

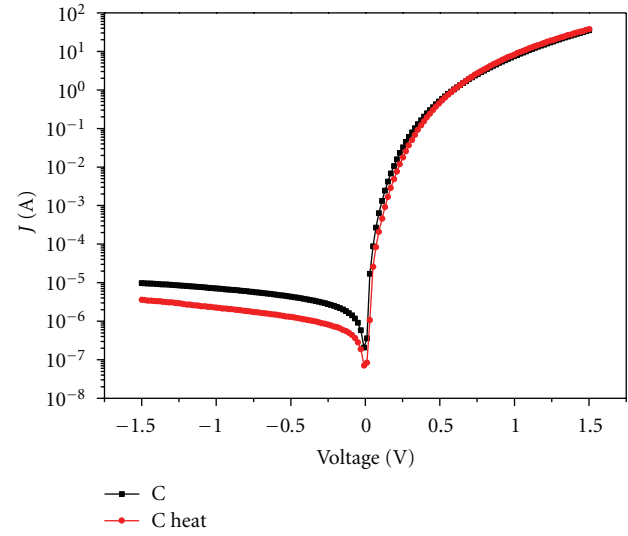


FIGURE 4: Dark current-voltage curve of structure C.

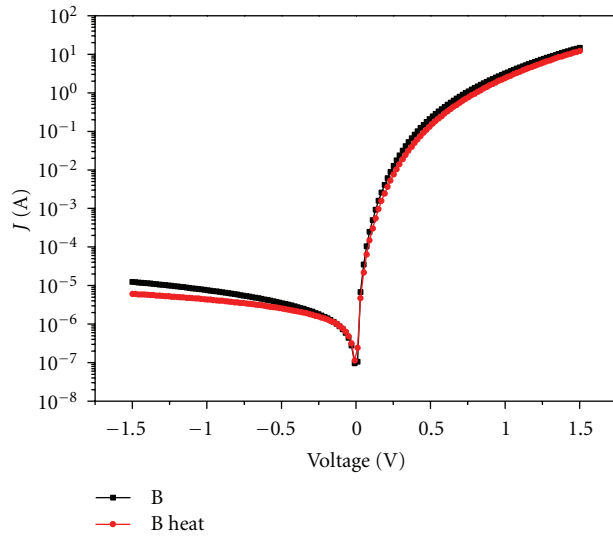


FIGURE 3: Dark current-voltage curve of structure B.

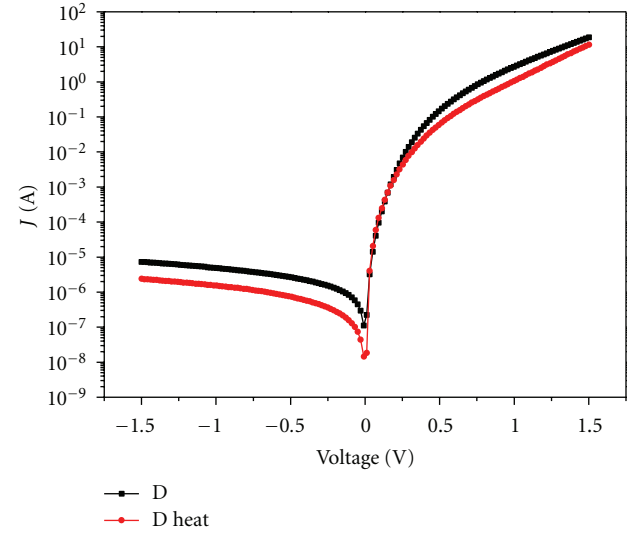


FIGURE 5: Dark current-voltage curve of structure D.

solar cells through dark current analysis of various electrode structures. The dark current-voltage curve in conjunction may be used to calculate the diode ideality factor (n value) [12, 13].

The dark current-voltage curve was measured on various electrode structures. Logarithmic coordinates were obtained from the current to obtain Figures 2, 3, 4, and 5 and then to obtain diode ideality factors (n). As shown in structure A in Figure 6, the n value calculated from the aluminum electrode before the heat treatment was 2.33, whereas the diode ideality factor following heat treatment of aluminum electrodes was 2.44. For single-crystal silicon solar cells with structure B, the n value calculated from the aluminum electrode before heat treatment was 1.72; the diode ideality factor after heat

treatment of the aluminum electrodes was 2.32. For single-crystal silicon solar cells of structure C, the n value calculated from the aluminum electrode before heat treatment was 1.96; the diode ideality factor after heat treatment of the aluminum electrodes was 2.76. For single-crystal silicon solar cells of structure D, the n value calculated from the aluminum electrode before heat treatment was 2.11; the diode ideality factor after heat treatment of the aluminum electrodes was 2.81.

By performing the aforementioned analyses, we discovered that for the four different electrode structures, the diode ideality factor (n) increased when the aluminum electrodes were heat treated. Such a phenomenon implied that applying heat treatment to an aluminum back electrode would enhance the performance of p-n junction single-crystal silicon solar cells.

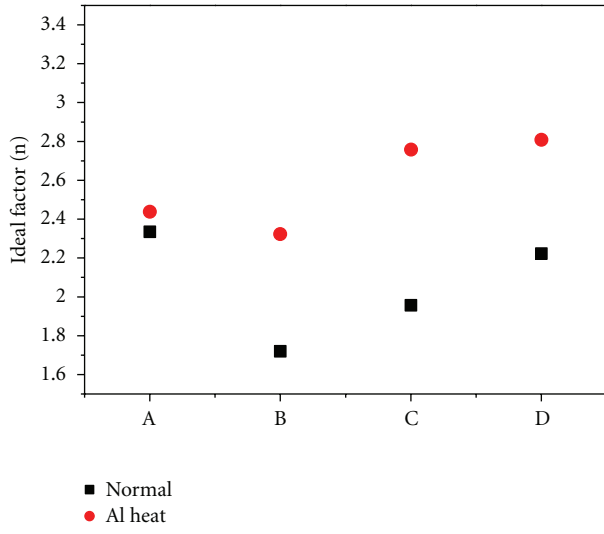


FIGURE 6: Ideality factors under different structure.

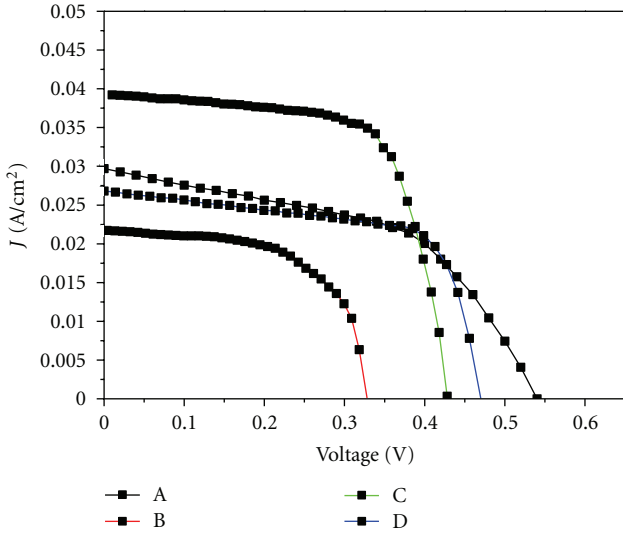


FIGURE 7: Current-voltage curve under different structure.

3.2. Analysis of Optoelectronic Properties. The light source employed by this study was an AM1.5, which has an incident light source intensity of 100 mW/cm^2 . The current-voltage curve for this lighting is shown in Figures 7 and 8.

3.2.1. Effect of Front Electrode Structure on Optoelectronic Properties. This study first probed the optoelectronic properties of single-crystal silicon solar cells with two different structures: a front electrode using pure ITO film (structure A) and a front electrode using ITO film combined with silver wire (structure C). The data were compiled in Figures 9–11 according to Figures 7 and 8. Structure A resulted in an optoelectronic conversion efficiency of 7.98%, open-circuit voltage of 0.53 V, and short-circuit current of 29.748 mA/cm^2 . In comparison, structure C yielded improved optoelectronic properties; the photoelectric conversion efficiency increased

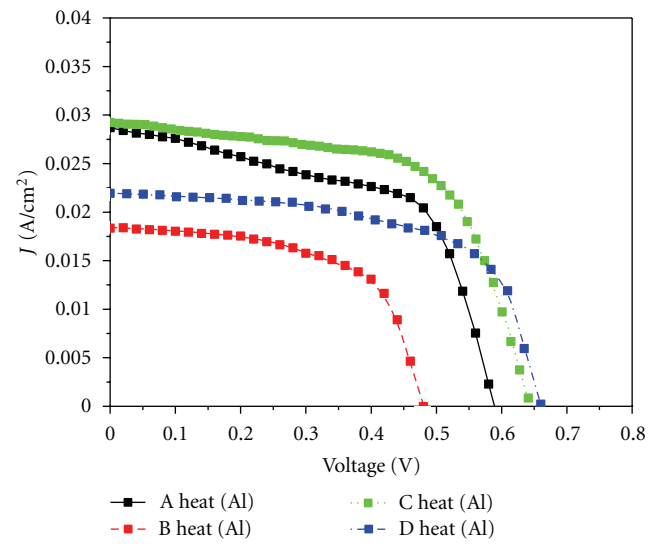


FIGURE 8: Current-voltage curve of aluminum undergone heat treatment under different structure.

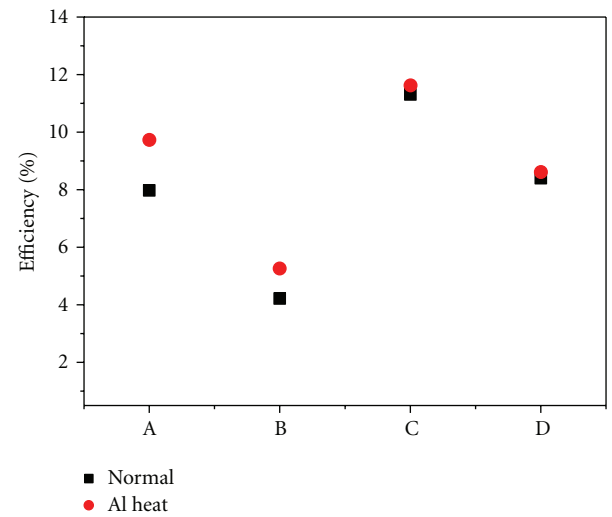


FIGURE 9: Efficiency map under different structure.

to 11.31%, the open-circuit voltage increased to 0.42 V and the short-circuit current increased to 39.214 mA/cm^2 .

Subsequently, structures B and D with heat treatment applied to the ITO were compared. Structure D (covered with silver wire) resulted in an open-circuit voltage (0.47 V), short-circuit current (26.810 mA/cm^2) and optoelectronic conversion efficiency (8.40%) that were all higher than the open-circuit voltage (0.33 V), short-circuit current (21.527 mA/cm^2), and optoelectronic conversion efficiency (4.22%) that resulted from structure B.

These results show that ITO covered with silver wire promotes rapid export of photoelectrons and substantially improves its efficiency.

This study then examined the impact of ITO heat treatment on single-crystal silicon solar cells by comparing structure A with structure B and structure C with structure

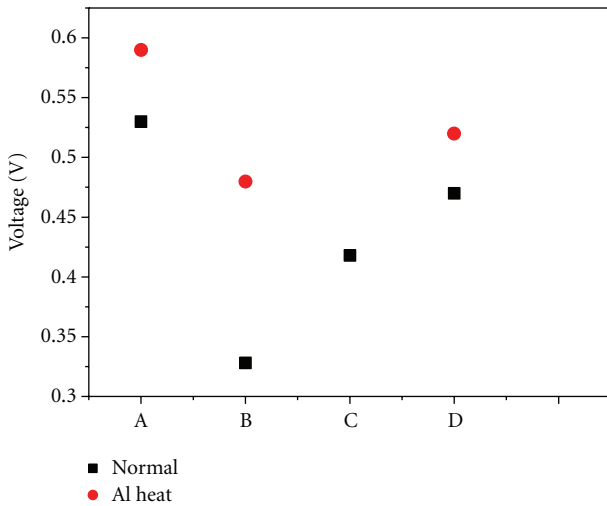


FIGURE 10: Open-circuit voltage under different structure.

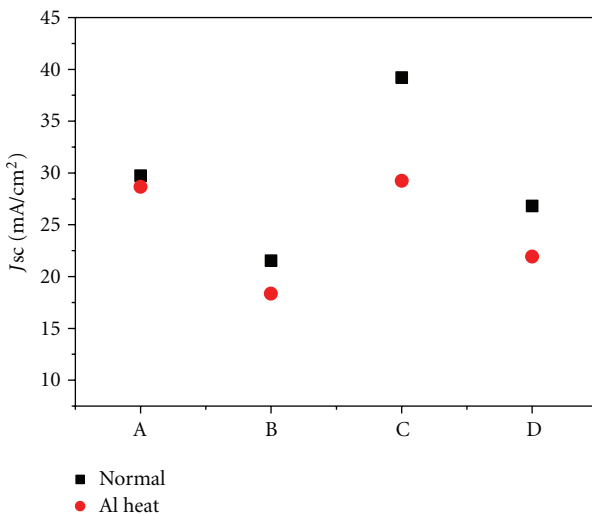


FIGURE 11: Short-circuit current under different structure.

D. The following results were obtained. The ITO film with structure A was used as the front electrode that exhibited higher efficiency; the optoelectronic conversion efficiency was 7.98%, the open-circuit voltage was 0.53 V and the short-circuit current was 29.748 mA/cm². In comparison, the ITO with structure B and a heat treatment of 350°C were used as front electrode that showed a lower efficiency; the optoelectronic conversion efficiency dropped to 4.22%, the open-circuit voltage dropped to 0.33 V and the short-circuit current dropped to 21.527 mA/cm². Next, the optoelectronic properties of structures C and D were compared. The optoelectronic conversion efficiency of structure C was 11.31%, the open-circuit voltage was 0.42 V, and the short-circuit current was 39.214 mA/cm². Upon applying a heat treatment of 350°C to the ITO with structure D, the optoelectronic efficiency decreased to 8.40%, the open-circuit voltage increased to 0.47 V, and the short-circuit current decreased to 26.810 mA/cm². These results show

that ITO causes single-crystal silicon solar cells to decline in overall efficiency upon undergoing a heat treatment of 350°C.

3.2.2. Effect of Heat Treating on the Aluminum Back Electrode.

Figures 9–11 show that the aluminum electrode of structure A produced an open-circuit voltage of 0.53 V, short-circuit current of 29.748 mA/cm² and optoelectronic conversion efficiency of 7.98% before a heat treatment was applied. After applying a heat treatment of 650°C to the aluminum electrode, the open-circuit voltage increased to 0.59 V, the short-circuit current decreased to 28.664 mA/cm², and the optoelectronic conversion efficiency rose to 9.72%. The aluminum electrode of structure B yielded an open-circuit voltage of 0.33 V, a short-circuit current of 21.527 mA/cm², and an optoelectronic conversion efficiency of 4.22% before the heat treatment was applied. After applying the heat treatment of 650°C to the aluminum electrode, the open-circuit voltage increased to 0.48 V, the short-circuit current decreased to 18.355 mA/cm², and the optoelectronic conversion efficiency rose to 5.27%. The aluminum electrode of structure C produced an open-circuit voltage of 0.42 V, a short-circuit current of 39.214 mA/cm², and optoelectronic conversion efficiency of 11.31% before the heat treatment was applied. After applying a heat treatment of 650°C to the aluminum electrode, the open-circuit voltage increased to 0.64 V, the short-circuit current decreased to 29.250 mA/cm², and the optoelectronic conversion efficiency rose to 11.62%. The aluminum electrode of structure C produced an open-circuit voltage of 0.47 V, a short-circuit current of 26.810 mA/cm², and optoelectronic conversion efficiency of 8.40% before the heat treatment was applied. After applying the heat treatment of 650°C to the aluminum electrode, the open-circuit voltage increased to 0.66 V, the short-circuit current decreased to 21.935 mA/cm², and the optoelectronic conversion efficiency rose to 8.62%. These results show that ITO causes single-crystal silicon solar cells to decrease in short-circuit current after undergoing a heat treatment, whereas the open-circuit voltage and optoelectronic conversion efficiency will both increase.

3.2.3. Effect of Inside Impedance.

The equivalent circuit for single-crystal silicon solar cells may be used to derive shunt resistance (R_{sh}), series resistance (R_s) and reverse saturation current (I_0) [14]. R_{sh} proportionally affects open-circuit voltage, whereas R_s inversely affects the short-circuit current.

Figures 10 and 12 show that there is a significant correlation between R_{sh} and open-circuit voltage. Additionally, as shown in Figure 12, R_{sh} significantly increased after applying heat treatment to the aluminum electrode. For structure A, R_{sh} was 299.99 kΩ before applying heat treatment to the aluminum electrode, and R_{sh} rose to 383.71 kΩ after heat treatment. For structure B, R_{sh} was 120 kΩ before applying heat treatment to the aluminum electrode, and R_{sh} rose to 342.85 kΩ after heat treatment. For structure C, R_{sh} was 209.53 kΩ before applying heat treatment to the aluminum electrode, and R_{sh} rose to 379.29 kΩ after heat treatment. For structure D, R_{sh} was 356.73 kΩ before applying heat treatment to the aluminum electrode, and

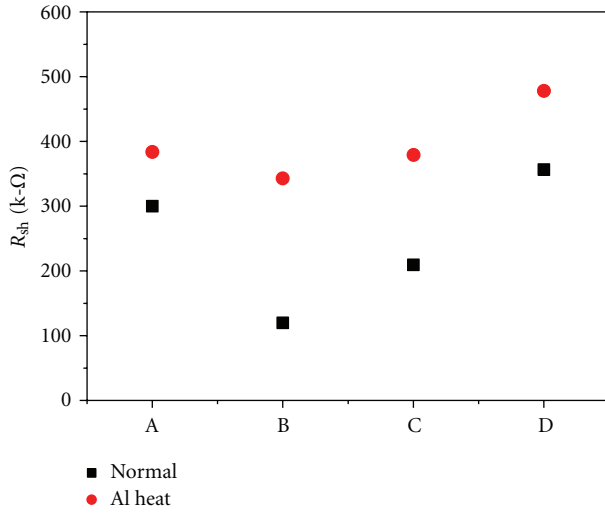


FIGURE 12: R_{sh} Comparison of parallel resistance under different structure.

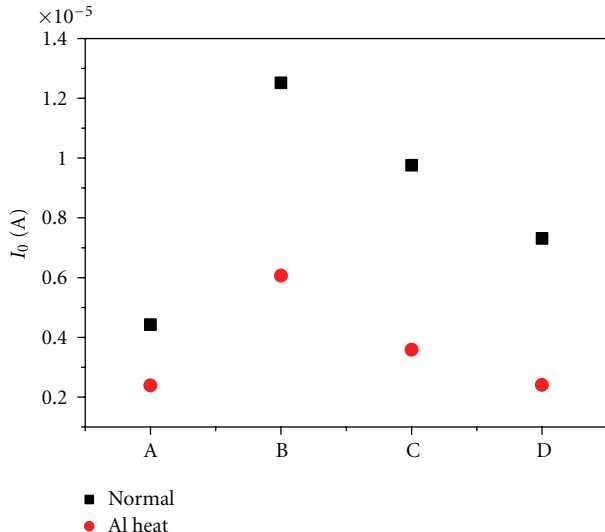


FIGURE 13: Comparison of reserve saturation current under different structure.

R_{sh} rose to $478.24\text{ k}\Omega$ after heat treatment. These results show that R_{sh} increases after applying heat treatment to the aluminum electrode.

The increase in R_{sh} implied a better insulation between the front electrode and back electrode, which would also correspond to a lower reverse saturation current. Reverse saturation currents for different structures are compiled in Figure 13, which shows that the I_0 of structure A was initially $4.43\text{ }\mu\text{A}$, but then decreased to $2.39\text{ }\mu\text{A}$ after heat treatment. The I_0 of structure B was initially $12.52\text{ }\mu\text{A}$, but then decreased to $6.07\text{ }\mu\text{A}$ after heat treatment. The I_0 of structure C was initially $9.76\text{ }\mu\text{A}$, but then decreased to $3.59\text{ }\mu\text{A}$ after heat treatment. The I_0 of structure D was initially $7.31\text{ }\mu\text{A}$, but then decreased to $2.42\text{ }\mu\text{A}$ after heat treatment.

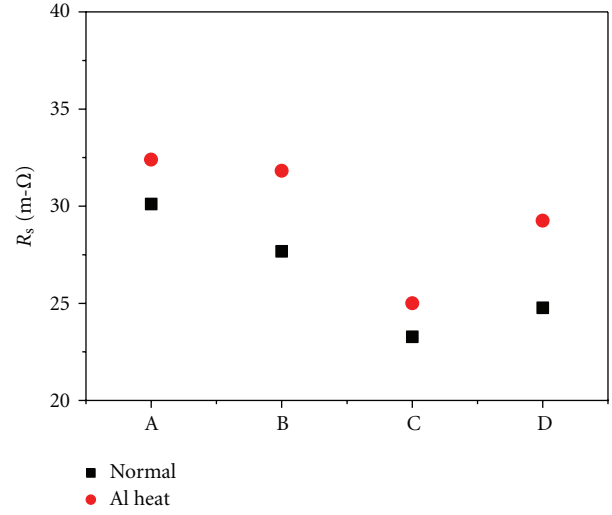


FIGURE 14: R_s Comparison of series resistance under different structure.

Figure 14 illustrates the series resistance (R_s) for different structures. Figures 11 and 14 show that R_s affects the short-circuit current (J_{sc}). After heat treatment, the R_s of structure A rose from $30.12\text{ m}\Omega$ to $32.41\text{ m}\Omega$, and J_{sc} decreased from 29.748 mA/cm^2 to 28.664 mA/cm^2 . After heat treatment, the R_s of structure B rose from $27.68\text{ m}\Omega$ to $31.83\text{ m}\Omega$, and J_{sc} decreased from 21.527 mA/cm^2 to 18.355 mA/cm^2 . After heat treatment, the R_s of structure C rose from $23.28\text{ m}\Omega$ to $25\text{ m}\Omega$, and J_{sc} decreased from 39.214 mA/cm^2 to 29.250 mA/cm^2 . After heat treatment, the R_s of structure D rose from $24.78\text{ m}\Omega$ to $29.26\text{ m}\Omega$, and J_{sc} decreased from 26.810 mA/cm^2 to 21.935 mA/cm^2 . These results show that R_s grew, whereas J_{sc} decreased after heat treatment of the aluminum electrode; this is due to the internal electronic transmission of the semiconductor encountering more obstacles, which thereby lowers the output current.

Moreover, in comparing structure A to structure C and structure B to structure C, we discovered that the electrode of ITO covered with silver wire results in a higher short-circuit current (J_{sc}) and a lower R_s than those produced by the electrode of pure ITO. This indicates that adding the electrode of silver wire reduces the R_s .

4. Conclusion

This study used the sol-gel method to prepare a phosphorus diffusion solution, which was spin coated onto the single-crystal silicon substrate using a 900°C heat diffusion process to form a p-n junction. This substrate was then covered with an ITO layer of variable structure and silver wire as the electrode. The impact of heat treatment on electrode structure was also examined in the study and yielded the following results.

- (1) The average efficiency of single-crystal silicon solar cells increased after applying a 650°C heat treatment to the aluminum electrode.

- (2) The efficiency decreased after applying a 350°C heat treatment to the ITO for 30 minutes, which resulted mainly from a decreasing shunt resistance and an increasing series resistance. This led to a decrease in both open-circuit voltage and short-circuit current, thereby lowering efficiency.
- (3) When comparing the composite electrode of ITO and silver wire with pure ITO, the lower resistance of silver wire substantially enhanced the short-circuit current; however, it also reduced some of the open-circuit voltages. Overall, ITO covered with silver wire increased the optoelectronic efficiency of ITO.
- (4) This study showed that the optimal front electrode structure was ITO covered with silver, which resulted in an 11.62% efficiency when a heat treatment of 650°C was applied to the aluminum metal of the back electrode.

References

- [1] W. U. Huynh, J. J. Dittmer, and A. P. Alivisatos, "Hybrid nano-rod-polymer solar cells," *Science*, vol. 295, no. 5564, pp. 2425–2427, 2002.
- [2] W. He, T. T. Chow, J. Ji, J. Lu, G. Pei, and L. S. Chan, "Hybrid photovoltaic and thermal solar-collector designed for natural circulation of water," *Applied Energy*, vol. 83, no. 3, pp. 199–210, 2006.
- [3] Y. Wang, Z. Fang, L. Zhu, Q. Huang, Y. Zhang, and Z. Zhang, "The performance of silicon solar cells operated in liquids," *Applied Energy*, vol. 86, no. 7-8, pp. 1037–1042, 2009.
- [4] H. Katsumata, T. Ihara, and F. Tatekura, "New technology developments of solar cell fabrication by NEDO," in *Proceedings of the 24th IEEE Photovoltaic Specialists Conference. Part 2*, pp. 2240–2246, December 1994.
- [5] N. B. Mason, T. M. Bruton, and M. Balbuena, "Laser grooved buried grid silicon solar cells from pilot line to 50 MWp manufacture in ten years," in *PV in Europe, Plenary Paper*, pp. 227–229, Rome, Italy, October 2002.
- [6] K. R. McIntosh, N. C. Shaw, and J. E. Cotter, "Light trapping in sunpower's A-300 solar cells," in *Proceedings of the 19th European Photovoltaic Solar Energy Conference*, Paris, France, 2004.
- [7] J. A. Amick, G. L. Schnable, and J. L. Vossen, "Deposition techniques for dielectric films on semiconductor devices," *Journal of Vacuum Science and Technology*, vol. 14, no. 5, pp. 1053–1063, 1977.
- [8] I. Hamberg and C. G. Granqvist, "Evaporated Sn-doped In₂O₃ films: basic optical properties and applications to energy-efficient windows," *Journal of Applied Physics*, vol. 60, no. 11, pp. R123–R160, 1986.
- [9] J. D. Rancourt, *Optical Thin Films: User's Handbook*, 1987.
- [10] C. G. Granqvist, *Handbook of Inorganic Electrochromic Materials*, 1995.
- [11] W.-D. Jheng and C. W. Chen, "Improve the efficiency of silicon solar cells by ITO-silver electrode structure," *ECS Transactions*, vol. 33, pp. 57–60, 2011.
- [12] A. Jain and A. Kapoor, "Exact analytical solutions of the parameters of real solar cells using Lambert W-function," *Solar Energy Materials and Solar Cells*, vol. 81, no. 2, pp. 269–277, 2004.
- [13] A. Jain and A. Kapoor, "A new method to determine the diode ideality factor of real solar cell using Lambert W-function," *Solar Energy Materials and Solar Cells*, vol. 85, no. 3, pp. 391–396, 2005.
- [14] M. Bashahu and P. Nkundabakura, "Review and tests of methods for the determination of the solar cell junction ideality factors," *Solar Energy*, vol. 81, no. 7, pp. 856–863, 2007.

Research Article

High-Efficiency CdS Quantum-Dots-Sensitized Solar Cells with Compressed Nanocrystalline TiO₂ Photoelectrodes

Yanan Wang, Ning Peng, Hongling Li, and Xuduo Bai

Key Laboratory of Functional Inorganic Material Chemistry, Ministry of Education, Heilongjiang University, Harbin 150080, China

Correspondence should be addressed to Xuduo Bai, xuduobai@hotmail.com

Received 26 November 2011; Revised 1 May 2012; Accepted 1 May 2012

Academic Editor: Mauro Coelho dos Santos

Copyright © 2012 Yanan Wang et al. This is an open access article distributed under the Creative Commons Attribution License, which permits unrestricted use, distribution, and reproduction in any medium, provided the original work is properly cited.

Nanocrystalline TiO₂ films were fabricated on titanium substrates by compression method. The CdS quantum dots (QDs) were assembled onto the compressed TiO₂ layers, which serve as sensitizers. A maximum power conversion efficiency of 4.49% is achieved under 100 mW/cm² illumination. In this paper, we find that the compression can help increase the efficiency of the cell by increasing the absorption of the CdS QDs and improving the transportation of photogenerated electrons.

1. Introduction

Dye-sensitized solar cells (DSSCs) have established themselves as an alternative to conventional solar cells owing to their remarkably high power conversion efficiency, longtime stability, and low-cost production [1, 2]. The traditional DSSCs use organic dyes as sensitizers and the power conversion efficiency of 11% has been achieved using ruthenium dyes [3]. In addition to organic dyes, QDs [2, 4–7] can also serve as sensitizers of DSSCs. The use of semiconductor QDs as sensitizer has some advantages compared with the conventional systems. Firstly, the band gap of the nanocrystals can be adjusted by changing their size so that the absorption spectrum can be tuned to match the spectral distribution of sunlight [8]. Secondly, these QDs can use hot electrons or generate multiple charge carriers with a single photon [7].

In the past, QDs-sensitized solar cells usually use a sintered TiO₂ film as the photoelectrode. In such a device, a lot of energy and time is consumed in the fabrication of TiO₂ films; moreover, the power conversion efficiency (η) is mainly limited by the small amount of the QDs on the electrode surface and the electron recombination in the cell [2, 4]. In this study, the TiO₂ film was fabricated using the compression method developed by Anders Hagfeldt and coworkers [9–11]. This method can offer a simple and fast

way to fabricate TiO₂ films; moreover, it was proved that the resulting films are porous and mechanically stable [9, 11]. We expect that this method would help resolve the problems mentioned above.

2. Experiment

In this paper, the TiO₂ paste used was composed of a mixture of commercially available nanosized P25 and ethanol solvent at a concentration of 20 wt%. After ultrasonication, the suspension was applied onto the Ti sheet by hand using doctor blading. Then, pressure (1500 kg/cm²) treatment was applied. CdS QDs were deposited to the TiO₂ film by S-CBD method [5]. A TiO₂ film was dipped into a CdCl₂ water solution (0.05 M) for 30 s, rinsed with water, and dipped for another 30 s into a Na₂S water solution (0.05 M). The two-step dipping procedure is termed as one S-CBD cycle and the incorporated amount of CdS can be increased by repeating the assembly cycles.

The performances of the photoelectrochemical (PEC) solar cells were studied in a three-armed cell with a platinum filament counter electrode and a saturated calomel electrode (SCE) as a reference. 0.1 M Na₂S solution serves as the electrolyte. Measurements were carried out under AM 1.5 G at 100 mW/cm² illumination.

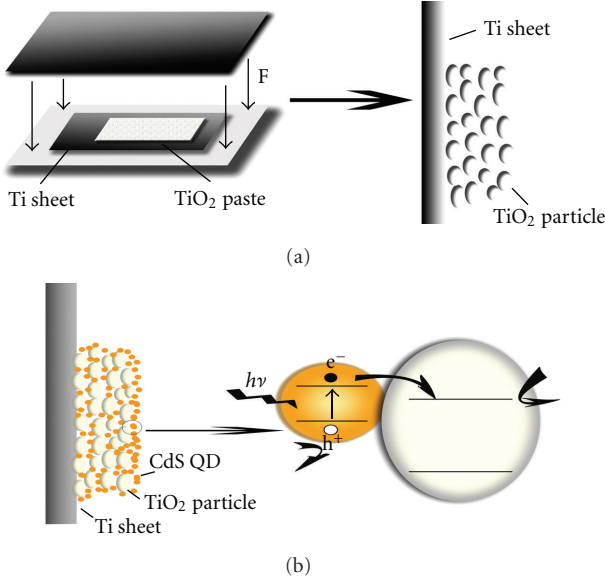


FIGURE 1: The schematic diagram of the process (a) and mechanism (b) of QDs-sensitized solar cell.

3. Results and Discussion

Figure 1 shows the process and mechanism of this QDs-sensitized solar cell. A suitable pressure can make a well packing TiO₂ film; after a series of S-CBD cycles some CdS QDs can formed on the surface of TiO₂ film and in the gaps between TiO₂ particles. When it illuminates under the light, the CdS QDs can absorb the light energy and an electron from the molecular ground state S⁰ is excited to an excited state S*. The excited electron of the CdS QDs is injected into the conduction band of the TiO₂ particles, leaving the QDs molecule to an oxidized state S⁺.

Figure 2 shows UV-vis absorption spectra of a bare TiO₂ film and TiO₂ films sensitized by CdS QDs with different S-CBD times. From Figure 2, we can see with the S-CBD cycles increasing, the UV-vis absorption shoulder and onset position become redshift, which indicating more visible light can be absorbed. By using the empirical equation proposed by Yu et al. [12], it is possible to estimate the sizes of CdS particles from the excitonic peaks of the absorption spectra. The mean diameter of CdS particles (10 S-CBD) was measured to be ca. 4.10 nm on the TiO₂ films, which indicating that the size of the CdS particles on the TiO₂ films is still within the scale of QDs.

To investigate the effect of compress and S-CBD cycles, different cells were made under the same condition. The most variation is the photoanode that we list in Table 1.

Figure 3 shows the photocurrent-voltage (*J-V*) characteristic curves of PEC solar cells as a function of S-CBD cycles. As seen in Figure 3, *J-V* measurements were performed under the conditions of illumination and darkness, respectively. A summary of *J-V* characteristics and the η of cells with different photoanodes are presented in Table 1. Under illumination, it is found that η can be markedly enhanced by the absorption of the CdS QDs. With the

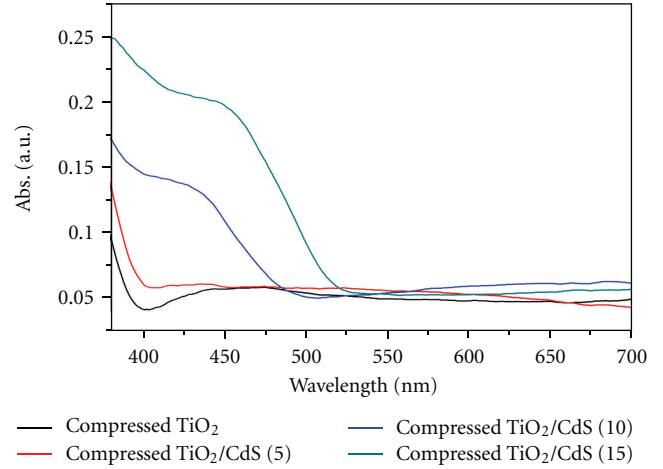


FIGURE 2: UV-vis absorption spectra of a bare TiO₂ film and TiO₂ films sensitized by CdS QDs with different S-CBD times.

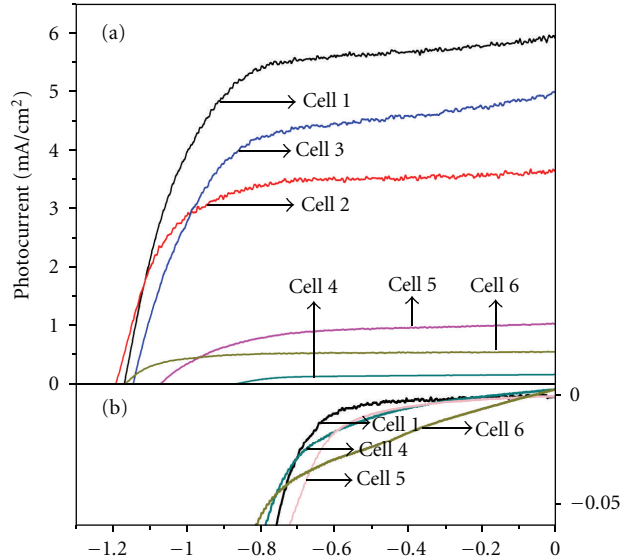


FIGURE 3: Photocurrent versus voltage in 0.1 M Na₂S (a) under AM 1.5 G at 100 mW/cm² illumination (b) in the dark. The TiO₂ film was made by compression method (cell 1 to cell 4), heat after pressure (cell 5), and heat (cell 6). The difference of cell 1 to cell 4 is the S-CBD cycles.

increase of S-CBD cycles to 10, generated photocurrent (J_{sc}) and open-circuit photovoltage (V_{oc}) are both enhanced, reaching their maximum of 5.91 mA/cm² and 1.17 V (versus SCE), respectively. An efficiency of 4.49% is achieved in such a cell. As the S-CBD cycles increases above 10, V_{oc} and J_{sc} both decrease. This trend can be explained as follows: when the amount of the CdS QDs due to the S-CBD cycles is too small, the absorbance of dye is insufficiently, which causes the low J_{sc} . When the amount of the CdS QDs is too large, the transmission process of the electrolyte inside the TiO₂ film's pore is restricted, which causes the serious electron recombination of the cell and also reduces cell performance.

TABLE 1: Parameters obtained from the photocurrent-voltage ($J-V$) measurements of the PEC solar cells constructed using various electrodes.

Cell	Photoanode	J_{sc} (mA/cm ²)	V_{oc} (V versus SCE)	ff	η (%)
Cell 1	Sample 1 (Ti/TiO ₂ (pressure)/S-CBD10)	5.91	1.17	0.65	4.49
Cell 2	Sample 2 (Ti/TiO ₂ (pressure)/S-CBD5)	3.63	1.19	0.68	2.94
Cell 3	Sample 3 (Ti/TiO ₂ (pressure)/S-CBD15)	4.99	1.14	0.60	3.41
Cell 4	Sample 4 (Ti/TiO ₂ (pressure)/S-CBD0)	0.16	0.87	0.61	0.08
Cell 5	Sample 5 (Ti/TiO ₂ (heat after pressure)/S-CBD10)	1.08	1.09	0.58	0.68
Cell 6	Sample 6 (Ti/TiO ₂ (heat)/S-CBD10)	0.55	1.16	0.70	0.44

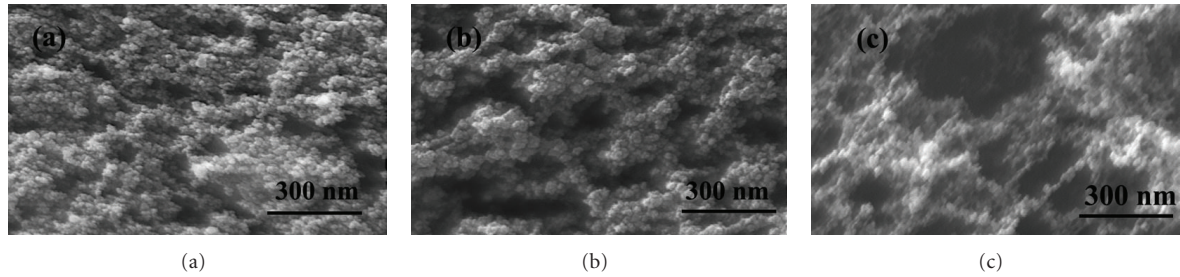


FIGURE 4: SEM of (a) Ti/TiO₂ (compressed), (b) Ti/TiO₂ (heat treatment after compressed), and (c) Ti/TiO₂ (sintered).

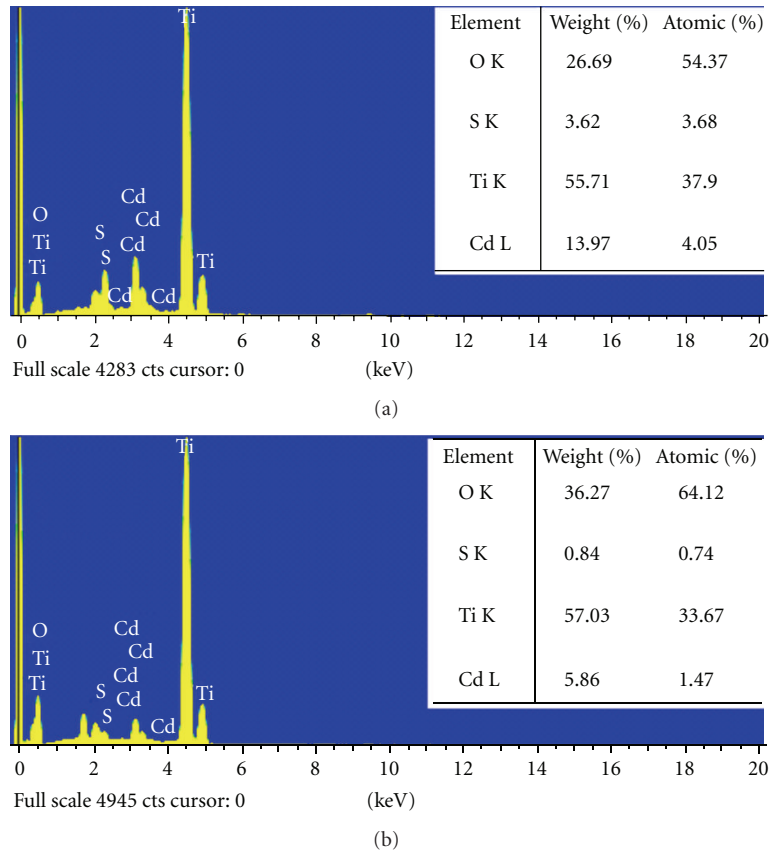


FIGURE 5: EDS of (a) Ti/TiO₂ (compressed)/CdS(S-CBD10) and (b) Ti/TiO₂ (heat treatment after compressed)/CdS(S-CBD10). The inset lists their dates, respectively.

We also took *J-V* curves under the dark condition (Figure 3(b)). Figure 3(b) displays that the onset of the dark current of cell 1 occurs at higher bias than cell 4, which indicates the electron recombination in cell 1 is lower than cell 4.

Table 1 also lists the date of cell 5 and cell 6. The configuration of cell 5 and cell 6 is similar to cell 1; the only difference between them is the fabrication technical of TiO_2 films. The compressed TiO_2 film of cell 5 was posttreated by a heat treatment (450°C , 1.5 h) and the TiO_2 film of cell 6 was made by sintered (450°C , 1.5 h) directly. Surprisingly, both cell 5 and cell 6 show bad results compared with cell 1. Especially, the cell 5 (with J_{sc} of 1.08 mA/cm^2 , V_{oc} of 1.09 V versus SCE, ff of 0.58, and η of 0.68%) performs worse than the cell 1 with respect to all cell parameters, especially in J_{sc} response, the cell 1 is 5.5 times that of the cell 5. It seems the additional heat treatment makes no improvement in cell performance. As mentioned in the introduction, the power conversion efficiency is mainly limited by the small amount of the QDs on the electrode surface when using a sintered TiO_2 film as the photoelectrode. Here, on the basis of the results presented above, we assume that the compression method may help solve this problem. To verify it, we first conducted scanning electron microscopy (SEM) studies of their morphology.

Figure 4 shows plane-view SEM images of a blank TiO_2 film of cell 1 (Figure 4(a)), cell 5 (Figure 4(b)), and cell 6 (Figure 4(c)). All of films display porous structures, creating holes in the film. However, big holes and aggregation between particles can be seen more obviously in Figures 2(b) and 2(c), implying that the surface area per unit volume of the sintered TiO_2 film is smaller than that of unsintered TiO_2 film. This is consistent with Lindström's observation [11]. Kavan et al. [13] find the sintering can cause decrease in surface areas of coated TiO_2 films. They think this decrease is caused by the efficient filling of small pores in the aggregate by surface diffusion. At the same time, we assume that the heat treatment may induce some chemical changes, which may weaken the linkage between the TiO_2 particles and the CdS QDs (further researches are expected to certify it). And both of the phenomena we mentioned above limit the absorption of CdS QDs in cell 5 and cell 6, and thus decrease the J_{sc} . Support for this explanation is given by the EDS (Energy Dispersive X-ray Spectrometer) analysis. Figure 5 is the EDS spectrum of the cell 1 and cell 5, their values are listed inside the Figure 5. Although the EDS value cannot be considered very accurate, it offers us a simple and direct way to study the amount of the CdS QDs. The EDS results reveal the atomic ratio Cd/O of cell 1 and cell 5 is 7.4% and 2.3%, respectively. We can also change them into the volume ratio (CdS over TiO_2) of 22.8% and 7.1%, respectively; the details of the procedure can be found in the literature [5]. So we can find that the amount of CdS QDs of cell 1 is higher than that of cell 5. Noticeably, the above results verify our former explanation. In addition, as seen in Figure 4, the stacking of particles is enhanced by the pressure, which is conducive to the transportation of photogenerated electrons, and can also improve the cell performance.

At last, 4.49% is similar to that of the same structure solar cell (4.15%) [14]. In that literature, they use TiO_2 nanotubes as the photoanode. They think the crystalline nature of the nanotubes and the film geometry allows a fast and efficient transfer of the photogenerated electrons from CdS QDs to the Ti substrate. In our device, we have a large fine TiO_2 film which has a large surface area and the compress also can give a good cohesion between TiO_2 film and Ti sheet which can also improve the transportation of photogenerate electrons. There are also some important factors can affect our final result, as pressure, film's height, and so on. This time we just use a fixed value to assess our devices. And we will make further researches to study it.

In summary, high efficiency has been obtained for QDs-sensitized TiO_2 PEC solar cells prepared by pressing (up to 4.49%). Through the comparison, we conclude that the compression can increase the absorption of CdS QDs and improve the transportation of photogenerate electrons. Overall, the compression method shows promise as a fast, simple, and effective method for the preparation of photoelectrodes in QDs-sensitized solar cells.

Acknowledgment

This work was supported by National Natural Science Foundation of China (no. 21074031).

References

- [1] B. O'Regan and M. Grätzel, "A low-cost, high-efficiency solar cell based on dye-sensitized colloidal TiO_2 films," *Nature*, vol. 353, no. 6346, pp. 737–740, 1991.
- [2] P. V. Kamat, "Quantum dot solar cells. Semiconductor nanocrystals as light harvesters," *Journal of Physical Chemistry C*, vol. 112, no. 48, pp. 18737–18753, 2008.
- [3] F. Gao, Y. Wang, D. Shi et al., "Enhance the optical absorptivity of nanocrystalline TiO_2 film with high molar extinction coefficient ruthenium sensitizers for high performance dye-sensitized solar cells," *Journal of the American Chemical Society*, vol. 130, no. 32, pp. 10720–10728, 2008.
- [4] C. H. Chang and Y. L. Lee, "Chemical bath deposition of CdS quantum dots onto mesoscopic TiO_2 films for application in quantum-dot-sensitized solar cells," *Applied Physics Letters*, vol. 91, no. 5, Article ID 053503, 2007.
- [5] G. Laramona, C. Choné, A. Jacob et al., "Nanostructured photovoltaic cell of the type titanium dioxide, cadmium sulfide thin coating, and copper thiocyanate showing high quantum efficiency," *Chemistry of Materials*, vol. 18, no. 6, pp. 1688–1696, 2006.
- [6] R. Plass, S. Pelet, J. Krueger, M. Grätzel, and U. Bach, "Quantum dot sensitization of organic-inorganic hybrid solar cells," *Journal of Physical Chemistry B*, vol. 106, no. 31, pp. 7578–7580, 2002.
- [7] A. Kongkanand, K. Tvrdy, K. Takechi, M. Kuno, and P. V. Kamat, "Quantum dot solar cells. Tuning photoresponse through size and shape control of $\text{CdSe}-\text{TiO}_2$ architecture," *Journal of the American Chemical Society*, vol. 130, no. 12, pp. 4007–4015, 2008.
- [8] Q. Shen, D. Arae, and T. Toyoda, "Photosensitization of nanostructured TiO_2 with CdSe quantum dots: effects of

- microstructure and electron transport in TiO₂ substrates,” *Journal of Photochemistry and Photobiology A*, vol. 164, no. 1–3, pp. 75–80, 2004.
- [9] H. Lindström, A. Holmberg, E. Magnusson, S. E. Lindquist, L. Malmqvist, and A. Hagfeldt, “A new method for manufacturing nanostructured electrodes on plastic substrates,” *Nano Letters*, vol. 1, no. 2, pp. 97–100, 2001.
- [10] T. Yamaguchi, N. Tobe, D. Matsumoto, and H. Arakawa, “Highly efficient plastic substrate dye-sensitized solar cells using a compression method for preparation of TiO₂ photoelectrodes,” *Chemical Communications*, no. 45, pp. 4767–4769, 2007.
- [11] H. Lindström, A. Holmberg, E. Magnusson, L. Malmqvist, and A. Hagfeldt, “A new method to make dye-sensitized nanocrystalline solar cells at room temperature,” *Journal of Photochemistry and Photobiology A*, vol. 145, no. 1-2, pp. 107–112, 2001.
- [12] W. W. Yu, L. Qu, W. Guo, and X. Peng, “Experimental determination of the extinction coefficient of CdTe, CdSe, and CdS nanocrystals,” *Chemistry of Materials*, vol. 15, no. 14, pp. 2854–2860, 2003.
- [13] L. Kavan, M. Grätzel, J. Rathouský, and A. Zukal, “Nanocrystalline TiO₂ (Anatase) electrodes: surface morphology, adsorption, and electrochemical properties,” *Journal of the Electrochemical Society*, vol. 143, no. 2, pp. 394–400, 1996.
- [14] W. T. Sun, A. Yu, H. Y. Pan, X. F. Gao, Q. Chen, and L. M. Peng, “CdS quantum dots sensitized TiO₂ nanotube-array photoelectrodes,” *Journal of the American Chemical Society*, vol. 130, no. 4, pp. 1124–1125, 2008.

Research Article

Nanoporous ZnO Photoelectrode for Dye-Sensitized Solar Cell

Bayram Kılıç,¹ Emre Gür,² and Sebahattin Tüzemen²

¹Department of Energy System Engineering, Faculty of Engineering, Yalova University, 77100 Yalova, Turkey

²Department of Physics, Science Faculty, Atatürk University, 2510 Erzurum, Turkey

Correspondence should be addressed to Bayram Kılıç, bkilic@yalova.edu.tr

Received 16 January 2012; Revised 7 April 2012; Accepted 9 April 2012

Academic Editor: Mauro Coelho dos Santos

Copyright © 2012 Bayram Kılıç et al. This is an open access article distributed under the Creative Commons Attribution License, which permits unrestricted use, distribution, and reproduction in any medium, provided the original work is properly cited.

Nanoporous and macroporous structures were prepared by using self-assembled monolayer (SAM) onto ZnO thin films in order to investigate the efficiency of dye-sensitized solar cells (DSSCs) produced using these films. Using SAM on ZnO thin films, it is obtained successfully assembled large-area, highly ordered porous ZnO thin films. Varying nanoporous radius is observed between 20 and 50 nm sizes, while it is 500–800 nm for macroporous radius. The solar conversion efficiency of 2.75% and IPCE of 29% was obtained using ZnO nanoporous/N719 dye/I⁻/I₃⁻ electrolyte, while macroporous ZnO given solar conversion efficiency of 2.22% and IPCE of 18%.

1. Introduction

The fundamental properties of II–VI compound semiconductor ZnO have been studied for many years, owing to its direct wide band gap (3.37 eV), large exciton binding energy, huge magnetooptic effect, chemical sensing, piezoelectric and ferroelectric properties, low toxicity, high infrared reflectivity, acoustic characteristics, high electrochemical stability, and excellent electronic properties [1–3]. Moreover, in the past few years, interesting much research has been reported connected with ZnO nanoscale structures with various morphologies such as nanoporous, nanowires, nanorods, and nanotubes obtained by different methods [4, 5]. Among these, porous ZnO nanostructures have some specific advantages such as a high specific surface area, chemical and photochemical stability, uniformity in pore size, shape-selective and rich surface chemistry [6]. According to the variation of porosity, physical and chemical properties of the samples can be controlled and changed. This makes porous structures a promising material in the field of separation, sensors, catalysis, bioscience, surface acoustic wave device, life science, photonic crystals, light emitting diodes, lasers application, and dye-sensitized solar cells (DSSCs) [7]. Since DSSCs based on nanostructure materials offer very low cost and relatively efficient photovoltaic energy conversion, it has attracted much attention in the last decade [8–12]. The highest efficiency, to the best of our knowledge, reported

on DSSCs was 11% obtained on nanoporous TiO₂ by using ruthenium complex dye, containing I⁻/I₃⁻ redox couple electrolytes, and platinum counterelectrode [13–15]. On the other hand, it has been achieved 0.3–6% conversion efficiency in ZnO nanosemiconductor materials [16, 17]. It is still thought of as an alternative to TiO₂ because of its ease of crystallization and optical and structural quality.

Reports are available in the preparation of porous ZnO films by a variety of techniques including wet-chemical method, radio frequency magnetron sputtering deposition, electrochemical anodisation, etching surface by an organic and inorganic solvents, templating methods, and self-assembled monolayers (SAMs) which are ordered molecular assemblies of single layer formed via the adsorption of an active surfactant onto the surfaces [18–22]. One of the most common examples to the SAMs is alkene thiols such as hexanethiols and dodecanethiols. The SAMs of thiols have been studied widely in recent years, since they offer a rational and easy approach for fabricating interfaces with a well-designed composition, structural properties and thickness of the samples [23–25].

In this study, macro- and nanoporous ZnO structures were formed by using SAMs and DSSC performance is compared to each other in terms of efficiency. Detailed structural and optical characterizations were performed by using scanning electron microscopy (SEM), X-ray diffraction

(XRD), photoluminescence (PL), absorbance, and Raman spectroscopy.

2. Experimental

The ECD of ZnO thin films were performed on indium tin oxide (ITO) substrate in a solution of 0.05 M $\text{Zn}(\text{ClO}_4)_2$ and 0.1 M LiClO_4 into DMSO solvent. ITO substrates were cleaned in an ultrasonic bath with trichloroethylene, acetone, and methanol. A conventional three-electrode ECD system was used for deposition of ZnO thin films. ITO substrate is used as the working electrode, Ag/AgCl as the reference electrode, and zinc plate as counter electrode. The growth temperature and deposition time were arranged at 100°C and 1 h, respectively. Deposition potential was kept constant during the growth process as -1.1 V which is determined from cyclic voltammogram (figure not shown). In order to obtain porous ZnO thin films, 0.05 M C_{12}SH -SAM and 0.05 M C_6SH -SAM were used with ethanol solution. After the growth of ZnO thin films, thin films were immersed in these solutions.

ZnO nano- and macroporous structure-based DSSCs were prepared by adsorbing cis-bis(isothiocyanato) bis(2,20-bipyridyl-4,40-dicarboxylato)-ruthenium (II) bis tetra butylammonium (N719) dye onto the surfaces of both kinds of samples. Substrates were first heated to 100°C before immersing them into 0.5 mM ethanolic dye solution for 30 min. The counterelectrode was an Pt:F:SnO₂ substrate. The electrodes were separated by 20 mm polypropylene spacer and pressed together with binder clips. Electrolyte was introduced between the electrodes by capillary forces. The electrolyte consisted of 0.5 M tetrabutylammonium iodide, 0.05 M I_2 (Iodine), and 0.5 M 4-tertbutylpyridine in acetonitrile. Active electrode area was typically 0.25 cm².

The morphology of the nanostructures was analyzed using a JEOL-6400 SEM. The crystal structure was analyzed by XRD (Rigaku D/Max-IIIC diffractometer) with $\text{Cu-K}\alpha$ radiation of 1.54 Å, within the 2θ angle ranging from 20 to 80. The PL measurements were conducted with the RF 5301 PC Shimadzu spectrofluorometer at room temperature. The absorption and transmittance measurements were carried out by Perkin-Elmer UV-VIS Lambda 2S spectrometer. The Raman scattering measurements were performed using a micro-Raman Renishaw 2000 system with an excitation source of 514.5 nm at room temperature. Current-voltage (I - V) characteristics were recorded using a Keithley 175A digital multimeter using 0.01 V/s voltage ramp rate. The light source was a 250 W tungsten halogen lamp calibrated to 100 mW/cm² using a radiometer (IL1700, International). The absorbance and incident photon to current conversion efficiency (IPCE) were measured using a 1000 W Xe lamp and a monochromator.

3. Results and Discussion

3.1. Formation Mechanism of the Porous ZnO Structures by SAMs of C_6SH and C_{12}SH .

SAMs are formed by immersing an appropriate substrate into a solution of an organic

compound (surface-active material), possessing the ability to spontaneously form an ordered molecular layer on the substrate [26]. The driving force for the spontaneous formation of the two-dimensional assembly includes chemical bond formation of molecules with the surface and intermolecular interactions [27]. In this study, formation of different size of porous structures on ZnO semiconductors by SAMs of C_6SH and C_{12}SH was achieved. In detail, the constituting self-assembling of the C_6SH and C_{12}SH consists of three parts. The first part is the head group. It causes the exothermic process of chemisorption on the surface of the substrate. It has specific affinity for the substrate. Organization of C_6SH and C_{12}SH starts with the interaction between the head and the substrate by means of chemisorption and last to the thermodynamic equilibrium. The second part is the alkyl chain. It is responsible for the intermolecular distance, the molecular orientation, and the degree of order in the film. The third part is a functional group that constitutes the outer surface of the film. The principal driving force for the formation of these films is a specific interaction between the head group and the substrate surface [28]. Provided these interactions are strong, SAMs of C_6SH and C_{12}SH form stable films depending on waiting time into the C_6SH and C_{12}SH solution. Porous structures develop on ZnO due to solvent evaporation at room temperature. Ma and Hao indicated macroporous structures on gold using C_{12}SH solution due to solvent evaporation and water droplet condensation [29]. They showed that the rapid evaporation of the solvent decreases the air/liquid interfacial temperature, resulting in porous formation on substrate. Similarly, Cai et al. showed porous formation via SAMs and indicated that different solvent evaporation rates affect pore formation and pore size [30].

The structural properties of the porous ZnO, which is obtained via SAMs of C_6SH and C_{12}SH , are strongly influenced by the interactions between the functional groups comprising the alkyl chain and functional group of the molecules as it has been shown our previous study [25]. The porous formation is largely governed by molecular-substrate interactions, though lateral chain-chain interactions are also quite important. While porous formation on ZnO substrate occurs via SAMs of C_6SH and C_{12}SH , it was shown that films formed by short alkyl chains exhibit very different characteristics than those formed by long alkyl chains. The alkyl chain and functional groups are found to have a profound influence on the porous structure. This knowledge will undoubtedly prove useful in controlling the surface densities of the samples which are prepared via SAMs.

3.2. Structural and Optical Properties of the Porous ZnO.

X-ray diffraction measurement of nano- and macroporous ZnO has been shown that the films have highly preferred (0002) *c*-axis orientation as shown in Figures 1(a) and 1(b), respectively. Another peak, ZnO (0004), can be seen in the Figure 1(a). The peak intensity of (0002) orientation of macroporous ZnO has shown the decrease by half that of the nanoporous sample. This might indicate that the bigger size

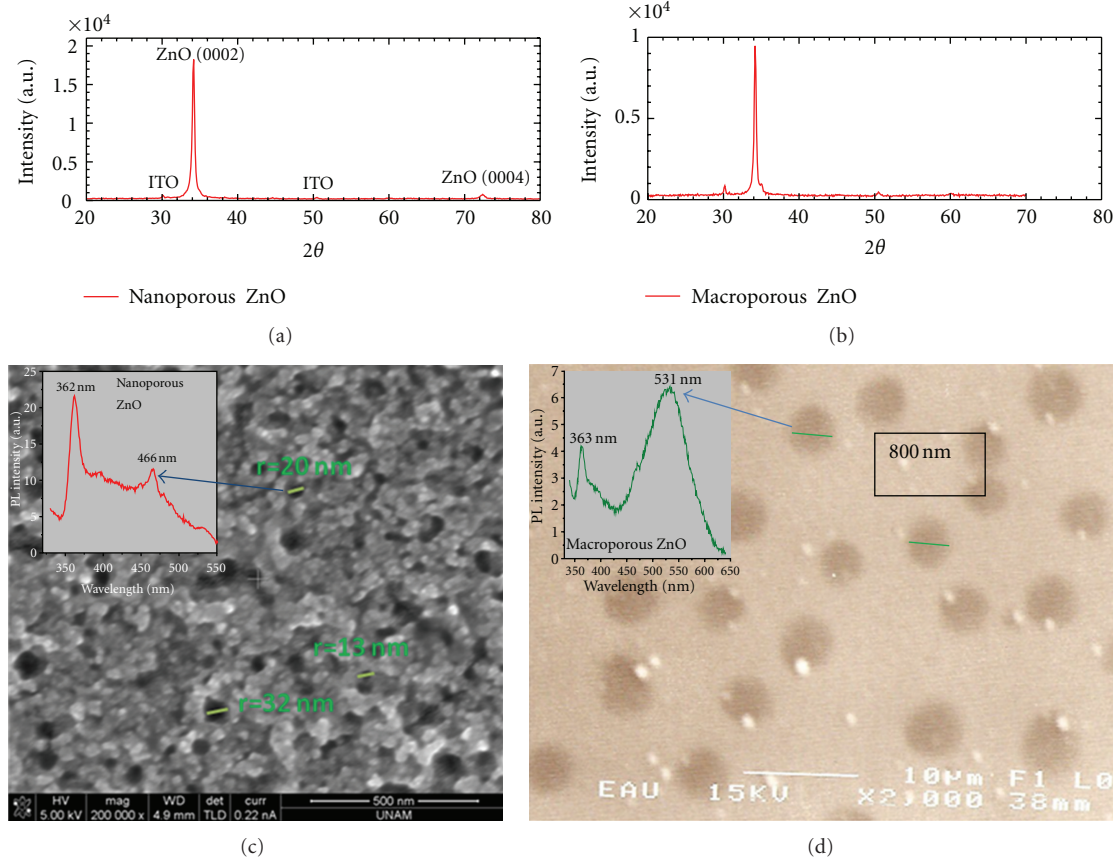


FIGURE 1: (a) XRD plot of nanoporous ZnO, (b) XRD plot of macroporous ZnO, (c) SEM image and PL characterization of nanoporous ZnO, (d) SEM image and PL characterization of macroporous ZnO.

porous radius has a negative effect on the crystallization as expected.

Figures 1(c) and 1(d) show SEM images of the porous structures formed onto the ZnO thin films which were obtained by using SAMs technique. Figure 1(c) shows that the nanoporous ZnO thin films have successfully been obtained with porous radius around 50 nm as indicated on image and also uniform pore distribution can be seen through the surface. Average radius of the pores has been calculated by taking account of the pores having a maximum, minimum and average size as indicated in the Figure 1(c). Macroporous structures are shown in Figure 1(b). Perfect circular structures of the pores can be seen with an average pore radius of around $\sim 800 \text{ nm}$ as it is indicated in the figure.

PL characterizations of the nano- and macroporous ZnO thin films are shown as an inset of the respective SEM images in Figures 1(c) and 1(d). PL measurements exhibit different spectra for both samples. Two luminescence bands are observed in nanoporous ZnO thin films. One of them is relatively weak deep level emission peaking at the 466 nm, while narrow UV emission is dominant emission peaking at about 362 nm which might be responsible for the recombination of the free excitons. As can be seen in the Figure 1(d), macroporous structure has a strong green emission peak located at $\sim 530 \text{ nm}$. This peak intensity is

much higher compared to the intensity of the UV emission at $\sim 363 \text{ nm}$ confirming that the decrease in the optical quality of the film [23–25]. Also, it can be speculated that the deep level defect formation causing the green emission in ZnO, which is believed commonly either oxygen vacancy or zinc vacancy [3], is more favorable in macroporous sample than the nanoporous sample.

The UV-visible absorbance and transmittance spectra of the ZnO nanoporous and macroporous are shown in Figures 2(a) and 2(b), respectively. The absorption spectra of the ZnO porous structures showed a strong absorption between 300 nm and 360 nm. The ZnO nanoporous sample has a good transparency with a visible light transmittance higher than 85%. However, the ZnO macroporous structures exhibited low transmittance at around 60%, which might be related to the pore density. These results clearly indicate that transparency of the ZnO nanoporous structure are related to surface morphology and roughness which affects the light scattering. Optical band gap of the ZnO nanoporous structures is calculated by using the following equation [30, 31]:

$$(\alpha) \propto (h\nu - E_g)^{1/2}, \quad (1)$$

where α is absorption coefficient. The direct band gap E_g was determined from α^2 -photon energy plot as shown in

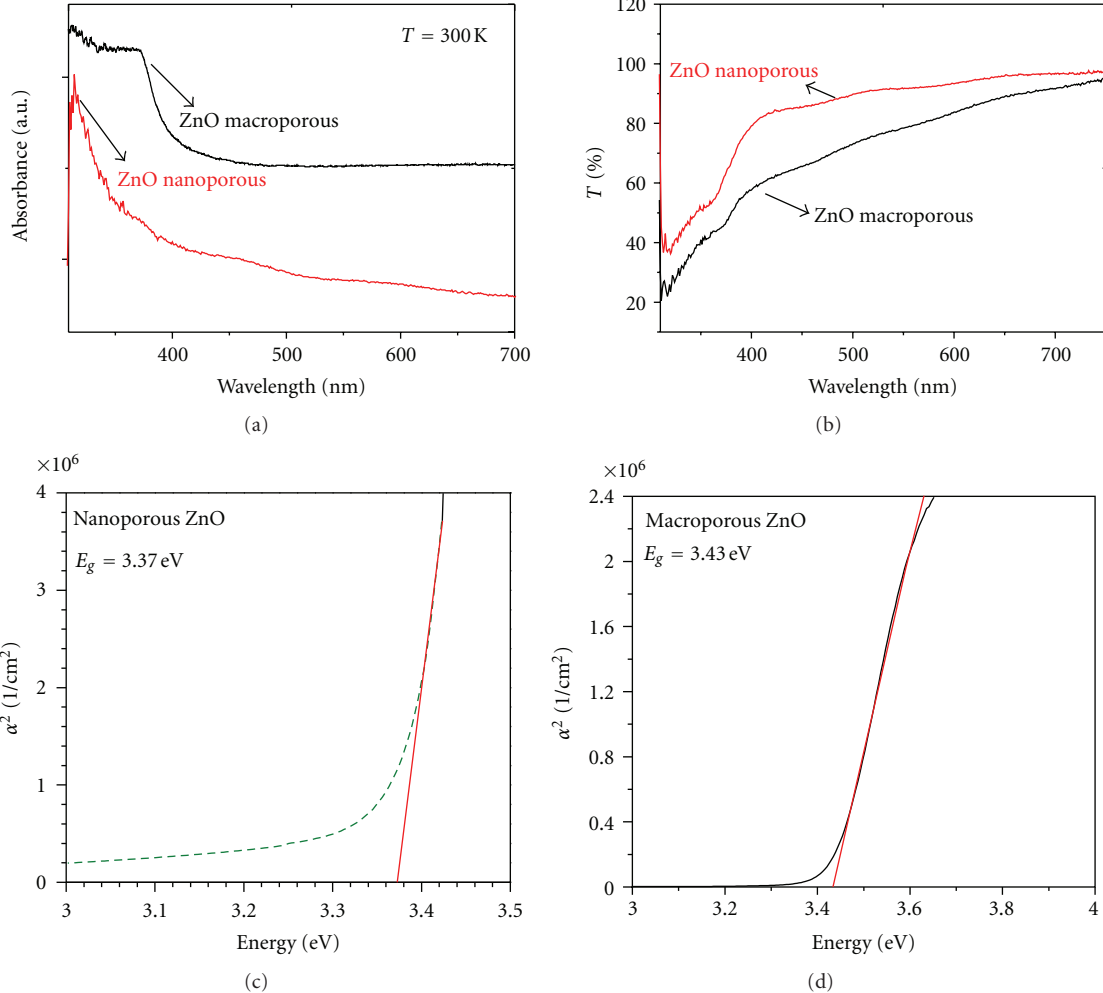


FIGURE 2: (a) Absorbance. (b) Transmittance spectrum of ZnO nanoporous and macroporous structures at room temperature. (c) Absorption coefficient and energy plot for ZnO nanoporous. (d) Absorption coefficient and energy plot for ZnO macroporous.

Figure 2(c) and 2(d). The optical bandgaps were determined as 3.37 eV and 3.42 eV for ZnO nanoporous and macroporous, respectively. Different optical band gap values obtained have shown that optical properties of the ZnO structures can be changed by the change in pore radius formed on the surfaces.

Raman spectra for the nanostructures were obtained to investigate the vibration properties of the nano and macroporous ZnO films. Wurtzite ZnO nanostructures belong to the C_6v^4 ($P6_3mc$) symmetry group [32]. At the Γ point of the Brillouin zone, group theory predicts the existence of the following optic modes [33]:

$$\Gamma_{\text{opt}} = A_1 + 2B_1 + E_1 + 2E_2. \quad (2)$$

A_1 , E_1 , and E_2 modes are Raman active, and B_1 is forbidden. In addition, A_1 , E_1 are infrared active and split into longitudinal (LO) and transverse (TO) optical components. The Raman spectra for the nanostructures in Figure 3 show that the ZnO nanoporous and macroporous structures have the similar Raman shift at the range of 100–900 cm^{-1} .

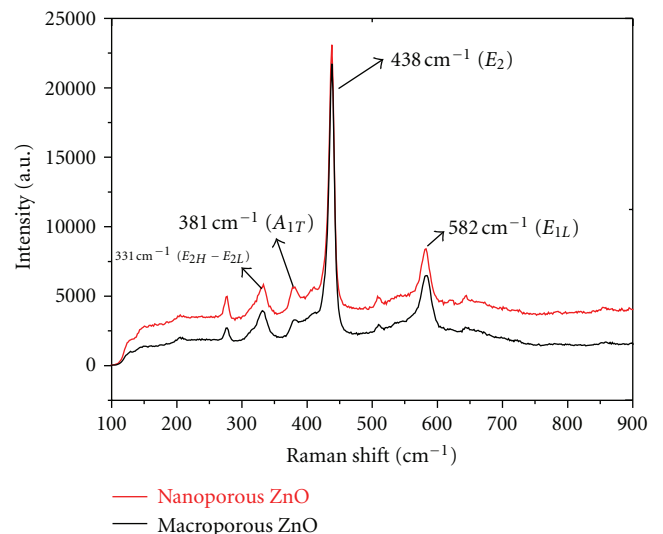


FIGURE 3: Raman shift of nano- and macroporous ZnO.

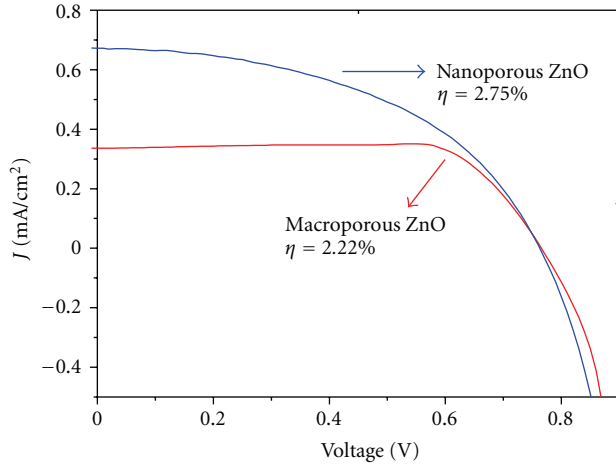


FIGURE 4: Current density-voltage characterization of nano- and macroporous ZnO.

A dominant and strong intensity peak at 438 cm^{-1} indicates the spectrum known as the optical phonon E_2 . The E_2 mode corresponds to the band characteristic for the Wurtzite hexagonal phase of ZnO raman active branches, which is also one of the characteristics of ZnO nanostructures [34]. However, two short peaks at 331 and 380 cm^{-1} were shown to be as E_{2H} - E_{2L} (multiphonon) and A_{1T} modes, respectively. For the ZnO nanostructures, an extra Raman band at 582 cm^{-1} known to be related to the E_1 mode because of the oxygen deficiency [35] indicates the presence of oxygen vacancies in the ZnO nanostructures.

Figure 4 shows the comparison of the current density-voltage ($J-V$) characteristics of solar cells fabricated using the ZnO nano- and macroporous structures, under 100 mW/cm^2 of AM-1.5 illumination. It can be seen from Figure 4 that there is a considerable increase in the short-circuit current density (J_{sc}) of the nanoporous ZnO DSSCs in comparison with the macroporous ZnO DSSCs. ZnO nanoporous structures provide both a larger surface area and a direct pathway for electron transport along the pore resulting in the observed higher J_{sc} [36, 37]. This is attributed to the superior light absorbing characteristics provided by the larger surface areas formed by the nanoporous structure.

The open-circuit voltage (V_{oc}) of the DSSCs shows that the higher solar conversion efficiency (η) of 2.75% is reached for the nanoporous structures, while it is 2.22% for macroporous structure. A comparison of the different solar cell parameters for the both DSSCs is summarized in Table 1. It can be seen that the ZnO nanoporous structures shows η values that are almost 40% higher than that of the macroporous ZnO. This is a significant result showing the dependence of solar cell performance on surface morphology of the ZnO. Obtained larger surface area in nanoporous structure also results in improved dye adsorption [38–40]. Figure 5 displays the dependence of IPCE of the DSSCs on the different ZnO nanostructures. As expected, the ZnO

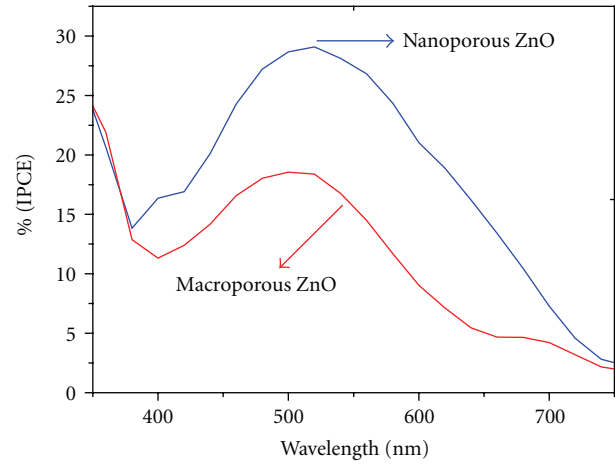


FIGURE 5: IPCE (%) measurements of nano- and macroporous ZnO.

nanoporous DSSCs show much higher IPCE, 29% at about 510 nm , compared to the macroporous ZnO, 18% at about 520 nm , mainly due to the aforementioned effect of larger surface area (and dye-loading).

Several attempts have been made to use ZnO photoelectrode in DSSCs. Redmond et al. [41] achieved an IPCE of 13% at 520 nm when using the $\text{Ru}(\text{dcbpyH}_2)_2(\text{NCS})_2$ dye. On the other hand, Keis et al. introduced IPCE values of 50–60% at 540 nm in photoelectrochemical (PEC) and an overall solar energy conversion efficiency of 2.0% was obtained under 56 mW/cm^2 illumination with a solar simulator [42, 43] which is lower than the present study. Recently, solar energy conversion efficiency under 99 mW/cm^2 illumination reaching 2.5% has been reported for then mercurochrome-sensitized ZnO PEC solar cell [44]. However, the efficiency is still moderate compared to solar cells based on TiO_2 .

4. Conclusion

In this study, using SAMs technique on ZnO thin films, we have successfully formed an assembled large-area, highly ordered porous ZnO thin films. Average pore radius is obtained around 50 nm , and 800 nm for nanoporous and macroporous ZnO structures, respectively. PL measurements show highly different emission characteristics according to the size of the porous radius: the samples having a macroporous show that green emission is the dominant, while, in the nanoporous sample the UV emission is dominant showing to better optical quality of the sample. In addition, the origin of an extra Raman band at 582 cm^{-1} was obtained due to oxygen deficiency of the ZnO nanostructures. The solar-to-electric energy conversion efficiency of 2.75% and IPCE of 29% was obtained by using the ZnO nanoporous/N719 dye/ I^-/I_3^- electrolyte. In addition, Zn macroporous showed solar-to-electric energy conversion efficiency of 2.22% and IPCE of 18%. In conclusion, ZnO nanoporous electrodes have been studied into dye-sensitized solar cells where they

TABLE 1: *J-V* characteristics of the cell using ZnO nanostructures with N719.

Morphology	FF	Efficiency	<i>V_{oc}</i>	<i>I_{sc}</i>	<i>P_{max}</i>	<i>V_{mp}</i>	<i>I_{mp}</i>	Area (cm ²)
Nanoporous ZnO	0.494	2.750	0.745	0.672	0.247	0.520	0.476	0.25
Macroporous ZnO	0.796	2.222	0.748	0.336	0.200	0.580	0.345	0.25

display reasonable light-harvesting efficiency, photovoltage, and relatively good fill factors than macroporous sample in the present study.

Acknowledgment

The authors gratefully acknowledge The Scientific and Technological Research Council of Turkey (TUBITAK) for the Grant 2214-P.h.D research scholarship program.

References

- [1] S. H. Lee, H. J. Lee, H. Goto, and M. Cho, "Fabrication of porous ZnO nanostructures and morphology control," *Physica Status Solidi*, vol. 4, no. 5, pp. 1747–1750, 2007.
- [2] G. Westin, A. Pohl, M. Ottosson, and K. Jansson, "Direct processing of porous nano-structured ZnO-CoOx films," *Thin Solid Films*, vol. 515, no. 20-21, pp. 7751–7757, 2007.
- [3] S. Tüzemen and E. Gür, "Principal issues in producing new ultraviolet light emitters based on transparent semiconductor zinc oxide," *Optical Materials*, vol. 30, no. 2, pp. 292–310, 2007.
- [4] J. Wang, S. X. Zhang, J. You et al., "ZnO nanostructured microspheres and grown structures by thermal," *Bulletin of Material Science*, vol. 31, no. 4, pp. 597–601, 2008.
- [5] J. Shen, H. Zhuang, D. Wang, C. Xue, and H. Liu, "Growth and characterization of zno nanoporous belts," *Crystal Growth and Design*, vol. 9, no. 5, pp. 2187–2190, 2009.
- [6] G. Q. Lu and X. S. Zhao, *Nanoporous Materials: Science and Engineering*, Chemical Engineering 4, Imperial College Press, 2004.
- [7] Z. Liu, Z. Jin, J. Qiu, X. Liu, W. Wu, and W. Li, "Preparation and characteristics of ordered porous ZnO films by a electrodeposition method using PS array templates," *Semiconductor Science and Technology*, vol. 21, no. 1, article 60, 2006.
- [8] J. C. Love, L. A. Estroff, J. K. Kriebel, R. G. Nuzzo, and G. M. Whitesides, "Self-assembled monolayers of thiolates on metals as a form of nanotechnology," *Chemical Reviews*, vol. 105, no. 4, pp. 1103–1169, 2005.
- [9] B. O'Regan and M. Grätzel, "A low-cost, high-efficiency solar cell based on dye-sensitized colloidal TiO₂ films," *Nature*, vol. 353, no. 6346, pp. 737–740, 1991.
- [10] A. Hagfeldt and M. Grätzel, "Light-Induced redox reactions in nanocrystalline systems," *Chemical Reviews*, vol. 95, pp. 49–68, 1995.
- [11] T. Soga, *Nanostructure Materials for Solar Energy Conversion*, Elsevier, Nagoya, Japan, 2006.
- [12] M. Grätzel, "Solar energy conversion by dye-sensitized photovoltaic cells," *Inorganic Chemistry*, vol. 44, no. 20, pp. 6841–6851, 2005.
- [13] M. Grätzel, "Perspectives for dye-sensitized nanocrystalline solar cells," *Progress in Photovoltaics*, vol. 8, pp. 171–185, 2000.
- [14] J. B. Baxter and E. S. Aydil, "Dye sensitized solar cells based on semiconductor morphologies with ZnO nanowires," *Solar Energy Materials & Solar Cells*, vol. 90, pp. 607–622, 2006.
- [15] M. Dürr, A. Bamedi, A. Yasuda, and G. Nelles, "Tandem dye-sensitized solar cell for improved power conversion efficiencies," *Applied Physics Letters*, vol. 84, no. 17, pp. 3397–3399, 2004.
- [16] M.K. Nazeruddin, A. Kay, I. Rodicio et al., "Conversion of light to electricity by cis-X2bis(2,2'-bipyridyl)-4,4'-dicarboxylaterutheniumII charge-transfer sensitizers X = Cl-, Br-, I-, CN-, and SCN- on nanocrystalline titanium dioxide electrodes," *Journal of the American Chemical Society*, vol. 115, no. 14, pp. 6382–6390, 1993.
- [17] Q. Zhang, C. S. Dandeneau, X. Zhou, and C. Cao, "ZnO nanostructures for dye-sensitized solar cells," *Advanced Materials*, vol. 21, no. 41, pp. 4087–4108, 2009.
- [18] C. Bouvy and B. L. Su, "ZnO@porous media, their PL and laser effect," *Journal of Materials Science & Technology*, vol. 24, no. 4, pp. 495–511, 2008.
- [19] H. Yan, C. F. Blanford, B. T. Holland, W. H. Smyrl, and A. Stein, "General synthesis of periodic macroporous solids by templated salt precipitation and chemical conversion," *Chemistry of Materials*, vol. 12, no. 4, pp. 1134–1141, 2000.
- [20] B. Reeja-Jayan, E. De La Rosa, S. Sepulveda-Guzman, R. A. Rodriguez, and M. J. Yacaman, "Structural characterization and luminescence of porous single crystalline ZnO nanodisks with sponge-like morphology," *Journal of Physical Chemistry C*, vol. 112, no. 1, pp. 240–246, 2008.
- [21] J. C. Love, L. A. Estroff, J. K. Kriebel, R. G. Nuzzo, and G. M. Whitesides, "Self-assembled monolayers of thiolates on metals as a form of nanotechnology," *Chemical Reviews*, vol. 105, pp. 1103–1169, 2005.
- [22] A. Ulman, "Formation and structure of self-assembled monolayers," *Chemical Reviews*, vol. 96, no. 4, pp. 1533–1554, 1996.
- [23] J. B. Lee, M. Namgung, S. B. Lee, and S. Y. Oh, "Fabrication of an electrically conductive mixed self-assembled monolayer and its application in an electrochemical immunosensor," *Cond Matt*, vol. 10628, p. 1352, 2008.
- [24] C. L. Perkins, "Molecular anchors for self-assembled monolayers on ZnO: a direct comparison of the thiol and phosphoric acid moieties," *Journal of Physical Chemistry C*, vol. 113, no. 42, pp. 18276–18286, 2009.
- [25] E. Gür, B. Kılıç, C. Coşkun, S. Tüzemen, and F. Bayrakçeken, "Nanoporous structures on ZnO thin films," *Superlattices and Microstructures*, vol. 47, no. 1, pp. 182–186, 2010.
- [26] M. P. Pilani, "Self-assembly of inorganic nanocrystals: fabrication and collective intrinsic properties," *Accounts of Chemical Research*, vol. 40, pp. 685–693, 2007.
- [27] H. Graaf, C. Maedler, M. Kehr, and T. Oekermann, "Structural changes of electrodeposited ZnO matrices for dye-sensitized solar cells during preparation," *Journal of Physical Chemistry C*, vol. 113, no. 17, pp. 6910–6912, 2009.
- [28] J. Joo, D. Lee, M. Yoo, and S. Jeon, "ZnO nanorod-coated quartz crystals as self-cleaning thiol sensors for natural gas fuel cells," *Sensors and Actuators, B: Chemical*, vol. 138, no. 2, pp. 485–490, 2009.
- [29] H. Ma and J. Hao, "Evaporation-induced ordered Honeycomb structures of gold nanoparticles at the air/water interface," *Chemistry*, vol. 10, p. 1002, 2009.

- [30] X. M. Cai, K. W. Cheng, C. C. Oey et al., "Porous metallic films fabricated by self-assembly of gold nanoparticles," *Thin Solid Films*, vol. 491, no. 1-2, pp. 66–70, 2005.
- [31] S. Tüzemen, E. Gür, T. Yıldırım, G. Xiong, and R. T. Williams, "An investigation of control mechanisms of the excitonic behavior in reactively sputtered ZnO on (0001) Al₂O₃," *Journal of Applied Physics*, vol. 100, no. 10, Article ID 103513, 7 pages, 2006.
- [32] Y. Tong, Y. Liu, C. Shao et al., "Growth and optical properties of faceted hexagonal ZnO nanotubes," *Journal of Physical Chemistry B*, vol. 110, no. 30, pp. 14714–14718, 2006.
- [33] F. Decremps, J. Pellicer-Porres, A. M. Saitta, J. C. Chervin, and A. Polian, "High-pressure Raman spectroscopy study of wurtzite ZnO," *Physical Review B*, vol. 65, no. 9, Article ID 092101, 4 pages, 2002.
- [34] A. Umar, S. H. Kim, Y. S. Lee, K. S. Nahm, and Y. B. Hahn, "Catalyst-free large-quantity synthesis of ZnO nanorods by a vapor-solid growth mechanism: Structural and optical properties," *Journal of Crystal Growth*, vol. 282, no. 1-2, pp. 131–136, 2005.
- [35] J.-J. Wu and S.-C. Liu, "Catalyst-free growth and characterization of ZnO nanorods," *Journal of Physical Chemistry B*, vol. 106, no. 37, pp. 9546–9551, 2002.
- [36] A. Suliman, Y. Tang, and L. Xu, "Preparation of ZnO nanoparticles and nanosheets and their application to dye-sensitized solar cells," *Solar Energy Materials & Solar Cells*, vol. 91, no. 18, pp. 1658–1662, 2007.
- [37] J. B. Baxter and E. S. Aydil, "Nanowire-based dye-sensitized solar cells," *Applied Physics Letters*, vol. 86, no. 5, Article ID 053114, 3 pages, 2005.
- [38] Y. F. Hsu, Y. Y. Xi, A. Djurisic, and W. K. Chen, "ZnO nanorods for solar cells: hydrothermal growth versus vapor deposition," *Applied Physics Letters*, vol. 92, no. 13, Article ID 133507, 3 pages, 2008.
- [39] A. J. Cheng, Y. Tzeng, Y. Zhou et al., "Thermal chemical vapor deposition growth of zinc oxide nanostructures for dye-sensitized solar cell fabrication," *Applied Physics Letters*, vol. 92, no. 9, Article ID 092113, 3 pages, 2008.
- [40] M. Law, L. E. Greene, J. C. Johnson, R. Saykally, and P. Yang, "Nanowire dye-sensitized solar cells," *Nature Materials*, vol. 4, no. 6, pp. 455–459, 2005.
- [41] G. Redmond, D. Fitzmaurize, and M. Grätzel, "Visible Light Sensitization by *cis*-Bis(thiocyanato)bis(2,2'-bipyridyl-4,4'-dicarboxylato)ruthenium(II) of a Transparent Nanocrystalline ZnO Film Prepared by Sol-Gel Techniques," *Chemistry of Materials*, vol. 6, no. 5, pp. 686–691, 1994.
- [42] K. Keis, C. Bauer, G. Boschloo et al., "Nanostructured ZnO electrodes for dye-sensitized solar cell applications," *Journal of Photochemistry and Photobiology A*, vol. 148, no. 1–3, pp. 57–64, 2002.
- [43] H. Rensmo, K. Keis, H. Lindström et al., "High light-to-energy conversion efficiencies for solar cells based on nanostructured ZnO electrodes," *Journal of Physical Chemistry B*, vol. 101, no. 14, pp. 2598–2601, 1997.
- [44] K. Hara, T. Horiguchi, T. Kinoshita, K. Sayama, H. Sugihara, and H. Arakawa, "Highly efficient photon-to-electron conversion with mercurochrome-sensitized nanoporous oxide semiconductor solar cells," *Solar Energy Materials and Solar Cells*, vol. 64, no. 2, pp. 115–134, 2000.

Research Article

PtRu/C Electrocatalysts Prepared Using Gamma and Electron Beam Irradiation for Methanol Electrooxidation

**Dionisio F. Silva, Adriana N. Geraldes, Eddy S. Pino,
Almir Oliveira Neto, Marcelo Linardi, and Estevam V. Spinacé**

Instituto de Pesquisas Energéticas e Nucleares, IPEN/CNEN, Cidade Universitária, Avenue Professor Lineu Prestes, 2242, 05508-000 São Paulo, SP, Brazil

Correspondence should be addressed to Estevam V. Spinacé, espinace@ipen.br

Received 18 October 2011; Revised 1 February 2012; Accepted 7 February 2012

Academic Editor: Mauro Coelho dos Santos

Copyright © 2012 Dionisio F. Silva et al. This is an open access article distributed under the Creative Commons Attribution License, which permits unrestricted use, distribution, and reproduction in any medium, provided the original work is properly cited.

PtRu/C electrocatalysts (carbon-supported PtRu nanoparticles) were prepared in a single step submitting water/2-propanol mixtures containing Pt(IV) and Ru(III) ions and the carbon support to gamma and electron beam irradiation. The electrocatalysts were characterized by energy dispersive X-ray analysis (EDX), X-ray diffraction (XRD), transmission electron microscopy (TEM), and cyclic voltammetry and tested for methanol electrooxidation. PtRu/C electrocatalyst can be prepared in few minutes using high dose rate electron beam irradiation while using low dose rate gamma irradiation some hours were necessary to prepare it. The obtained materials showed the face-centered cubic (fcc) structure of Pt and Pt alloys with average nanoparticle sizes of around 3 nm. The material prepared using electron beam irradiation was more active for methanol electrooxidation than the material prepared using gamma irradiation.

1. Introduction

Fuel cells convert chemical energy directly into electrical energy with high efficiency. However, the use of hydrogen as a fuel presents problems, principally with storage for mobile and portable applications [1–3]. Thus, there has been an increasing interest in the use of alcohols directly as fuel (Direct Alcohol Fuel Cell—DAFC). Methanol has been considered the most promising alcohol and carbon-supported PtRu nanoparticles (PtRu/C), normally with a Pt : Ru atomic ratio of 50 : 50, the best electrocatalyst [4]. However, the catalytic activity of PtRu/C electrocatalysts strongly depends on the method of preparation and it is one of the major topics studied in direct methanol fuel cells (DMFC) [4, 5]. PtRu/C electrocatalysts are produced mainly by impregnation and colloids methods. Although impregnation method is a simple procedure, the major drawback is the difficulty in controlling nanoparticle size and distribution. The colloidal methods have the advantage to produce very small and homogeneously distributed carbon-supported metal nanoparticles; however, the methodologies are very complex [4].

Lately radiation-induced reduction of metal ion precursors in solution has been described to prepare carbon-supported metal nanoparticles for fuel cell applications. Despite the complexity and cost of electron beam or gamma irradiation facilities, the methodologies used to prepare the electrocatalysts are easy to perform [6–10]. Le Gratiet et al. [6] prepared platinum nanoparticles submitting a K_2PtCl_4 salt dissolved in a CO-saturated water/2-propanol solvent to gamma irradiation. The reduction of platinum ions occurred by a combined effect of CO and radicals produced by radiolysis, leading to the formation of platinum nanoparticles of 2–3 nm diameter that were further impregnated on the carbon support. These catalysts were found to be effective for methanol or hydrogen electrooxidation. Oh et al. [7] prepared Pt-Ru alloy particles dispersed on various carbon structures in water/2-propanol using gamma irradiation, but no tests for DMFC were described using the obtained materials. Wang et al. [8] prepared Pt nanoparticles irradiating an aqueous solution of chloroplatinic acid in the presence of 2-propanol as a radical scavenger and sodium sulfonate as

a surfactant. The synthesized Pt nanoparticles (2.5–4.0 nm) were further impregnated on multiwalled carbon nanotubes. The obtained material was tested on a single proton exchange membrane fuel cell operating with H₂/O₂, and the results showed that the electrocatalysts were very promising. Silva et al. [9] prepared PtRu/C electrocatalysts in a single step submitting water/ethylene glycol solutions containing Pt(IV) and Ru(III) ions and the carbon support to gamma irradiation at room temperature under stirring. The obtained carbon-supported PtRu nanoparticles showed mean particle sizes of 2.5–3.0 nm and were very active for methanol oxidation. Recently, Chai et al. [10] prepared Pt (80 wt%) supported on a mesoporous carbon support in a single step. The Pt salt was dissolved in a solution of water/2-propanol, and the carbon support was added to the solution. The mixture was irradiated at room temperature under stirring. The obtained material exhibited enhanced catalytic activity towards the oxygen reduction reaction (ORR). In this work, PtRu/C electrocatalysts were prepared using high dose rate electron beam and low dose rate gamma irradiation and were tested for methanol electrooxidation.

2. Experimental

PtRu/C electrocatalyst (20 wt%, Pt:Ru atomic ratio of 50:50) was prepared using H₂PtCl₆·6H₂O (Aldrich) and RuCl₃·1.5H₂O (Aldrich) as metal sources, which were dissolved in water/2-propanol solution (25/75, v/v). After this, the carbon Vulcan XC72R, used as a support, was dispersed in the solution using an ultrasonic bath. The resulting mixture (dissolved metal ions and the carbon support) was submitted to gamma irradiation (⁶⁰Co source, dose rate of 0.5 kGy h⁻¹) under stirring at room temperature for 6 h (total dose of 3 kGy). After irradiation, the mixture was filtered, and the solid PtRu/C electrocatalyst was washed with water and dried. In a similar way, the resulting mixture was submitted under stirring at room temperature to an electron beam source for 3 min (Electron Accelerator's Dynamitron job 188-IPEN/CNEN-SP, dose rate 5760 kGy h⁻¹, total dose of 288 kGy) [11].

The Pt:Ru atomic ratios were determined by semiquantitative EDX analysis using a Philips XL30 scanning electron microscope with a 20 keV electron beam and provided with EDAX DX-4.

XRD analysis was performed using a Rigaku diffractometer model Miniflex II using Cu K α radiation source ($\lambda = 0.15406$ nm). The diffractograms were recorded from $2\theta = 20^\circ$ to 90° with a step size of 0.05° and a scan time of 2 s per step. The average crystallite size was calculated using Scherrer equation [12].

Transmission electron microscopy (TEM) was carried out using a JEOL JEM-2100 electron microscope operated at 200 kV. The particle distribution histogram was determined by measuring 150 particles from micrograph.

Electrochemical studies of the electrocatalysts were carried out using the thin porous coating technique [13]. An amount of 20 mg of the electrocatalyst was added to a solution of 50 mL of water containing 3 drops of a 6% polytetrafluoroethylene (PTFE) suspension. The resulting mixture

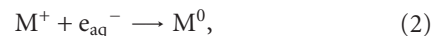
was treated in an ultrasound bath for 10 min, filtered, and transferred to the cavity (0.30 mm deep and 0.36 cm² area) of the working electrode. The quantity of electrocatalyst in the working electrode was determined with an accuracy of 0.0001 g using an analytical balance. In cyclic voltammetry experiments the current values (I) were normalized per gram of platinum (A g_{Pt}⁻¹). The quantity of platinum was calculated considering the mass of the electrocatalyst present in the working electrode multiplied by its percentage of platinum. The reference electrode was a RHE, and the counter electrode was a Pt plate. Electrochemical measurements were made using a Microquimica (model MQPG01, Brazil) potentiostat/galvanostat coupled to a personal computer and using the Microquimica software. Cyclic voltammetry was performed in a 0.5 mol L⁻¹ H₂SO₄ solution saturated with N₂. Methanol oxidation was performed at 25°C using 1.0 mol L⁻¹ of methanol in 0.5 mol L⁻¹ H₂SO₄. For comparative purposes, a commercial PtRu/C E-TEK (20 wt%, Pt:Ru molar ratio 50:50, Lot # B0011117) was used.

3. Results and Discussion

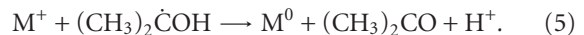
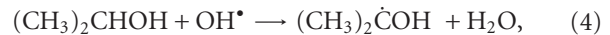
Electron beam or gamma irradiation of a water solution containing metals causes the ionization and excitation of water, forming the species shown in (1) [14].



The aqueous solvated electrons, e_{aq}⁻, and H[•] atoms are strong reducing agents and reduce metal ions down to the zero-valent state ((2) and (3)).



Similarly, multivalent ions, like Pt(IV) and Ru(III), are reduced by multistep reactions. However, OH[•] radicals could oxidize the ions or the atoms into a higher oxidation state and thus counterbalance the reduction reactions, (2) and (3). An OH[•] radical scavenger is therefore added to the solution, in this case 2-propanol, which reacts with these radicals leading to the formation of radicals exhibiting reducing power that are able to reduce metal ions ((4) and (5)) [14].



In this manner, the atoms produced by the reduction of metals ions progressively coalesce leading to the formation of carbon-supported PtRu nanoparticles (PtRu/C electrocatalyst). The results of PtRu/C electrocatalysts preparation using electron beam and gamma irradiation are shown in Table 1.

The water/2-propanol solution containing Pt(IV) and Ru(III) ions used in the preparation of PtRu/C electrocatalysts showed a dark brown color before the addition of the carbon support and irradiation. After irradiation and separation of the solid (PtRu/C electrocatalyst) by filtration, the reaction medium becomes colorless suggesting that all of

TABLE 1: Influence of electron beam and gamma irradiation on Pt : Ru atomic ratio and average crystallite size of the PtRu/C electrocatalysts (20 wt% of metals, nominal Pt : Ru atomic ratio of 50 : 50, water/2-propanol volumetric ratio of 25/75).

Source	Irradiation time (h)	Dose rate (kGy h^{-1})	Total dose (kGy)	Pt : Ru atomic ratio (EDX)	Crystallite size (nm)
Electron beam	0.05	5760.0	288	47 : 53	2.9
Gamma ^{60}Co	6	0.5	3	45 : 55	2.7

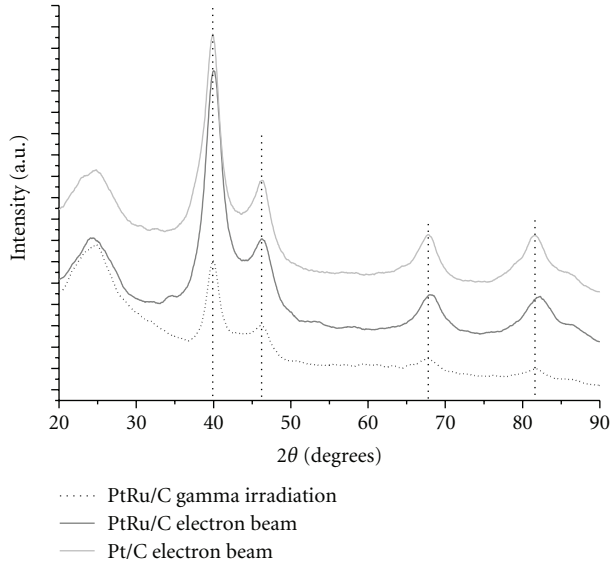


FIGURE 1: X-ray diffractograms of Pt/C and PtRu/C electrocatalysts prepared using electron beam and gamma irradiation.

the Pt(IV) and Ru(III) ions were reduced. To confirm this assumption, a qualitative test using potassium iodide [15] did not detect Pt ions in the filtrates, which suggest that all Pt(IV) ions were reduced to metallic Pt. As no Pt ions were not detected in the filtrates, and the obtained Pt : Ru atomic ratios were similar to the nominal ones (Table 1), it was considered that both electrocatalysts were obtained with 20 wt% of metal loading. Using low dose rate gamma irradiation the total reduction of metal ions was observed only after 6 h of irradiation. On the other hand, only 3 min were necessary to observe the total reduction of the metal ions using high dose rate electron beam irradiation.

The X-ray diffractograms of Pt/C and PtRu/C electrocatalysts are prepared using electron beam, and gamma irradiation are shown in Figure 1.

The X-ray diffractograms showed a broad peak at about 25°, which was associated to the Vulcan XC72R support material and five diffraction peaks at about $2\theta = 40^\circ, 47^\circ, 67^\circ, 82^\circ$, and 87° that were associated to the (111), (200), (220), (311), and (222) planes, respectively, which are characteristic of the face-centered cubic (fcc) structure of platinum and platinum alloys [16]. No peaks, which could be attributed to metallic ruthenium or to materials rich in ruthenium with a hexagonal structure, were observed in the XRD patterns. On

the other hand, the presence of these species as amorphous materials cannot be discarded. The X-ray diffractogram of PtRu/C electrocatalyst prepared using electron beam irradiation showed the diffraction peaks of fcc phase shifted to higher angles with respect to those of Pt/C electrocatalyst, indicating a lattice contraction and some alloy formation. This was not observed for the PtRu/C electrocatalyst prepared using gamma irradiation. The (220) reflection of Pt fcc structure was used to calculate the average crystallite sizes according to Scherrer equation and for both electrocatalysts the calculated values were about 3 nm.

TEM micrographs and the corresponding particle size distribution histograms of the PtRu/C electrocatalysts are prepared using gamma and electron beam irradiations are shown in Figures 2(a) and 2(b), respectively. It can be seen for both electrocatalysts that the nanoparticles were homogeneously distributed on the carbon support, and the mean particle sizes were around 3 and 2.5 nm for the materials obtained using gamma and electron beam irradiation, respectively.

The cyclic voltammograms in acid medium of the PtRu/C electrocatalysts are shown in Figure 3.

The cyclic voltammograms (CV) of both PtRu/C electrocatalysts do not have a well-defined hydrogen adsorption-desorption region (0–0.4 V) and show an increase of the current values in the double-layer region (0.4–0.8 V) when compared to the CV of Pt/C electrocatalyst [17]. The increase of current values in the double region was attributed to the capacitive currents and redox process of ruthenium oxides [17, 18]. However, comparing the CVs of both PtRu/C electrocatalysts, it is observed for the material prepared using electron beam irradiation a more defined hydrogen region when compared to the material prepared using gamma irradiation. On the other hand, the material prepared using gamma irradiation showed the double layer region more pronounced. This could suggest that the material prepared using electron beam irradiation has a surface more enriched in Pt while the material prepared using gamma irradiation has a surface more enriched in Ru.

The electrooxidation of methanol was studied by cyclic voltammetry in 1 mol L^{-1} methanol in 0.5 mol L^{-1} H_2SO_4 (Figure 4).

The electrooxidation of methanol started only at about 0.45 V for the PtRu/C electrocatalyst prepared using gamma irradiation, and the current values were lower than those observed for the PtRu/C electrocatalyst prepared using an electron beam. For the latter electrooxidation started at about 0.35 V, and the performance of this catalyst was very

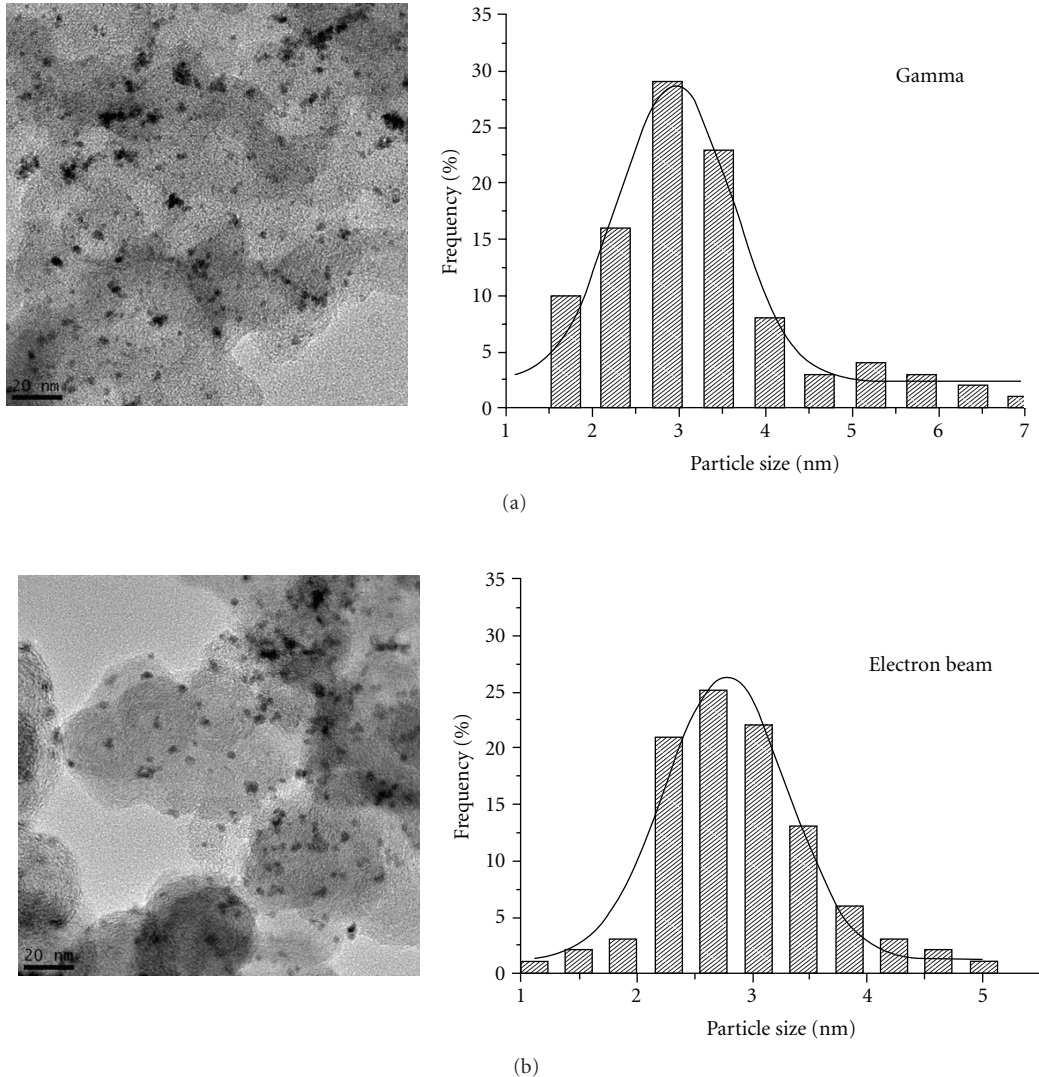


FIGURE 2: TEM micrographs and particle size distributions of PtRu/C electrocatalysts prepared using (a) gamma and (b) electron beam irradiation.

similar to the commercial PtRu/C electrocatalyst from E-TEK. Studies have shown that the maximum activity for methanol oxidation at room temperature could be obtained using PtRu/C electrocatalysts with low Ru coverage [19–21]. The obtained results could be explained by the different dose rates of electron beam and gamma radiation and to different reduction potentials of Pt(IV) and Ru(III) ions. Using electron beam irradiation (high dose rate), the reduction of Pt(IV) and Ru(III) ions proceeds very quickly and enhances the probability of alloying, as confirmed by XRD measurements. Thus, the carbon-supported PtRu nanoparticles obtained using electron beam seem to have a more homogeneous distribution of Pt and Ru atoms on the nanoparticles surface. On the other hand, at low dose rate (gamma source) it seems that the Pt(IV) ions were reduced before the Ru(III) ions. In this case, Ru atoms deposit preferentially on the presupported Pt nanoparticles and

the resulting carbon-supported PtRu nanoparticles have a Ru-rich surface. Another possibility is that Pt(IV) and Ru(III) ions were reduced with equal probabilities by radiolytic radicals, but a further electron transfer from the less noble metal atom, Ru, to the more noble metal ion, Pt(IV), could also result in the formation of carbon-supported PtRu nanoparticles with the surface enriched by Ru atoms, which could explain the low activity of this sample for methanol electrooxidation.

4. Conclusions

An active PtRu/C electrocatalyst for methanol oxidation was easily obtained in a single step within a few minutes using electron beam irradiation. The PtRu/C electrocatalysts showed the typical fcc structure of platinum and platinum

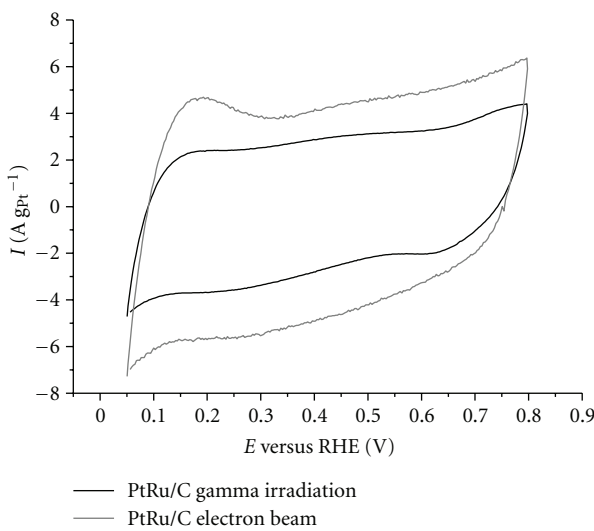


FIGURE 3: Cyclic voltammograms of PtRu/C electrocatalysts prepared using electron beam and gamma irradiation in $0.5 \text{ mol L}^{-1} \text{H}_2\text{SO}_4$ with a scan rate of 10 mV s^{-1} .

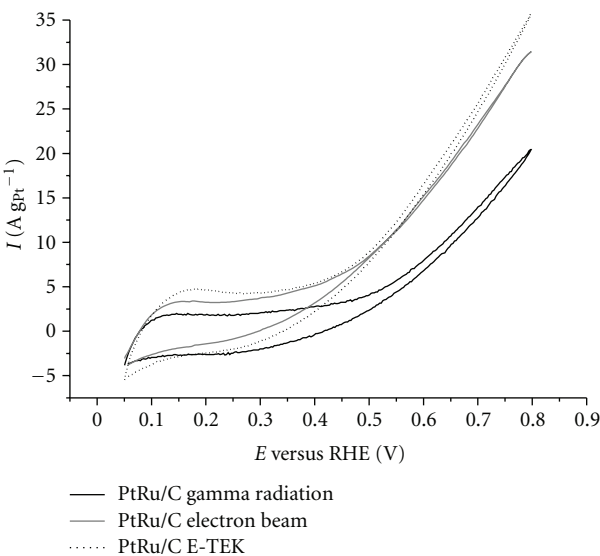


FIGURE 4: Cyclic voltammograms of PtRu/C electrocatalyst prepared using electron beam and gamma irradiation and commercial PtRu/C E-TEK in $0.5 \text{ mol L}^{-1} \text{H}_2\text{SO}_4$ and 1.0 mol L^{-1} methanol with a scan rate of 10 mV s^{-1} .

alloys with average particle sizes of 2.5 nm. At room temperature, the material prepared using electron beam irradiation has a similar methanol oxidation performance as that of a commercial PtRu/C electrocatalyst.

Acknowledgments

The authors thank FAPESP (Proc. no. 2007/08724-7), FINEP-ProH₂ and CNPq for financial support and the collaboration of Elisabeth S.R. Somessari, Carlos Gaia da Silveira, Helio Paes e Samir L. Somessari (CTR-IPEN/CNEN-SP).

References

- [1] H. Wendt, E. V. Spinacé, A. Oliveira Neto, and M. Linardi, "Electrocatalysis and electrocatalysts for low temperature fuel cells: fundamentals, state of the art, research and development," *Química Nova*, vol. 28, no. 6, pp. 1066–1075, 2005.
- [2] L. Schlapbach and A. Züttel, "Hydrogen-storage materials for mobile applications," *Nature*, vol. 414, no. 6861, pp. 353–358, 2001.
- [3] L. Carrete, K. A. Friedrich, and U. Stimming, "Fuel cells: principles, types, fuels, and applications," *Chemical Physics and Physical Chemistry*, vol. 1, p. 162, 2000.
- [4] H. Liu, C. Song, L. Zhang, J. Zhang, H. Wang, and D. P. Wilkinson, "A review of anode catalysis in the direct methanol fuel cell," *Journal of Power Sources*, vol. 155, no. 2, pp. 95–110, 2006.
- [5] C. Lamy, A. Lima, V. LeRhun, F. Delime, C. Coutanceau, and J. M. Léger, "Recent advances in the development of direct alcohol fuel cells (DAFC)," *Journal of Power Sources*, vol. 105, no. 2, pp. 283–296, 2002.
- [6] B. Le Gratiet, H. Remita, G. Picq, and M. O. Delcourt, "CO-stabilized supported Pt catalysts for fuel cells: radiolytic synthesis," *Journal of Catalysis*, vol. 164, no. 1, pp. 36–43, 1996.
- [7] S.-D. Oh, K. R. Yoon, S.-H. Choi et al., "Dispersion of Pt-Ru alloys onto various carbons using γ -irradiation," *Journal of Non-Crystalline Solids*, vol. 352, no. 4, pp. 355–360, 2006.
- [8] H. Wang, X. Sun, Y. Ye, and S. Qiu, "Radiation induced synthesis of Pt nanoparticles supported on carbon nanotubes," *Journal of Power Sources*, vol. 161, no. 2, pp. 839–842, 2006.
- [9] D. F. Silva, A. O. Neto, E. S. Pino, M. Linardi, and E. V. Spinacé, "PtRu/C electrocatalysts prepared using γ -irradiation," *Journal of Power Sources*, vol. 170, no. 2, pp. 303–307, 2007.
- [10] G. S. Chai, B. Fang, and J.-S. Yu, " γ -Ray irradiation as highly efficient approach for synthesis of supported high Pt loading cathode catalyst for application in direct methanol fuel cell," *Electrochemistry Communications*, vol. 10, no. 11, pp. 1801–1804, 2008.
- [11] E. V. Spinacé, A. O. Neto, M. Linardi, D. F. Silva, E. S. Pino, and V. A. Cruz, Patent BR200505416, 2005.
- [12] V. Radmilovic, H. A. Gasteiger, and P. N. Ross, "Structure and chemical composition of a supported Pt-Ru electrocatalyst for methanol oxidation," *Journal of Catalysis*, vol. 154, no. 1, pp. 98–106, 1995.
- [13] A. Oliveira Neto, M. J. Giz, J. Perez, E. A. Ticianelli, and E. R. Gonzalez, "The electro-oxidation of ethanol on Pt-Ru and Pt-Mo particles supported on high-surface-area carbon," *Journal of the Electrochemical Society*, vol. 149, no. 3, pp. A272–A279, 2002.
- [14] J. Belloni, M. Mostafavi, H. Remita, J. L. Marignier, and M. O. Delcourt, "Radiation-induced synthesis of mono- and multi-metallic clusters and nanocolloids," *New Journal of Chemistry*, vol. 22, no. 11, pp. 1239–1255, 1998.
- [15] H. G. Julsing and R. I. McCrindle, "Colorimetric method for the determination of residual Pt in treated acidic effluents," *South African Journal of Chemistry*, vol. 53, no. 2, pp. 86–89, 2000.
- [16] *Powder Diffraction File: 01-087-0646*, vol. PDF-2, Joint Committee on Powder Diffraction Standards, International Center for Diffraction Data, Newtown Square, Pa, USA, 2010.
- [17] G. A. Camara, R. B. de Lima, and T. Iwasita, "Catalysis of ethanol electrooxidation by PtRu: the influence of catalyst composition," *Electrochemistry Communications*, vol. 6, no. 8, pp. 812–815, 2004.

- [18] L. P. R. Profeti, F. C. Simões, P. Olivi et al., "Application of Pt + RuO₂ catalysts prepared by thermal decomposition of polymeric precursors to DMFC," *Journal of Power Sources*, vol. 158, no. 2, pp. 1195–1201, 2006.
- [19] T. Iwasita, "Electrocatalysis of methanol oxidation," *Electrochimica Acta*, vol. 47, no. 22–23, pp. 3663–3674, 2002.
- [20] F. Maillard, F. Gloaguen, and J. M. Leger, "Preparation of methanol oxidation electrocatalysts: ruthenium deposition on carbon-supported platinum nanoparticles," *Journal of Applied Electrochemistry*, vol. 33, no. 1, pp. 1–8, 2003.
- [21] E. V. Spinacé, A. O. Neto, and M. Linardi, "Electro-oxidation of methanol and ethanol using PtRu/C electrocatalysts prepared by spontaneous deposition of platinum on carbon-supported ruthenium nanoparticles," *Journal of Power Sources*, vol. 129, no. 2, pp. 121–126, 2004.

Research Article

Virus-Assembled Flexible Electrode-Electrolyte Interfaces for Enhanced Polymer-Based Battery Applications

Ayan Ghosh,¹ Juchen Guo,¹ Adam D. Brown,² Elizabeth Royston,² Chunsheng Wang,¹ Peter Kofinas,³ and James N. Culver^{2,4}

¹ Department of Chemical and Biomolecular Engineering, University of Maryland, College Park, MD 20742, USA

² Institute for Bioscience and Biotechnology Research, University of Maryland, College Park, MD 20742, USA

³ Fischell Department of Bioengineering, University of Maryland, College Park, MD 20742, USA

⁴ Department of Plant Science and Landscape Architecture, University of Maryland, College Park, MD 20742, USA

Correspondence should be addressed to James N. Culver, jculver@umd.edu

Received 19 December 2011; Accepted 26 January 2012

Academic Editor: Mauro Coelho dos Santos

Copyright © 2012 Ayan Ghosh et al. This is an open access article distributed under the Creative Commons Attribution License, which permits unrestricted use, distribution, and reproduction in any medium, provided the original work is properly cited.

High-aspect-ratio cobalt-oxide-coated Tobacco mosaic virus (TMV-) assembled polytetrafluoroethylene (PTFE) nonstick surfaces were integrated with a solvent-free polymer electrolyte to create an anode-electrolyte interface for use in lithium-ion batteries. The virus-assembled PTFE surfaces consisted primarily of cobalt oxide and were readily intercalated with a low-molecular-weight poly(ethylene oxide) (PEO) based diblock copolymer electrolyte to produce a solid anode-electrolyte system. The resulting polymer-coated virus-based system was then peeled from the PTFE backing to produce a flexible electrode-electrolyte component. Electrochemical studies indicated the virus-structured metal-oxide PEO-based interface was stable and displayed robust charge transfer kinetics. Combined, these studies demonstrate the development of a novel solid-state electrode architecture with a unique peelable and flexible processing attribute.

1. Introduction

The high energy, power densities, and excellent cycling stability of lithium-ion batteries have made them the preferred system for many portable electronic applications [1]. However, the liquid-based organic electrolytes commonly used in these systems are typically flammable and impose weight and size constraints that significantly limit their application [2]. To mitigate these issues, recent efforts have focused on the development of solid-state polymer-based lithium-ion electrolytes [3–7]. Polymer-based electrolytes can be readily processed to produce thin films that can be configured into a range of packaging shapes and coatings. In addition, the composition and self-assembly aspects of different block copolymer electrolytes can be combined and tuned to create electrolyte architectures tailored to enhance specific battery properties [8–11]. These polymer-based systems are also generally lighter and resistant to fire, making them safer and potentially more economical to use. However, a key obstacle in the use of polymer-based electrolytes is their reduced ionic

conductivity and the high interfacial resistance that occurs between the electrode and the solid electrolyte. One method to enhance the charge transfer and rate performance in these systems is to create nanoscale three-dimensional electrode-electrolyte interfaces with increased surface areas and shortened Li⁺ diffusion lengths. Unfortunately, it is currently difficult to achieve such three-dimensional nanoscale electrode-solid electrolyte interfaces using traditional micromachining and casting methodologies [12, 13]. Thus, there is a need to identify novel methods to interface polymer electrolytes with three-dimensional electrode patterning capabilities.

Biological macromolecules encode unique properties that include self-assembly, genetic programmability, and diverse functionalities that have made them attractive building blocks for the development of nanoparticles and surface features [14, 15]. In particular, the uniform structure and assembly processes of virus particles have been used to develop battery electrodes and memory devices [13, 16–18]. For example, Nam et al. [13] demonstrated the use of M13 virus in the fabrication of a two-dimensional electrode-polymer

electrolyte interface with enhanced battery applications. Previous efforts by our group have developed a novel combination of genetically engineered *Tobacco mosaic virus* (TMV) and electroless plating techniques to obtain near uniform inorganic coatings of Ni, Co, Pt, and silica on three-dimensionally patterned virus templates [18–21]. TMV produces a rod-shaped particle of 300 nm in length by 18 nm in diameter with a 4 nm wide central channel. Individual particles are assembled from ~2130 identical 17.5 kDa coat protein subunits wrapped in a helical array around the virus' single-stranded RNA genome. Using the known three-dimensional structure of TMV, we created novel coat protein mutants such as TMV1cys, which has a unique cysteine codon within the N-terminus of the coat protein open reading frame [18]. The positioning of the 1cys mutation directs viral rod attachment via its 3' end onto gold and other surfaces, including stainless steel and SiN [18, 22]. Combined with electroless plating methods, this process yields high aspect ratio surfaces composed of evenly coated virus templates containing confluent metal coatings as thin as 15 nm in thickness [18, 22]. These virus-assembled surfaces have been shown to enhance anode function in Ni-Zn and Li-Si battery systems [18, 23].

In this study, we demonstrate the production of virus assembled three-dimensional electrodes on nonstick polytetrafluoroethylene (PTFE) surfaces. The PTFE-assembled virus enhanced electroless coatings of cobalt and served as a robust template for the casting of a poly (ethylene oxide) (PEO) and poly (methyl methacrylate) (PMMA) based block copolymer that possesses a high transference number and excellent electrochemical properties [6, 7]. The resulting virus-assembled-polymer electrolyte system was easily peeled from the PTFE surface to produce a flexible electrode-electrolyte interface with stable electrochemical properties.

2. Materials and Methods

2.1. Virus Assembly, Patterning, and Coatings. A PTFE substrate was used for electrode release studies and SEM observations, while an Au-coated stainless steel substrate, in the form of a CR2032 coin disk, was used for electrochemical testing. To pattern the virus-structured PTFE surfaces, a parafilm mask with 1 cm² square opening was applied to a PTFE-coated substrate (Bytac Saint-Gobain Performance Plastics Poestenkill, NY). Virus-assembled surfaces were prepared by immersing the parafilm-patterned PTFE or Au-coated stainless steel discs in a solution of 0.2 mg/mL purified TMV1cys in 0.1 M pH 7 phosphate buffer and incubating overnight [18]. Cobalt-coated TMV electrodes were prepared using an electroless plating method as described in Royston et al. [18]. In summary, a 0.02 M solution of Na₂PdCl₄ in methanol was added to the virus solution to a final Na₂PdCl₄ concentration of 0.0015 M and allowed to incubate for 30 minutes. The virus solution was then removed and replaced with a cobalt electroless plating solution consisting of 0.033 M cobalt (II) sulfate, 0.008 M glycine, 0.5 M sodium tetraborate, and 0.175 M dimethylamine borane. The plating reaction was allowed to proceed for 10 minutes. The plating solution was then removed and the

virus-coated surface washed with ethanol and dried overnight under vacuum before being moved into an argon-filled glovebox.

2.2. Analysis of Virus-Assembled Surfaces. Virus-assembled surfaces were visualized using a Hitachi field emission scanning electron microscope (FESEM) at 5–20 kV accelerating potential. X-ray photoelectron spectroscopy (XPS) was performed using a Kratos Axis 165 X-ray photoelectron spectrometer operating in hybrid mode, using monochromatic AlK α radiation (1486.6 eV) at 220 W. Survey spectra and high-resolution spectra were collected with a pass energy of 160 eV and 20 eV, respectively. All data were calibrated to the hydrocarbon contamination peak at 284.8 eV. Peak fitting was carried out using CASA XPS software (<http://www.casaxps.com/>). Peaks were fit with a 70% Gaussian, 30% Lorentzian peak shape after subtraction of a Shirley background. X-ray diffraction (XRD) pattern was recorded on a Bruker Smart1000 using CuK α radiation.

2.3. Preparation of the Polymer Electrolyte Membrane. The PEO-*b*-PMMA block copolymer (Molecular weight, 3000 : 500 for PEO : PMMA) (Polymer Source Inc.) was used as starting material to synthesize the diblock copolymer PEO-*b*-(PMMA-*ran*-PMAALi) [6]. Electrolyte films were prepared inside an argon glove box. The diblock copolymer PEO-*b*-(PMMA-*ran*-PMAALi) and LiBOB (Chemetall GmbH) were mixed in previously optimized compositions of 4 : 1 (PEO : LiBOB) and dissolved in anhydrous and degassed tetrahydrofuran (THF) [6, 7]. Electrolyte membranes were then prepared by solution casting onto the virus-assembled Bytac molds or virus-assembled Au-coated stainless steel disks resulting in translucent polymer films. The drying process lasted for several days under an argon atmosphere, followed by at least 48 hours of drying under vacuum. The resulting block copolymer has a low molecular weight and a high salt loading capacity, resulting in enhanced conductivity and transference numbers [7]. Cross-sectioning of the electrode-electrolyte interface was carried out in an argon glove box using a scalpel. Cross-sections were then transported inside a sealed vial under argon and quickly mounted on an FESEM sample holder followed by placement under vacuum to limit exposure to moisture.

2.4. Half-Cell Assembly and Testing. To demonstrate the electrochemical performance of the electrode-polymer electrolyte assembly, half-cells with Li metal as a counter electrode were assembled and tested in CR2032 coin cells. Solution casting of the block copolymer onto the virus assembled Au-coated stainless steel current collector was done as described above. Washers made from Celgard membranes were used as separators to standardize the area between the virus-assembled polymer electrolyte and the Li metal counter electrode. CR2032 coin cells were annealed at 75°C for at least 48 hrs before electrochemical testing. Cycling studies were performed at 80°C at various charge-discharge rates to study the dynamics of the half-cell's capacity performance between 3 and 0.3 volts using an Arbin battery test station.

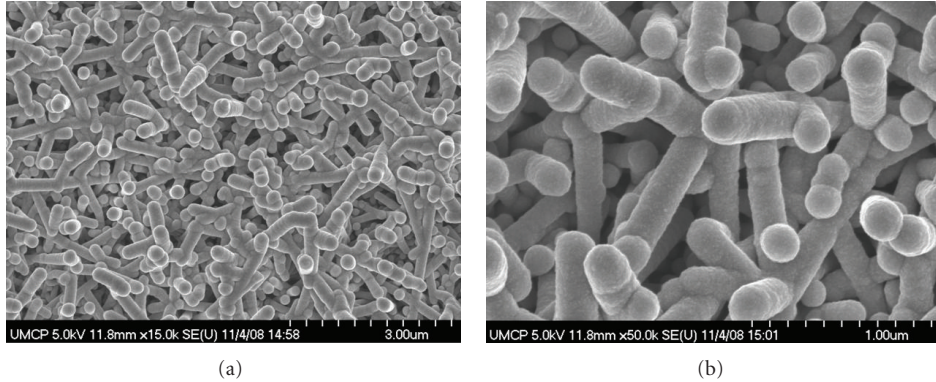


FIGURE 1: SEM analysis of cobalt-coated TMV1cys assembled surface at (a) 15 K and (b) 50 K.

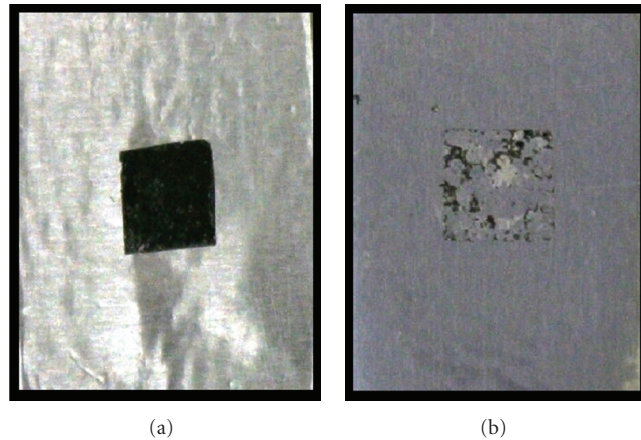


FIGURE 2: Electroless cobalt coatings on (a) a patterned TMV1cys assembled PTFE surface and (b) a patterned unmodified PTFE surface. Parafilm masks were used to delineate 1 cm² square openings.

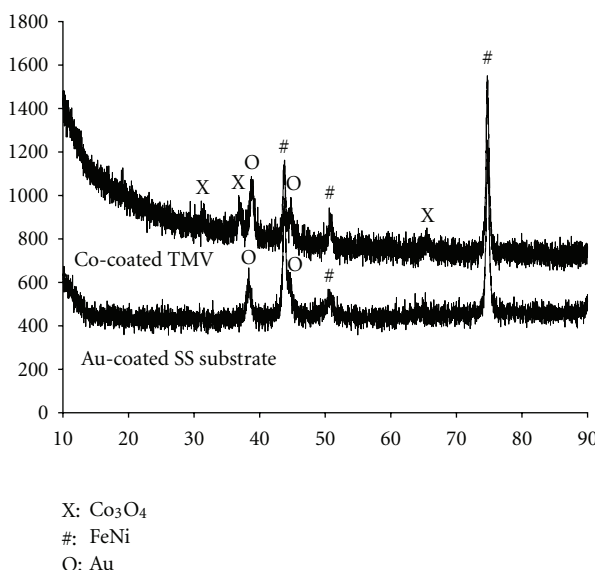


FIGURE 3: XRD analysis of a cobalt-coated virus-assembled surface. Peaks labeled with X are Co₃O₄, # are FeNi, and O are Au.

3. Results and Discussion

Previous studies demonstrated that TMV1cys binds in an oriented fashion to numerous surfaces including gold, stainless steel, and the polymer SU-8 [18, 21]. In this study, we demonstrate for the first time that TMV1cys is capable of similarly interacting with PTFE surfaces. Scanning electron microscopy (SEM) was used to study the 3 D TMV-templated cobalt oxide electrode structure. Figure 1 shows the SEM images of cobalt-coated TMV1cys at 15 k and 50 k magnifications. The rod-shaped virus is generally attached to the surface at one end and largely oriented away from the underlying PTFE. This configuration significantly increases reactive surface area by as much as 80-fold depending upon virus concentration [23]. The electroless plating process can be seen to provide very consistent and reproducible cobalt coatings that have a continuous metal layer ~20 nm in thickness. Attempts to assemble the unmodified wild-type virus onto the PTFE surface were unsuccessful (data not shown) indicating that the thiol groups on the TMV1cys virus are critical for assembly on PTFE surfaces. Based on this finding, we hypothesize that the electronegativity of the PTFE attracts

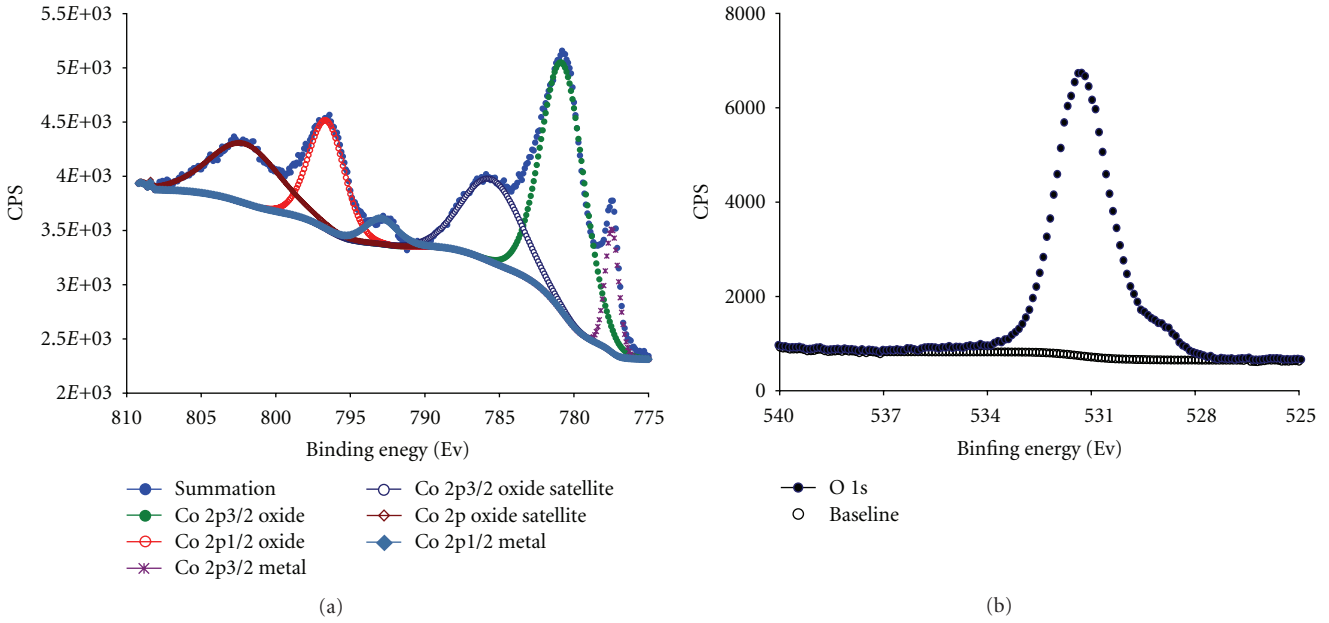


FIGURE 4: XPS spectrum of the (a) Co 2p_{3/2} and (b) O 1s peaks from a cobalt-coated TMV1cys surface.

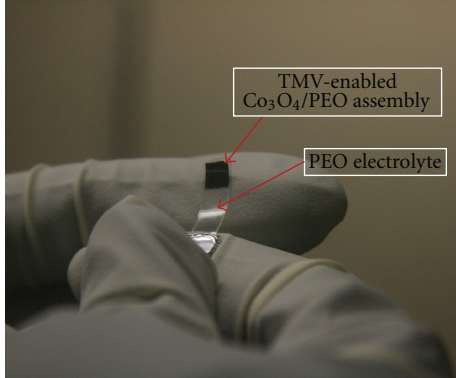


FIGURE 5: Flexible polymer electrolyte-TMV1cys templated electrode half-cell. Virus assembly, cobalt coating, and polymer casting were done on a PTFE (Bytac) surface. The assembled half-cell was then peeled from the PTFE surface (picture taken inside an argon glovebox).

the sulphydryl groups exposed at the end of the TMV1cys particle, thus allowing the virus to form a noncovalent association with the PTFE surface. Once assembled on the PTFE surface, TMV1cys functions as a robust template for the deposition of cobalt and other metals via electroless plating as previously described [18, 23]. The inability to produce uniform cobalt coatings on bare PTFE via electroless plating further demonstrates the importance of the assembled TMV1cys as a template for the attraction and deposition of metals on this surface (Figure 2).

Analysis of the cobalt-coated TMV1cys substrates was performed to determine the suitability of this material to function as a battery electrode. XRD patterns generated from the gold-coated stainless steel substrate and a similar

substrate carrying the cobalt-coated TMV1cys are shown in Figure 3. The XRD pattern of the substrate alone shows the characteristic peaks for FeNi alloy that is the main component of the stainless steel and the peaks for the Au coating. The XRD pattern from the cobalt coated TMV1cys substrate clearly shows additional peaks at 30.6°, 36.7°, and 64.8° beside the peaks for stainless steel and Au. The positions of these new peaks are consistent with the XRD pattern of crystalline Co₃O₄. Similarly, high-resolution XPS scans for Co 2p show a ratio of ~10% metal and ~90% oxide with Co 2+ in the high spin state (Figure 4). This amount of oxide at the surface was consistent with the exposure of the metal surface to air. Combined these elemental studies indicate that the cobalt-coated virus surfaces are sufficient for electrode function.

Solution casting of the block copolymer electrolyte onto the cobalt-coated virus-assembled PTFE surface produced flexible translucent films as seen in Figure 5. Once the polymer film was dried, it could be easily peeled from the PTFE surface, leaving no residue from the virus-patterned electrode behind. Cross-sections of the electrode-electrolyte assembly were studied using SEM as shown in Figure 6. The lower-magnification SEM image (Figure 6(a)) clearly shows the flat released backside of the TMV1cys electrode that was peeled from the PTFE surface. The higher-magnification SEM image (Figure 6(b)) shows that the casting method permits the polymer electrolyte to fully intercalate within the three-dimensional TMV1cys electrode. The integration of the polymerized diblock copolymer provides the means for the simple release of the cobalt-coated virus electrode from the mold. The ability to cleanly peel off the cobalt-coated virus templates from the PTFE surface represents a unique means of patterning and producing flexible nanofeatured electrode-electrolyte interfaces.

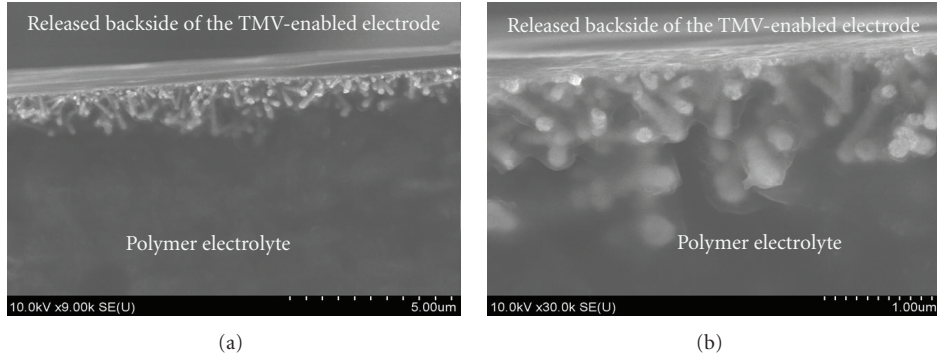


FIGURE 6: SEM images showing the TMV1cys assembled polymer-electrode interface at (a) 9 K and (b) 30 K. The polymer electrolyte-virus electrode half-cell was peel-released from a PTFE (Bytac) surface before being sliced with a scalpel and mounted for SEM visualization.

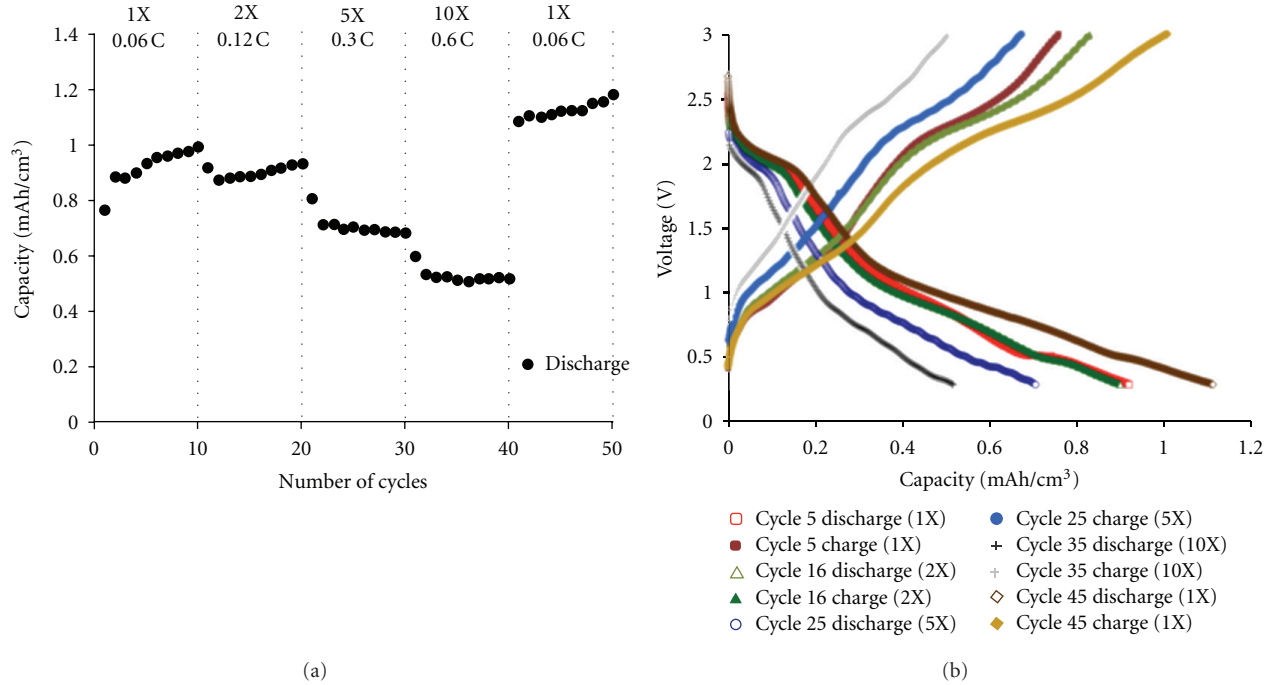


FIGURE 7: Capacity profile at different C rates (a) and the charge-discharge profile at corresponding cycles (b) of the TMV1cys assembled PEO-*b*-(PMMA-*ran*-PMAALi) half-cell when galvanostatically cycled at 80°C.

To characterize the electrochemical properties of the TMV1cys enabled electrode-electrolyte interface, a coin-cell-assembled electrode was discharged (lithiation) and charged (delithiation) at various current densities at 80°C. Figure 7 shows the rate performance of the TMV polymer electrode and the charge/discharge curves at different current densities. The TMV1cys electrode shows a stable initial capacity of 0.7 mAh cm⁻² at 0.06 C. Subsequent increases in the C rate by two-, five-, and ten-fold produce only incremental losses in electrode capacity (Figure 7(a)). In addition, restoration to the original C rate fully restored electrode capacity. These observations are consistent with good charge transfer kinetics at the electrode-electrolyte interface and indicate that the virus-assembled cobalt anode is in good contact with the block copolymer electrolyte and that this contact is stable

throughout the experiment. Combined these data indicate that the virus-patterned cobalt oxide surfaces can be readily intercalated with a polymer electrolyte to produce robust high-surface-area solid-state electrode-electrolyte interfaces.

4. Conclusion

The demand for portable electronic devices is driving the development of compact power sources that combine enhanced energy storage characteristics with flexible battery architectures that are both safe and durable. Here, we describe the development of a novel virus-assembled electrode-electrolyte interface system that effectively produces tailored battery components of various form factors. This electrolyte-electrode interface leverages the use of a biologically driven

assembly process to produce a three-dimensional nanostructured conductive surface of high area. The TMV1cys assembly process also provides a robust surface for the deposition of electrode metals that could not otherwise be obtained on a PTFE surface. This electrode-electrolyte interface is further enhanced by the use of a low-molecular weight block copolymer electrolyte material that efficiently intercalates within the nanostructured electrode surface to produce a flexible electrode backing. Combined with the virus' ability to assemble onto nonstick PTFE surfaces, this process represents a novel approach toward the production of peelable battery components that can address the size and shape constraints of device designs.

Acknowledgments

This research was partially supported by the US Department of Energy, Office of Basic Energy Science, Division of Materials Science and Engineering, Biomolecular Materials Research Program (DEFG02-02-ER45975). The authors also thank Dr. Karen Gaskell for XPS analysis and gratefully acknowledge shared experimental facilities support from the NSF MRSEC under Grant DMR 05-20471.

References

- [1] J. M. Tarascon and M. Armand, "Issues and challenges facing rechargeable lithium batteries," *Nature*, vol. 414, no. 6861, pp. 359–367, 2001.
- [2] E. Quararone and P. Mustarelli, "Electrolytes for solid-state lithium rechargeable batteries: recent advances and perspectives," *Chemical Society Reviews*, vol. 40, no. 5, pp. 2525–2540, 2011.
- [3] W. H. Meyer, "Polymer electrolytes for lithium-ion batteries," *Advanced Materials*, vol. 10, no. 6, pp. 439–448, 1998.
- [4] G. B. Appetecchi, F. Croce, G. Dautzenberg et al., "Composite polymer electrolytes with improved lithium metal electrode interfacial properties: I. Electrochemical properties of dry PEO-LiX systems," *Journal of the Electrochemical Society*, vol. 145, no. 12, pp. 4126–4132, 1998.
- [5] P. P. Soo, B. Huang, Y. I. I. Jang, Y. M. Chiang, D. R. Sadoway, and A. M. Mayes, "Rubbery block copolymer electrolytes for solid-state rechargeable lithium batteries," *Journal of the Electrochemical Society*, vol. 146, no. 1, pp. 32–37, 1999.
- [6] A. Ghosh and P. Kofinas, "Nanostructured block copolymer dry electrolyte," *Journal of the Electrochemical Society*, vol. 155, no. 6, pp. A428–A431, 2008.
- [7] A. Ghosh, C. Wang, and P. Kofinas, "Block copolymer solid battery electrolyte with high Li-ion transference number," *Journal of the Electrochemical Society*, vol. 157, no. 7, pp. A846–A849, 2010.
- [8] T. Niitani, M. Amaki, H. Nakano, K. Dokko, and K. Kanamura, "Star-shaped polymer electrolyte with microphase separation structure for all-solid-state lithium batteries," *Journal of the Electrochemical Society*, vol. 156, no. 7, pp. A577–A583, 2009.
- [9] S. C. Mui, P. E. Trapa, B. Huang et al., "Block copolymer-templated nanocomposite electrodes for rechargeable lithium batteries," *Journal of the Electrochemical Society*, vol. 149, no. 12, pp. A1610–A1615, 2002.
- [10] S. E. Bullock and P. Kofinas, "Synthesis of an A/B/C triblock copolymer for battery materials applications," *Macromolecules*, vol. 37, no. 5, pp. 1783–1786, 2004.
- [11] M. Singh, O. Odusanya, G. M. Wilmes et al., "Effect of molecular weight on the mechanical and electrical properties of block copolymer electrolytes," *Macromolecules*, vol. 40, no. 13, pp. 4578–4585, 2007.
- [12] J. W. Long, B. Dunn, D. R. Rolison, and H. S. White, "Three-dimensional battery architectures," *Chemical Reviews*, vol. 104, no. 10, pp. 4463–4492, 2004.
- [13] K. T. Nam, R. Wartena, P. J. Yoo et al., "Stamped microbattery electrodes based on self-assembled M13 viruses," *Proceedings of the National Academy of Sciences of the United States of America*, vol. 105, no. 45, pp. 17227–17231, 2008.
- [14] C. C. Dufort and B. Dragnea, "Bio-Enabled synthesis of meta-materials," *Annual Review of Physical Chemistry*, vol. 61, pp. 323–344, 2010.
- [15] F. Barthelat, "Biomimetics for next generation materials," *Philosophical Transactions A*, vol. 365, no. 1861, pp. 2907–2919, 2007.
- [16] K. T. Nam, D. W. Kim, P. J. Yoo et al., "Virus-enabled synthesis and assembly of nanowires for lithium ion battery electrodes," *Science*, vol. 312, no. 5775, pp. 885–888, 2006.
- [17] R. J. Tseng, C. Tsai, L. Ma, J. Ouyang, C. S. Ozkan, and Y. Yang, "Digital memory device based on Tobacco mosaic virus conjugated with nanoparticles," *Nature nanotechnology*, vol. 1, no. 1, pp. 72–77, 2006.
- [18] E. Royston, A. Ghosh, P. Kofinas, M. T. Harris, and J. N. Culver, "Self-assembly of virus-structured high surface area nanomaterials and their application as battery electrodes," *Langmuir*, vol. 24, no. 3, pp. 906–912, 2008.
- [19] S. Y. Lee, J. Choi, E. Royston, D. B. Janes, J. N. Culver, and M. T. Harris, "Deposition of platinum clusters on surface-modified Tobacco mosaic virus," *Journal of Nanoscience and Nanotechnology*, vol. 6, no. 4, pp. 974–981, 2006.
- [20] E. S. Royston, A. D. Brown, M. T. Harris, and J. N. Culver, "Preparation of silica stabilized Tobacco mosaic virus templates for the production of metal and layered nanoparticles," *Journal of Colloid and Interface Science*, vol. 332, no. 2, pp. 402–407, 2009.
- [21] K. Gerasopoulos, M. McCarthy, P. Banerjee, X. Fan, J. N. Culver, and R. Ghodssi, "Biofabrication methods for the patterned assembly and synthesis of viral nanotemplates," *Nanotechnology*, vol. 21, no. 5, Article ID 055304, 2010.
- [22] K. Gerasopoulos, M. McCarthy, E. Royston, J. N. Culver, and R. Ghodssi, "Nanostructured nickel electrodes using the Tobacco mosaic virus for microbattery applications," *Journal of Micromechanics and Microengineering*, vol. 18, no. 10, Article ID 104003, 2008.
- [23] X. Chen, K. Gerasopoulos, J. Guo et al., "Virus-enabled silicon anode for lithium-ion batteries," *ACS Nano*, vol. 4, no. 9, pp. 5366–5372, 2010.

Research Article

Synthesis of High-Quality Carbon Nanotube Arrays without the Assistance of Water

Yongfeng Luo,^{1,2} Xinjun Wang,² Mengdong He,² Xi Li,² and Hong Chen²

¹ Institute of Powder Metallurgy, Central South University, Hunan, Changsha 410083, China

² Institute of Mathematics and Physics, Central South University of Forestry and Technology, Hunan, Changsha 410004, China

Correspondence should be addressed to Yongfeng Luo, lyfmku@163.com and Hong Chen, chenhongcs@126.com

Received 2 November 2011; Accepted 5 February 2012

Academic Editor: Arava Leela Mohana Reddy

Copyright © 2012 Yongfeng Luo et al. This is an open access article distributed under the Creative Commons Attribution License, which permits unrestricted use, distribution, and reproduction in any medium, provided the original work is properly cited.

Long and high-quality carbon nanotube (CNT) arrays have been synthesized through a chemical vapor deposition process. The Fe/Al₂O₃ on silicon was used as the catalyst, ethylene as the carbon source, and a gas mixture of Ar and H₂ gases as the carrying gas. It is found for the first time that the high-quality and superlong carbon nanotube array can be improved by varying the content of hydrogen and carbon source.

1. Introduction

Carbon nanotubes (CNTs) have been extensively studied recently due to their unique structures and excellent mechanical, electrical, and chemical properties [1–14]. The special characteristics of carbon nanotubes arise from their atomic structures, number of walls, diameters, and lengths. For example, CNTs can be either metals or semiconductors depending on chirality and diameters [15, 16]. The alignment, diameter, and number of walls of a CNT significantly affect its mechanical and electrical properties and thus can impact a wide range of applications such as probe microscopy tips [17, 18], field emission devices [19], solar cells [7, 20], electromechanical devices [21], and structural composites [22, 23]. Recently, new technology based on the properties of very long aligned CNTs has been developing rapidly. The long nanotubes can be spun into fibers [20, 24–30] that are much stronger than all current structural materials. This will allow revolutionary advances in lightweight and high-strength applications. Intense research efforts have been undertaken to synthesize aligned long CNTs [31–38]; nevertheless, many limitations to the synthesis of very long aligned CNTs remain. Recently, the Iijima [38] group succeeded in growing 2.5 mm long aligned single-walled carbon nanotubes of high purity using the water-assisted chemical vapor deposition (CVD) technique. For

the synthesis of very long aligned CNTs by CVD technique, the catalyst activity and lifetime are very important factors. The coating of the catalyst particles by amorphous carbon during CVD reduces the catalyst activity and stops the growth of CNTs. The successful synthesis of very long CNTs can be achieved if the catalyst activity and lifetime can be enhanced [38]. The control of the diameter and number of walls of CNTs represents one of the most basic issues in developing nanotube growth methods. There are some reports that the size of the catalyst used in thermal catalytic CVD can define the diameter of as-grown nanotubes [39–41]. This hypothesis has been supported by the observation that catalytic particles at the ends of CVD-grown CNTs have sizes commensurate with the nanotube diameters. The direct growth of long CNTs with a tunable number of walls by adjusting the catalyst thickness can be very promising due to its simplicity and the possibility of wide applications, which have not been yet reported. Accordingly, the developments of synthesis techniques that can control the length, diameter, alignment, and number of walls of the nanotubes have become the most important part of intense research. In the present study, we report the successful synthesis of 4 mm-long aligned CNTs by improving the flow ratio of hydrogen in the catalytic thermal CVD technique without water assistance.

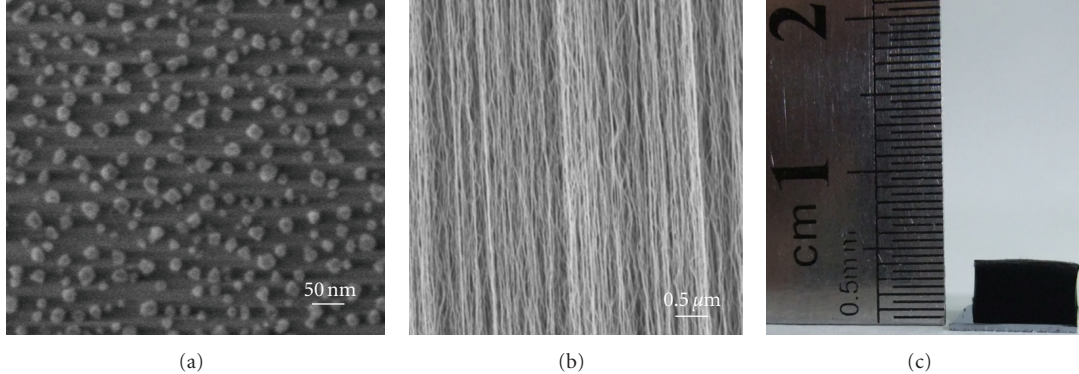


FIGURE 1: (a) SEM images of the catalytic iron nanoparticles after the heating treatment in simulating the CNT synthesis without introduction of the carbon source; (b) SEM image showing sidewall of well-aligned CNTs after the growth for 180 min; (c) optical image of 4.0 mm long CNT arrays after the growth for 180 min.

2. Experimental

The long aligned CNTs were synthesized using a conventional CVD technique. High-quality and long CNTs arrays were synthesized in an atmospheric pressure quartz tube furnace having the inner diameter of 47 mm. Ar with 30% H₂ was used as a carrier gas, and pure ethylene served as the carbon source. CNTs growth was performed in quartz tube furnace. High-purity ethylene (99.999%) was used as the source gas of carbon. Argon (99.999%) was used as a carrier gas, and hydrogen (99.999%) was introduced with Ar at 1 atm pressure.

Typical CVD growth was carried out at 750°C. During heating of the reactor, a steady flow of 300 sccm argon and 150 sccm H₂ was maintained into the chamber. After the growth temperature was attained, the total gas flow rate throughout the deposition process was maintained at 500 sccm. The optimum CVD condition was determined by balancing the relative levels of ethylene and H₂. This sharp optimum condition was achieved for the growth of long aligned CNTs array by studying the dependence of the height of CNTs on ethylene-to-H₂ ratios, which has been reported earlier. In contrast to the report of Hata et al. [38] where the catalyst was active only for 30 min, we achieved very long time (ca. 3 h) catalyst activity by optimizing the CVD parameters very accurately, which resulted in the growth of aligned CNTs as long as 4 mm. Si wafers (5 mm × 5 mm) with 1 μm thickness SiO₂ layer were used as the substrate for the growth of long CNTs. The Al₂O₃ layer of thicknesses (10 nm) was used as a buffer layer between the Si/SiO₂ substrate and the catalyst. The Al₂O₃ layer was deposited on the substrate on which thicknesses (1.0 nm) of Fe catalyst layer were deposited to grow CNTs. Both the catalyst and buffer layers were deposited by an e-beam evaporation technique. The progress was normally for few seconds (5 s for 1.0 nm thick Fe catalyst) to achieve catalyst thicknesses. The variation of Fe catalyst thickness was found to be most effective for controlling the number of walls of the aligned CNTs. The CNTs array with thicknesses up to 4.0 mm can be synthesized by improving the flow ratio of hydrogen to 30%. Amount

of hydrogen is much larger than the 6% of total flow gas reported previously.

The microstructures of the deposited nanotubes were studied by scanning electron microscopy (SEM, Hitachi FE-SEM S4800 operated at 1 kV) and transmission electron microscopy (TEM, JEOL JEM-2100F operated at 200 kV). TEM samples were prepared by drop-casting CNT/ethanol solutions onto copper grids in the open air. Raman measurements were performed on Renishaw in Via Reflex with excitation wavelength of 514.5 nm and laser power of 20 mW at room temperature.

3. Results and Discussion

Long CNTs array up to 4.0 mm was synthesized through a chemical vapor deposition process. The experimental results showed that the synthesis of aligned CNTs is very sensitive to the CVD parameters. The large amount of hydrogen during CVD plays a critical role in synthesizing long aligned CNTs. The hydrogen acts like a weak oxidizer and helps to remove the amorphous carbon deposited on the catalyst surface during CVD. The deposition of amorphous carbon layer on the catalyst surface reduces the activity and lifetime of the catalyst; as a result long continuous CNTs cannot be synthesized. By optimizing the CVD parameters and the hydrogen concentration, it is possible to grow long CNTs with high reproducibility.

It seems that upon heating to CNTs growth temperature the Fe nanoparticles formation occurred from the thin Fe layer. These particles were then trapped in the holes of the Al₂O₃ surface. The shape of the metal particles was also guided by the dip traps of the Al₂O₃ surface, and the appropriate shape of the nanoparticles is very important for growing high-quality CNTs. The surface morphology of the Fe-coated Al₂O₃ surface was also studied by scanning electron microscopy (SEM) (Figure 1(a)), and the Fe film breaks into uniform nanoparticles with an average size of about 14 nm. SEM images of the aligned CNTs deposited for 30 min by using Fe catalyst layer (1.0 nm) are shown

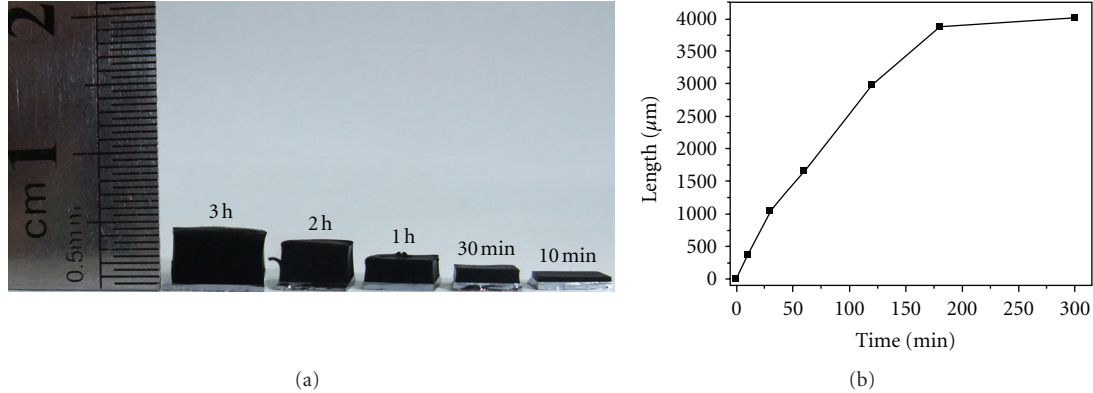


FIGURE 2: (a) and (b): growth length of CNT array with time at 750°C and with ethylene and carrier-gas flow rates at 500 sccm.

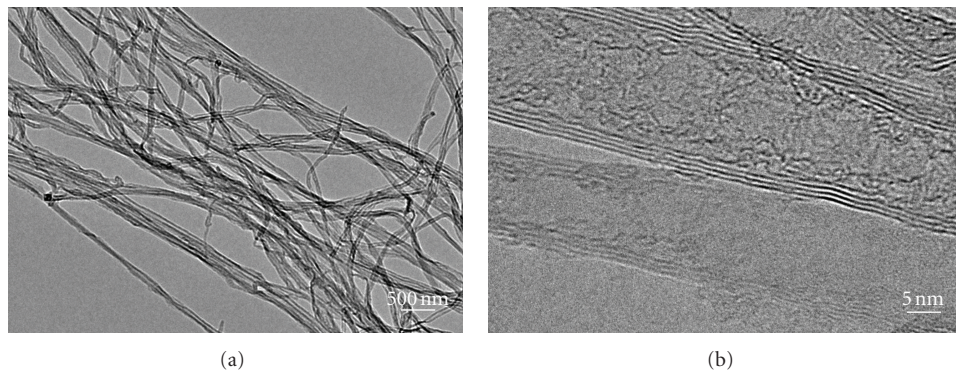


FIGURE 3: (a) Transmission electron microscopy (TEM) image of the typical CNTs. (b) High-resolution TEM image of the CNTs.

in Figure 1(b), which indicates high-quality aligned CNTs without any defect. Figure 1(c) shows that the height of aligned CNTs is up to 4 mm.

Figure 2(a) compares the side views of the CNT arrays synthesized with different growth times of 10, 30, 60, 120, and 180 min. The CNTs are highly aligned with each other in the above arrays. The plot of variation of growth rate with time for 5 h deposition is shown in Figure 2(b). The average growth rate is ca. 0.54 μm/s in the first 3 hours. In the case of the aligned CNTs grown from a 1.0 nm thick Fe layer, the growth rate of CNTs was found to not vary for long time. The plot indicates gradual slow decrease in the growth rate of CNTs in the first 3 hours. The growth rate is directly related to the catalyst activity during deposition. The balance between the rate of amorphous carbon deposition on the catalyst surface and removal of that amorphous carbon layer by hydrogen is the factor keeping the catalyst active for a long time. However, with increasing time the rate of amorphous carbon deposition increases compared to the rate of removal, which results in the decrease in the catalyst activity; the growth rate decreases followed by saturation, and finally the growth terminates due to the termination of catalyst activity. Figures 3(a) and 3(b), respectively, show the transmission electron microscopy (TEM) and high-resolution TEM images of individual CNTs grown for 180 min. The outer diameters of CNTs are around

12 nm, and the inner diameters are about 9 nm. The CNTs synthesized by this approach are all multi-walled with the interlamellar distance of 0.34 nm.

The CNT arrays had been further investigated by Raman spectroscopy. The intensity ratios of *D*-band to *G*-band intensity ratio may reflect the structure integrity of the CNTs in the clean arrays. Figure 4(a) shows typical Raman spectra of the top surfaces in the CNTs arrays synthesized with the growth times of 10, 60, and 180 min. The *D*-band and *G*-band are located at about 1337 cm⁻¹ and 1571 cm⁻¹, respectively. Figure 4(b) carefully compares the *I_D/I_G* values from the top of the CNTs arrays. It was found that the *I_D/I_G* values remain almost unchanged with the increasing growth times for both cases. In other words, the synthesized CNTs show high structure integrity.

The growth mechanism of long CNT arrays had been previously investigated by several groups [28, 29]. For instance, Peng et al. [28] found that the catalyst played a critical role in the structure and size of the resulting CNTs during a chemical vapor deposition process. A tiny variation in the catalyst composition produced the so-called pearl-like CNT which was very important to the spinnability of the CNT array. In this work, we also believe that the high-performance catalyst should be responsive for the high-quality CNT array without the assistance of water. It was found that uniform nanoparticles could be produced upon

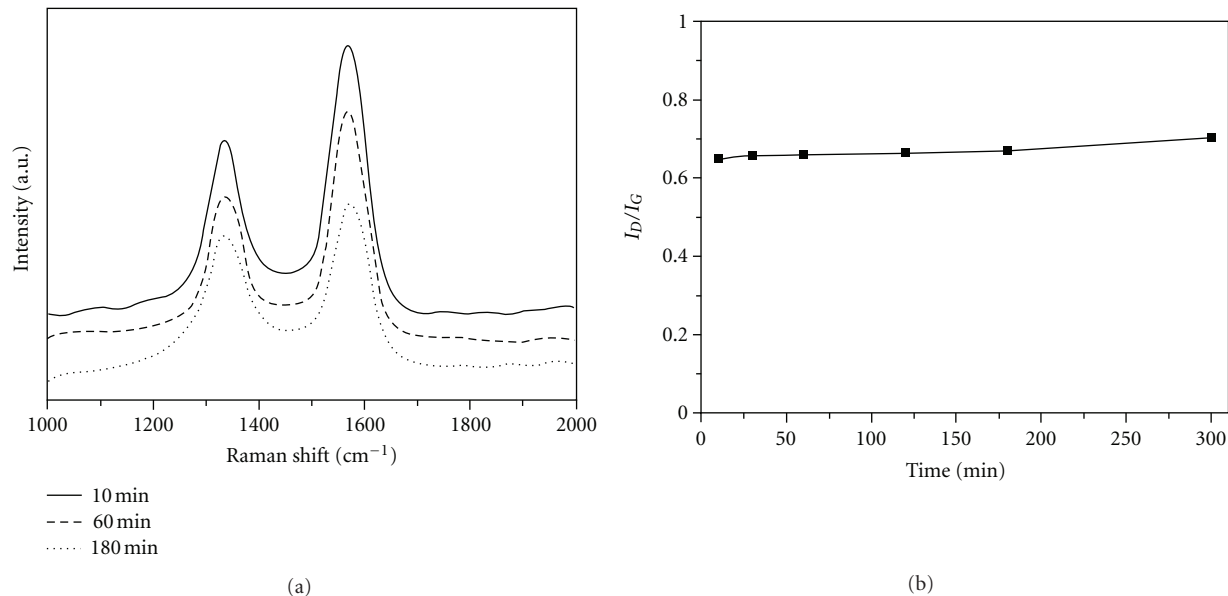


FIGURE 4: (a) Raman spectra of the CNT arrays grown for 10 min, 60 min, and 180 min. (b) Dependence of the I_D/I_G on the growth time from the top of the CNT arrays. Here I_D and I_G correspond to the peak intensities of D-band and G-band, respectively.

heating treatment of the catalyst in mimicking the synthetic condition. More efforts are underway.

4. Conclusions

In summary, we have developed a catalyst structure consisting of a thin Fe film on a dense Al_2O_3 buffer layer that was deposited on a Si substrate by e-beam evaporation. This catalyst lifetime was prolonged (>120 min), resulting in growth of CNT arrays that are 4 mm long. These CNT lengths are much longer than those reported previously. Increasing fraction of hydrogen was found to reduce the formation of amorphous carbon and to extend the catalyst life. Our synthesis of long CNT arrays requires a very low fraction of ethylene and large fraction of hydrogen.

Acknowledgments

The authors thank L. Li, X. Sun, and L. Qiu for suggestive discussions. This work was supported by the National Natural Science Foundation of China (Grant no. 11174372).

References

- [1] L. Zhu, D. W. Hess, and C. P. Wong, "Monitoring carbon nanotube growth by formation of nanotube stacks and investigation of the diffusion-controlled kinetics," *Journal of Physical Chemistry B*, vol. 110, no. 11, pp. 5445–5449, 2006.
- [2] H. Peng, Y. Zhu, D. E. Peterson, and Y. Lu, "Nanolayered carbon/silica superstructures via organosilane assembly," *Advanced Materials*, vol. 20, no. 6, pp. 1199–1204, 2008.
- [3] H. Peng, D. Chen, J. Y. Huang et al., "Strong and ductile colossal carbon tubes with walls of rectangular macropores," *Physical Review Letters*, vol. 101, no. 14, Article ID 145501, 2008.
- [4] H. Peng and X. Sun, "Macroporous carbon nanotube arrays with tunable pore sizes and their template applications," *Chemical Communications*, no. 9, pp. 1058–1060, 2009.
- [5] H. Peng and X. Sun, "Highly aligned carbon nanotube/polymer composites with much improved electrical conductivities," *Chemical Physics Letters*, vol. 471, no. 1–3, pp. 103–105, 2009.
- [6] L. Li, Z. Yang, H. Gao et al., "Vertically aligned and penetrated carbon nanotube/polymer composite film and promising electronic applications," *Advanced Materials*, vol. 23, no. 32, pp. 3730–3735, 2011.
- [7] S. Huang, L. Li, Z. Yang et al., "A new and general fabrication of aligned carbon nanotube/polymer film for electrode application," *Advanced Materials*, vol. 23, no. 40, pp. 4707–4710, 2011.
- [8] H. Peng, X. Sun, F. Cai et al., "Electrochromatic carbon nanotube/polydiacetylene nanocomposite fibres," *Nature Nanotechnology*, vol. 4, no. 11, pp. 738–741, 2009.
- [9] H. Peng, M. Jain, D. E. Peterson, Y. Zhu, and Q. Jia, "Composite carbon nanotube/silica fibers with improved mechanical strengths and electrical conductivities," *Small*, vol. 4, no. 11, pp. 1964–1967, 2008.
- [10] X. Sun, T. Chen, S. Huang, L. Li, and H. Peng, "Chromatic polydiacetylene with novel sensitivity," *Chemical Society Reviews*, vol. 39, no. 11, pp. 4244–4257, 2010.
- [11] H. Peng, "Aligned carbon nanotube/polymer composite films with robust flexibility, high transparency, and excellent conductivity," *Journal of the American Chemical Society*, vol. 130, no. 1, pp. 42–43, 2008.
- [12] T. Chen, S. Wang, Z. Yang et al., "Flexible, light-weight, ultra-strong, and semiconductive carbon nanotube fiber for highly efficient novel solar cell," *Angewandte Chemie International Edition*, vol. 50, no. 8, pp. 1815–1819, 2011.
- [13] M. Zhang, S. Fang, A. A. Zakhidov et al., "Materials science: strong, transparent, multifunctional, carbon nanotube sheets," *Science*, vol. 309, no. 5738, pp. 1215–1219, 2005.

- [14] R. H. Baughman, A. A. Zakhidov, and W. A. De Heer, "Carbon nanotubes—the route toward applications," *Science*, vol. 297, no. 5582, pp. 787–792, 2002.
- [15] T. W. Odom, J. L. Huang, P. Kim, and C. M. Lieber, "Atomic structure and electronic properties of single-walled carbon nanotubes," *Nature*, vol. 391, no. 6662, pp. 62–64, 1998.
- [16] J. W. G. Wildöer, L. C. Venema, A. G. Rinzler, R. E. Smalley, and C. Dekker, "Electronic structure of atomically resolved carbon nanotubes," *Nature*, vol. 391, no. 6662, pp. 59–62, 1998.
- [17] H. Nishijima, S. Kamo, S. Akita et al., "Carbon-nanotube tips for scanning probe microscopy: preparation by a controlled process and observation of deoxyribonucleic acid," *Applied Physics Letters*, vol. 74, no. 26, pp. 4061–4063, 1999.
- [18] S. Akita, Y. Nakayama, S. Mizooka et al., "Nanotweezers consisting of carbon nanotubes operating in an atomic force microscope," *Applied Physics Letters*, vol. 79, no. 11, pp. 1691–1693, 2001.
- [19] H. Tanaka, S. Akita, L. Pan, and Y. Nakayama, "Daisylike field-emission images from standalone open-ended carbon nanotube," *Japanese Journal of Applied Physics, Part 2*, vol. 43, no. 2, pp. L197–L199, 2004.
- [20] T. Chen, Z. Cai, Z. Yang et al., "Nitrogen-doped carbon nanotube composite fiber with a core-sheath structure for novel electrode," *Advanced Materials*, vol. 23, no. 40, pp. 4620–4625, 2011.
- [21] O. Suekane, A. Nagataki, and Y. Nakayama, "Current-induced curing of defective carbon nanotubes," *Applied Physics Letters*, vol. 89, no. 18, Article ID 183110, 2006.
- [22] J. Suhr, N. Koratkar, P. Keblinski, and P. Ajayan, "Viscoelasticity in carbon nanotube composites," *Nature Materials*, vol. 4, no. 2, pp. 134–137, 2005.
- [23] B. J. Hinds, N. Chopra, T. Rantell, R. Andrews, V. Gavalas, and L. G. Bachas, "Aligned multiwalled carbon nanotube membranes," *Science*, vol. 303, no. 5654, pp. 62–65, 2004.
- [24] Y. L. Li, I. A. Kinloch, and A. H. Windle, "Direct spinning of carbon nanotube fibers from chemical vapor deposition synthesis," *Science*, vol. 304, no. 5668, pp. 276–278, 2004.
- [25] X. Zhang, K. Jiang, C. Feng et al., "Spinning and processing continuous yarns from 4-inch wafer scale super-aligned carbon nanotube arrays," *Advanced Materials*, vol. 18, no. 12, pp. 1505–1510, 2006.
- [26] Z. Yang, X. Sun, X. Chen et al., "Structure and property dependence of carbon nanotube fiber on heating treatment," *Journal of Materials Chemistry*, vol. 21, no. 36, pp. 13772–13775, 2011.
- [27] M. Zhang, K. R. Atkinson, and R. H. Baughman, "Multi-functional carbon nanotube yarns by downsizing an ancient technology," *Science*, vol. 306, no. 5700, pp. 1358–1361, 2004.
- [28] H. Peng, M. Jain, Q. Li, D. E. Peterson, Y. Zhu, and Q. Jia, "Vertically aligned pearl-like carbon nanotube arrays for fiber spinning," *Journal of the American Chemical Society*, vol. 130, no. 4, pp. 1130–1131, 2008.
- [29] Q. Li, Y. Li, X. Zhang et al., "Structure-dependent electrical properties of carbon nanotube fibers," *Advanced Materials*, vol. 19, no. 20, pp. 3358–3363, 2007.
- [30] K. Jiang, Q. Li, and S. Fan, "Spinning continuous carbon nanotube yarns," *Nature*, vol. 419, no. 6909, p. 801, 2002.
- [31] H. M. Christen, A. A. Puretzky, H. Cui et al., "Rapid growth of long, vertically aligned carbon nanotubes through efficient catalyst optimization using metal film gradients," *Nano Letters*, vol. 4, no. 10, pp. 1939–1942, 2004.
- [32] W. Z. Li, S. S. Xie, L. X. Qian et al., "Large-scale synthesis of aligned carbon nanotubes," *Science*, vol. 274, no. 5293, pp. 1701–1703, 1996.
- [33] G. Y. Xiong, D. Z. Wang, and Z. F. Ren, "Aligned millimeter-long carbon nanotube arrays grown on single crystal magnesia," *Carbon*, vol. 44, no. 5, pp. 969–973, 2006.
- [34] A. J. Hart and A. H. Slocum, "Rapid growth and flow-mediated nucleation of millimeter-scale aligned carbon nanotube structures from a thin-film catalyst," *Journal of Physical Chemistry B*, vol. 110, no. 16, pp. 8250–8257, 2006.
- [35] J. Liu, L. Yuan, X. Yang, A. Elbert, and A. T. Harris, "Synthesis of vertically aligned carbon nanotube arrays on polyhedral Fe/Al₂O₃ catalysts," *Chemical Communication*, vol. 47, no. 22, pp. 6434–6436, 2011.
- [36] C. Kocabas, M. Shim, and J. A. Rogers, "Spatially selective guided growth of high-coverage arrays and random networks of single-walled carbon nanotubes and their integration into electronic devices," *Journal of the American Chemical Society*, vol. 128, no. 14, pp. 4540–4541, 2006.
- [37] X. Chen, L. Li, X. Sun, H. G. Kia, and H. Peng, "A novel synthesis of graphene nanoscrolls with tunable dimension at a large scale," *Nanotechnology*, vol. 23, no. 5, p. 55603, 2012.
- [38] K. Hata, D. N. Futaba, K. Mizuno, T. Namai, M. Yumura, and S. Iijima, "Water-assisted highly efficient synthesis of impurity-free single-walled carbon nanotubes," *Science*, vol. 306, no. 5700, pp. 1362–1364, 2004.
- [39] W. Guo, C. Liu, X. Sun, Z. Yang, H.G. Kia, and H. Peng, "Aligned carbon nanotube/polymer composite fibers with improved mechanical strength and electrical conductivity," *Journal of Materials Chemistry*, vol. 22, no. 3, pp. 903–908, 2012.
- [40] Y. Y. Wei, G. Eres, V. I. Merkulov, and D. H. Lowndes, "Effect of catalyst film thickness on carbon nanotube growth by selective area chemical vapor deposition," *Applied Physics Letters*, vol. 78, no. 10, pp. 1394–1396, 2001.
- [41] H. Dai, A. G. Rinzler, P. Nikolaev, A. Thess, D. T. Colbert, and R. E. Smalley, "Single-wall nanotubes produced by metal-catalyzed disproportionation of carbon monoxide," *Chemical Physics Letters*, vol. 260, no. 3-4, pp. 471–475, 1996.

Research Article

Controlled Synthesis of Manganese Dioxide Nanostructures via a Facile Hydrothermal Route

Suh Cem Pang, Suk Fun Chin, and Chian Ye Ling

Department of Chemistry, Faculty of Resource Science and Technology, Universiti Malaysia Sarawak, Sarawak, 94300 Kota Samarahan, Malaysia

Correspondence should be addressed to Suh Cem Pang, suhcem@gmail.com

Received 4 October 2011; Accepted 5 December 2011

Academic Editor: Arava Leela Mohana Reddy

Copyright © 2012 Suh Cem Pang et al. This is an open access article distributed under the Creative Commons Attribution License, which permits unrestricted use, distribution, and reproduction in any medium, provided the original work is properly cited.

Manganese dioxide nanostructures with controllable morphological structures and crystalline phases were synthesized via a facile hydrothermal route at low temperatures without using any templates or surfactants. Both the aging duration and aging temperatures were the main synthesis parameters used to influence and control the rate of morphological and structural evolution of MnO_2 nanostructures. MnO_2 nanostructures comprise of spherical nanoparticulate agglomerates and highly amorphous in nature were formed at lower temperature and/or short aging duration. In contrast, MnO_2 nanostructures of sea-urchin-like and nanorods-like morphologies and nanocrystalline in nature were prepared at the combined higher aging temperatures and longer aging durations. These nanostructures underwent notable phase transformation from $\delta\text{-MnO}_2$ to $\alpha\text{-MnO}_2$ upon prolonged hydrothermal aging duration and exhibited accelerated rate of phase transformation at higher aging temperature.

1. Introduction

One-dimensional manganese dioxide (MnO_2) nanostructures such as nanorods, nanowires, and nanofibers have generated intense research interests over the past recent years due to their superior optical, electrical, catalytic, magnetic and electrochemical properties [1–3]. Such manganese dioxide nanostructures are of considerable importance in technological applications and have been intensively investigated as promising electrode materials in primary/secondary batteries and electrochemical capacitors due to their excellent electrochemical properties, low-cost, environmentally benign, and ease of preparation [4–7]. Various approaches have been used to fabricate manganese dioxide, such as self-reacting microemulsion [8], precipitation [9], room-temperature solid reaction [10], sonochemical [11], and hydrothermal methods [12]. The hydrothermal method is a powerful synthesis approach for synthesizing various forms of manganese oxides and affords various advantageous features including the use of mild synthesis conditions such as pH and temperature, and a wide range of precursors that can be used.

Various types of inorganic nanowires and nanorods have been synthesized with the aid of templates or catalysts. Templates are being used to confine the growth of crystals,

while catalysts may act as energetically favorable sites for the adsorption of reactant molecules [13]. However, the introduction of templates or catalysts to a reaction system is often accompanied by drawbacks such as the need to prepare or select appropriate templates or catalysts. Besides, impurities in the final product may be difficult to be removed, thereby making the overall synthesis process more complicated and costly. As such, any synthetic method without the need to use any catalyst or template is more favorable for the preparation of low-dimensional nanostructures. Recently, a hydrothermal or solvothermal method has been employed to prepare one-dimensional nanoscaled materials, for example, $\alpha\text{-MnO}_2$, without the use of templates or catalysts [14]. This method is superior to traditional methods since no specific and expensive equipment is required for synthesizing nanostructured materials at low temperatures. The hydrothermal preparation of manganese dioxides involved mainly redox reactions of MnO_4^- and/or Mn^{2+} or the phase transformation of granular manganese dioxide precursors [15]. A common approach for the synthesis of single-crystalline $\alpha\text{-MnO}_2$ nanorods was based on the hydrothermal reaction of MnSO_4 and KMnO_4 [16]. DeGuzman et al. prepared fibrous $\alpha\text{-MnO}_2$ through redox reactions between KMnO_4 and MnSO_4 .

[17]. However, some minor differences in the morphology of final products have been observed as specific reaction conditions were being altered slightly. Parameters such as temperature, time and capping molecules can influence the growth of nanocrystals under nonequilibrium kinetic growth conditions in the solution-based approach [18]. Henceforth, the controlled synthesis of manganese dioxide nanostructures with favorable surface morphology, phase structure, crystallinity, and high reproducibility remains a considerable challenge.

This paper reports the controlled synthesis of various MnO_2 nanostructures via a facile and mild hydrothermal route without using any physical template and addition of any surfactant. Both $\delta\text{-MnO}_2$ and $\alpha\text{-MnO}_2$ nanostructures were synthesized based on the hydrothermal reaction of MnSO_4 and KMnO_4 in aqueous medium and at mild temperatures. Effects of hydrothermal synthesis conditions on the evolution of structural morphology and phase transformation of MnO_2 nanostructures were investigated.

2. Materials and Methods

2.1. Synthesis of MnO_2 Nanostructures. The synthesis of MnO_2 nanoparticles was based on the method reported by Xiao et al. with some modifications [19]. MnO_2 nanoparticles were synthesized by mixing aqueous solutions of KMnO_4 and MnSO_4 at ambient temperature and pressure, and the pH of solution mixture was adjusted to ~ 1 with concentrated HNO_3 . The aging temperatures were fixed at 25°C and 80°C , whereas the aging duration varied between 1 hour and 24 hours. The reaction product was collected by filtration, washed, and then air-dried at room temperature.

2.2. Characterization of MnO_2 Nanostructures. The surface and structural morphologies of MnO_2 samples were studied by scanning electron microscope (SEM) (JEOL Model JSM 6390LA) and transmission electron microscope (TEM) (JEOL Model JEM-1230). For SEM imaging, all MnO_2 samples were pre-coated with a thin platinum layer using an Ion Sputtering Device (JFC-1100 E) in order to reduce the inherent charging effect. As for TEM imaging, MnO_2 samples were first being dispersed well in ultrapure water by ultrasonication. $1\ \mu\text{L}$ of the resulting dispersions were then drop-coated onto Formvar-covered copper grids and air-dried. The specific surface area and pore size distribution of MnO_2 samples were determined using the nitrogen adsorption-desorption (BET) analyzer (Micrometrics ASAP 2010) at 77 K . The phases of MnO_2 samples synthesized at different aging durations and temperatures were studied using a X-ray diffractometer (XRD) (Scintag) with $\text{Cu K}\alpha$ radiation source.

3. Results and Discussion

A facile and mild hydrothermal route was being used to synthesize MnO_2 nanostructures without the use of any template or surfactant. Figures 1 and 2 show SEM micrographs of MnO_2 samples after being aged for various durations

at temperatures of 25°C and 80°C , respectively. Both the aging duration and aging temperature were observed to have substantial effect on the shape and morphology of MnO_2 nanostructures formed. At an aging temperature of 25°C , spherical agglomerates of MnO_2 nanoparticles were obtained at aging durations of between 0 hour and about 4 hours (Figure 1). In absence of surfactant, MnO_2 nanoparticles showed high tendency to aggregate and formed spherical agglomerates of various sizes [20]. However, upon prolonged aging for 8 hours, nanorod-like structures began to develop on surfaces of individual MnO_2 nanoparticles. Upon aging for more than 24 hours, well-defined nanorods had developed around these spherical MnO_2 nanoparticles to form sea-urchin-like MnO_2 nanostructures.

As shown in Figure 2, MnO_2 samples synthesized initially at 80°C comprised of mainly spherical agglomerates. However, such spherical agglomerates were no longer discernible but large aggregates of nanorod-like structures were observed upon being aged for 4 hours at 80°C . Well-defined and fully developed MnO_2 nanorods were formed after being aged for extended durations of 8 and 24 hours at 80°C , respectively. The aging temperature was found to play a crucial role in accelerating the rate of evolution of MnO_2 nanostructures from spherical agglomerates to aggregates of well-defined nanorods. On the contrary, no MnO_2 nanostructure was formed at the aging temperature of below 20°C even after being aged for a week. At the aging temperature of 25°C , the rate of structural evolution was observed to be rather slow, with MnO_2 nanostructures of sea-urchin-like shape formed only after being aged for 24 hours (Figure 1). However, at the elevated aging temperature of 80°C , distinctive and well-defined MnO_2 nanorod-like nanostructures were clearly discernable after being aged for 4 or more hours (Figure 2). A higher aging temperature appeared to favor the growth of one-dimensional (1D) MnO_2 nanostructures which could be attributed to the accelerated rate of decomposition of MnSO_4 to form MnO_2 at elevated temperatures. These nanorod-like nanostructures continued to grow in length due to their anisotropic nature and eventually led to the formation of nanowires [21]. Henceforth, hydrothermal synthesis conditions could be controlled and optimized was for the synthesis of MnO_2 nanostructures of desired morphology and crystalline phase.

Figure 3 shows TEM micrographs of MnO_2 nanoparticles synthesized at various aging durations at aging temperatures of 25°C . The evolution of nanorod-like nanostructures was observed to have initiated from the surfaces of MnO_2 nanoparticles after being aged for 4 hours at 25°C . More distinctive and defined nanorod-like nanostructures had evolved from spherical MnO_2 nanoparticles after being aged for 8 hours. Long and well-defined nanorods were observed to have developed on MnO_2 nanoparticles forming sea-urchin-like nanostructures after being aged for 24 hours at 25°C .

As shown in Figure 4, TEM micrographs depicted the rapid evolution of well-defined nanorods from individual spherical MnO_2 nanoparticles at elevated aging temperature of 80°C . Agglomerates of MnO_2 nanoparticles were observed to have transformed rapidly into sea-urchin-like

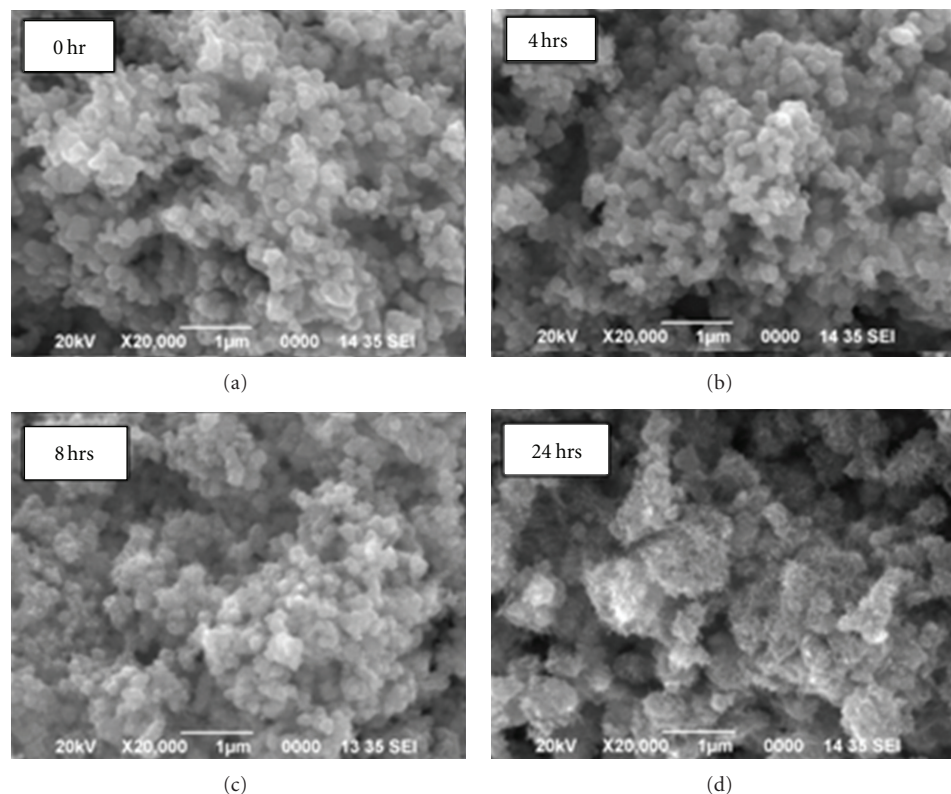


FIGURE 1: SEM micrographs of MnO₂ samples synthesized at various aging durations at 25°C.

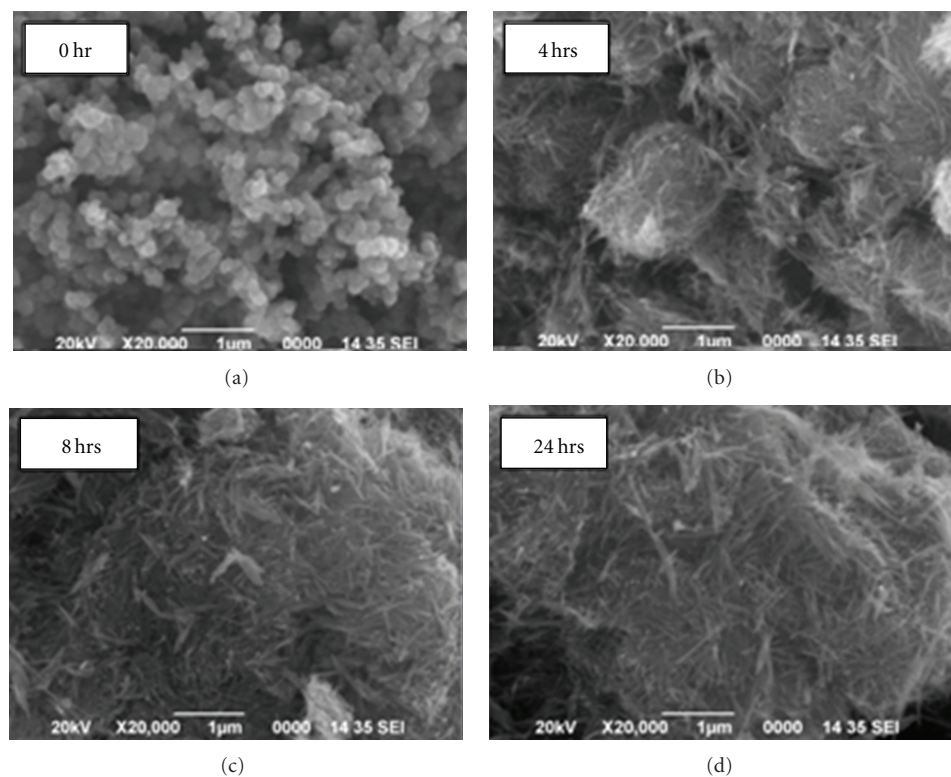


FIGURE 2: SEM micrographs of MnO₂ samples synthesized at various aging durations at 80°C.

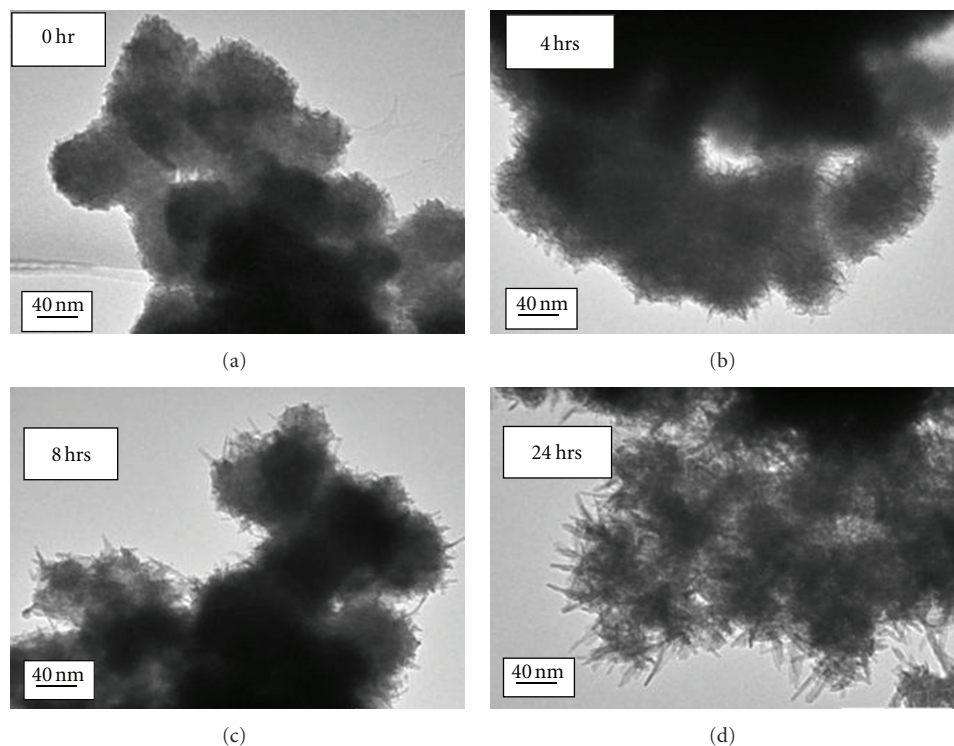


FIGURE 3: TEM micrographs of MnO_2 samples synthesized at various aging durations at 25°C .

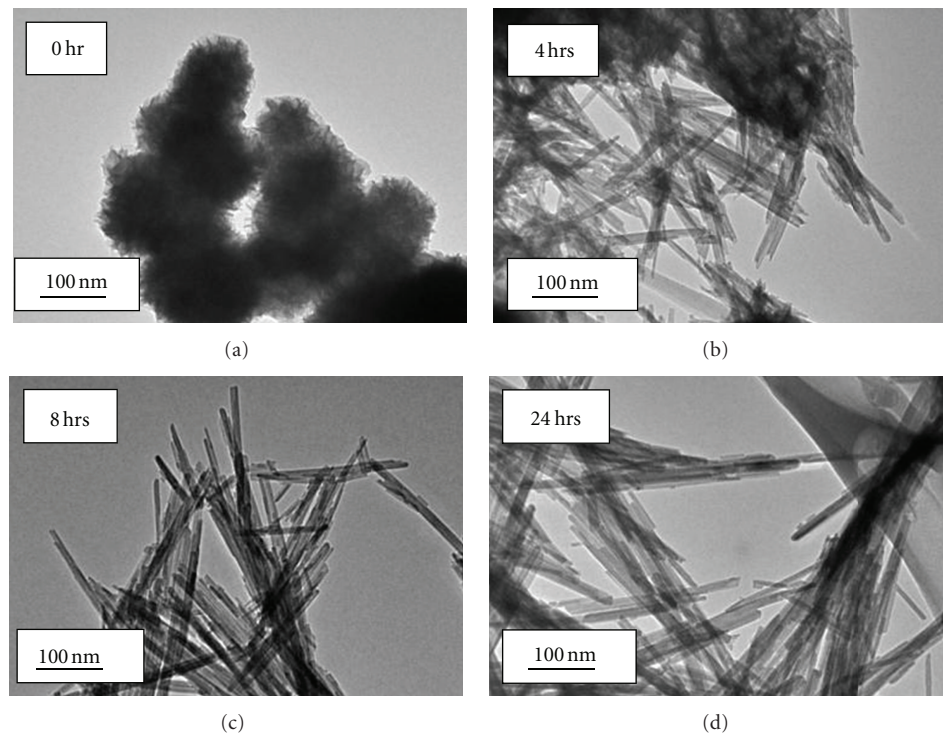


FIGURE 4: TEM micrographs of MnO_2 samples synthesized at various aging durations at 80°C .

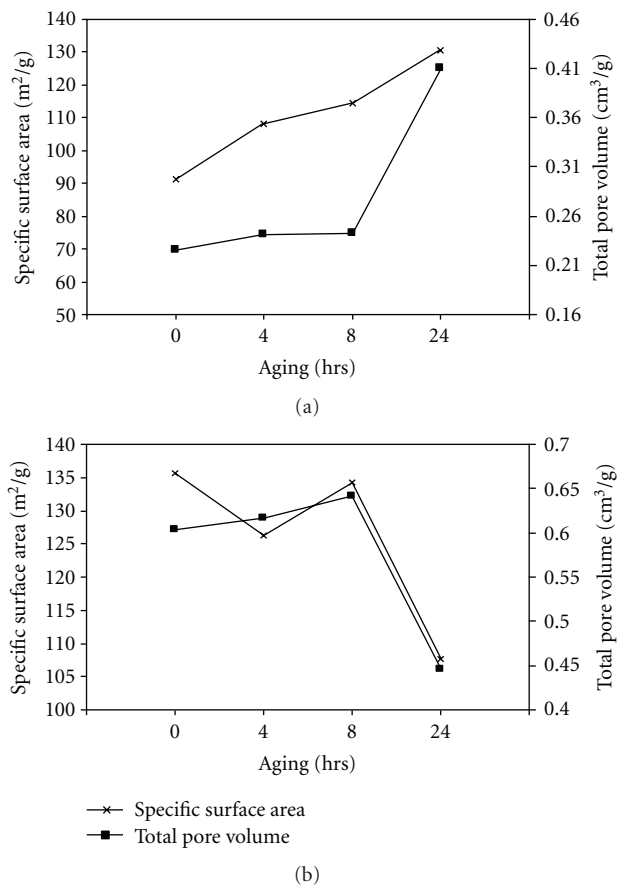


FIGURE 5: Effect of aging duration on the specific surface area and the total pore volume of MnO_2 samples synthesized at (a) 25°C and (b) 80°C.

nanostructures after being aged for 4 hours at 80°C. All MnO_2 nanoparticles were observed to have transformed completely into well-developed nanorods after being aged for 8 hours. No notable morphological changes of nanorods were observed after prolonged aging duration for up to 24 hours at 80°C. The diameter and length of well-defined MnO_2 nanorods ranged from 20 to 30 nm and 300 to 400 nm, respectively.

The hydrothermal synthesis route used in the present study had been shown to be a facile and mild synthesis approach for the synthesis of manganese dioxide nanostructures of desired morphology through judicious control of both the aging temperature and aging duration. In this synthesis approach, neither catalyst was needed to provide energetically favorable sites for the absorption of reactant molecules nor template was needed to direct the growth of nanorods. The driving force for the growth of MnO_2 nanorods during the synthesis process could be derived from the inherent crystal structure of MnO_2 material and its chemical potential in solution [22]. Based on our experimental observations, the formation mechanisms of MnO_2 nanostructures could entail the following processes. MnO_2 nanoparticles were initially produced by the redox reaction between

MnSO_4 and KMnO_4 . These MnO_2 nanoparticles would subsequently aggregate to form spherical agglomerates due to their high surface energies. During prolonged aging duration, MnO_2 nanoparticles would gradually transform into nanorods under the specific aging conditions. The gradual transformation of MnO_2 nanoparticles into nanorods could be attributed to their one-dimensional growth and anisotropic nature. Such processes obey the well-known “Ostwald Ripening” process, in which larger nanorods grow at the expense smaller ones because of differences in their surface energies. Similar formation mechanism of MnO_2 nanorods had been reported by Tang et al. with single-crystalline $\alpha\text{-MnO}_2$ nanorods being successfully synthesized via a facile hydrothermal approach without any template and surfactant [23].

Figure 5 shows the effect of aging duration on the specific surface area and total pore volume of MnO_2 nanostructures synthesized at different aging temperatures of 25°C and 80°C. For MnO_2 samples synthesized at aging temperature of 25°C, both specific surface area and total pore volume were observed to increase with increasing aging durations. The specific surface area and total pore volume of MnO_2 samples increased from 91.1 m^2/g and 0.225 cm^3/g as prepared (or without aging) to 130.5 m^2/g and 0.410 cm^3/g , respectively, after being aged for 24 hours. Such increases could be attributed to microstructural changes associated with the gradual transformation of tightly packed nanoparticles into nanorod-like structures during aging. MnO_2 nanostructures of evolving nanorods should possess higher porosity as indicated by the increasing specific surface area and total pore volume with longer aging durations. In contrast, MnO_2 samples synthesized at aging durations between 0 and 8 hours at 80°C showed substantially higher values of specific surface area and total pore volume which were comparable or even higher than MnO_2 samples synthesized after being aged for 24 hours at 25°C (Figure 5). However, there was a notable decrease in both specific surface area and total pore volume for samples synthesized after being aged for 24 hours (Figure 5(b)) which could be due to aggregation and realignment of fully developed nanorods. These results showed that a substantially higher rate of transformation from spherical nanoparticles to nanorods occurred at elevated aging temperature, with complete transformation being achieved within 1 hour of aging duration at 80°C as compared to more than 24 hours at 25°C.

Figure 6 shows X-ray diffractographs of MnO_2 samples as prepared and after being aged for 24 hours at 25°C and 80°C. Both types of as-prepared MnO_2 samples without any post synthesis aging showed similar broad diffraction peaks which can be indexed to $\delta\text{-MnO}_2$ phase albeit with low degree of crystallinity. The absence of other manganese dioxide diffraction peaks indicated the high purity of these as-prepared $\delta\text{-MnO}_2$ samples. $\delta\text{-MnO}_2$ samples synthesized at 25°C were observed to have only partially converted to $\alpha\text{-MnO}_2$ phase as indicated by the 211 peak but have remained mostly amorphous in nature after being aged for 24 hours (Figure 6(a)). In contrast, samples of highly crystalline $\alpha\text{-MnO}_2$ phase were obtained after being aged for 24 hours

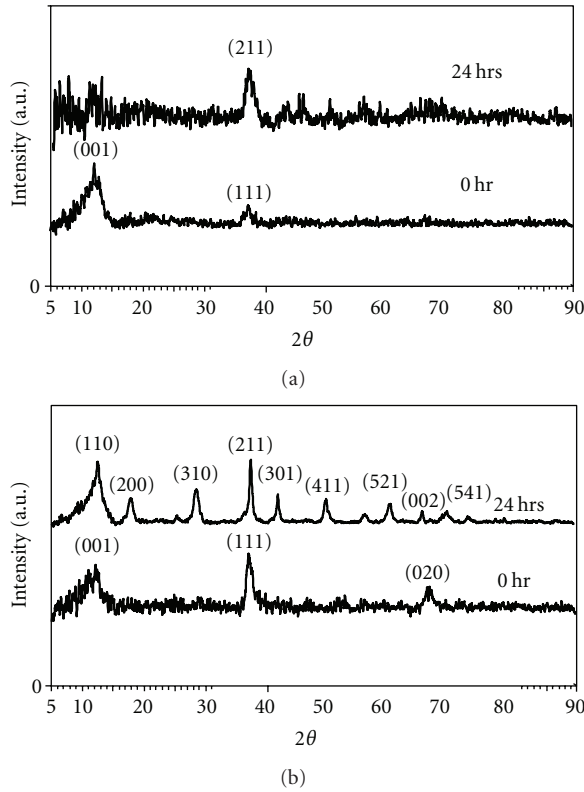


FIGURE 6: XRD diffractographs of MnO_2 samples synthesized at (a) 25°C and (b) 80°C with different aging duration.

at a higher aging temperature of 80°C . The presence of well-defined and sharp characteristic diffraction peaks of $\alpha\text{-MnO}_2$ phase showed a complete phase transformation of $\delta\text{-MnO}_2$ into $\alpha\text{-MnO}_2$ phase upon aging at 80°C for 24 hours (Figure 6(b)). Such phase transformation could be associated with the simultaneous morphological transformation from spherical nanoparticles to nanorods during prolonged aging at 80°C . These results indicated that the rates of phase and morphological transformation were temperature dependent, with accelerated rate occurred at elevated aging temperature. Our findings concurred with observations reported by other researchers that a higher aging temperature would promote more rapid phase transformation of MnO_2 samples [24, 25]. The phase transformation from $\delta\text{-MnO}_2$ to $\alpha\text{-MnO}_2$ could also be attributed to the stability of the polymorphs of MnO_2 . Since $\delta\text{-MnO}_2$ is less stable than $\alpha\text{-MnO}_2$ and $\beta\text{-MnO}_2$, it will be transformed into $\alpha\text{-MnO}_2$ or $\beta\text{-MnO}_2$ with increasing temperature [26]. However, due to the mild reaction conditions used in the present study, the $\beta\text{-MnO}_2$ phase could not be formed. These above results indicated that both the morphological structure and crystalline phase of MnO_2 samples could be modulated by varying the hydrothermal aging duration and temperatures.

4. Conclusion

In conclusion, MnO_2 nanostructures of spherical nanoparticulate agglomerates could be synthesized and transformed

into nanostructures of sea-urchin-like or agglomerates of nanorods by a facile and mild hydrothermal route without the use of any templates or catalyst. MnO_2 nanostructures underwent accelerated rate of transformation from $\delta\text{-MnO}_2$ to $\alpha\text{-MnO}_2$ phase and associated morphological changes from spherical nanoparticles to nanorods at elevated aging temperature. Both the morphological structure and crystalline phase of the MnO_2 nanostructures could therefore be modulated by varying the hydrothermal aging duration and temperatures.

Acknowledgment

This work was supported in part by the Universiti Malaysia Sarawak under the special fundamental Research Grant 01(K03)/557/2005(56).

References

- [1] V. Subramanian, H. Zhu, R. Vajtai, P. M. Ajayan, and B. Wei, "Hydrothermal synthesis and pseudocapacitance properties of MnO_2 nanostructures," *Journal of Physical Chemistry B*, vol. 109, no. 43, pp. 20207–20214, 2005.
- [2] S. F. Chin, S. C. Pang, and M. A. Anderson, "Self-assembled manganese dioxide nanowires as electrode materials for electrochemical capacitors," *Materials Letters*, vol. 64, no. 24, pp. 2670–2672, 2010.
- [3] Y. S. Ding, X. F. Shen, S. Gomez, H. Luo, M. Aindow, and S. L. Suib, "Hydrothermal growth of manganese dioxide into three-dimensional hierarchical nanoarchitectures," *Advanced Functional Materials*, vol. 16, no. 4, pp. 549–555, 2006.
- [4] S. C. Pang and M. A. Anderson, "Novel electrode materials for electrochemical capacitors: Part II. Material characterization of sol-gel-derived and electrodeposited manganese dioxide thin films," *Journal of Materials Research*, vol. 15, no. 10, pp. 2096–2106, 2000.
- [5] S. C. Pang, M. A. Anderson, and T. W. Chapman, "Novel electrode materials for thin-film ultracapacitors: comparison of electrochemical properties of sol-gel-derived and electrodeposited manganese dioxide," *Journal of the Electrochemical Society*, vol. 147, no. 2, pp. 444–450, 2000.
- [6] S. F. Chin, S. C. Pang, and M. A. Anderson, "Material and electrochemical characterization of tetrapropylammonium manganese oxide thin films as novel electrode materials for electrochemical capacitors," *Journal of the Electrochemical Society*, vol. 149, no. 4, pp. A379–A384, 2002.
- [7] S. F. Chin and S. C. Pang, "Tetrapropylammonium-manganese oxide/polypyrrole hybrid nanocomposite thin films as novel electrode materials for supercapacitors," *Materials Chemistry and Physics*, vol. 124, no. 1, pp. 29–32, 2010.
- [8] C. Xu, B. Li, H. Du, F. Kang, and Y. Zeng, "Electrochemical properties of nanosized hydrous manganese dioxide synthesized by a self-reacting microemulsion method," *Journal of Power Sources*, vol. 180, no. 1, pp. 664–670, 2008.
- [9] V. Subramanian, H. Zhu, and B. Wei, "Alcohol-assisted room temperature synthesis of different nanostructured manganese oxides and their pseudocapacitance properties in neutral electrolyte," *Chemical Physics Letters*, vol. 453, no. 4–6, pp. 242–249, 2008.
- [10] A. Yuan, X. Wang, Y. Wang, and J. Hu, "Textural and capacitive characteristics of MnO_2 nanocrystals derived from a novel

- solid-reaction route," *Electrochimica Acta*, vol. 54, no. 3, pp. 1021–1026, 2009.
- [11] A. Zolfaghari, F. Ataherian, M. Ghaemi, and A. Gholami, "Capacitive behavior of nanostructured MnO₂ prepared by sonochemistry method," *Electrochimica Acta*, vol. 52, no. 8, pp. 2806–2814, 2007.
- [12] D. Yan, P. Yan, S. Cheng et al., "Fabrication, in-depth characterization, and formation mechanism of crystalline porous birnessite MnO₂ film with amorphous bottom layers by hydrothermal method," *Crystal Growth and Design*, vol. 9, no. 1, pp. 218–222, 2009.
- [13] L. Zhang, Z. H. Liu, X. Tang, J. Wang, and K. Ooi, "Synthesis and characterization of β -MnO₂ single crystals with novel tetragonal morphology," *Materials Research Bulletin*, vol. 42, no. 8, pp. 1432–1439, 2007.
- [14] X. Wang and Y. Li, "Rational synthesis of α -MnO₂ single-crystal nanorods," *Chemical Communications*, no. 7, pp. 764–765, 2002.
- [15] X. Zhang, W. Yang, J. Yang, and D. G. Evans, "Synthesis and characterization of α -MnO₂ nanowires: self-assembly and phase transformation to β -MnO₂ microcrystals," *Journal of Crystal Growth*, vol. 310, no. 3, pp. 716–722, 2008.
- [16] X. Wang and Y. Li, "Synthesis and formation mechanism of manganese dioxide nanowires/nanorods," *Chemistry—A European Journal*, vol. 9, no. 1, pp. 300–306, 2003.
- [17] R. N. DeGuzman, Y. F. Shen, E. J. Neth et al., "Synthesis and characterization of Octahedral Molecular Sieves (OMS-2) having the hollandite structure," *Chemistry of Materials*, vol. 6, no. 6, pp. 815–821, 1994.
- [18] J. Wu, H. Zhang, X. Ma et al., "Synthesis and characterization of single crystalline MnOOH and MnO₂ nanorods by means of the hydrothermal process assisted with CTAB," *Materials Letters*, vol. 60, no. 29–30, pp. 3895–3898, 2006.
- [19] T. D. Xiao, P. R. Strutt, M. Benaissa, H. Chen, and B. H. Kear, "Synthesis of high active-site density nanofibrous MnO₂-base materials with enhanced permeabilities," *Nanostructured Materials*, vol. 10, no. 6, pp. 1051–1061, 1998.
- [20] R. Jiang, T. Huang, J. Liu, J. Zhuang, and A. Yu, "A novel method to prepare nanostructured manganese dioxide and its electrochemical properties as a supercapacitor electrode," *Electrochimica Acta*, vol. 54, no. 11, pp. 3047–3052, 2009.
- [21] Y. Dong, H. Yang, K. He, S. Song, and A. Zhang, " β -MnO₂ nanowires: a novel ozonation catalyst for water treatment," *Applied Catalysis B: Environmental*, vol. 85, no. 3–4, pp. 155–161, 2009.
- [22] Z. Y. Yuan, Z. Zhang, G. Du, T. Z. Ren, and B. L. Su, "A simple method to synthesise single-crystalline manganese oxide nanowires," *Chemical Physics Letters*, vol. 378, no. 3–4, pp. 349–353, 2003.
- [23] N. Tang, X. Tian, C. Yang, Z. Pi, and Q. Han, "Facile synthesis of α -MnO₂ nanorods for high-performance alkaline batteries," *Journal of Physics and Chemistry of Solids*, vol. 71, no. 3, pp. 258–262, 2010.
- [24] X. Wang and Y. Li, "Synthesis and formation mechanism of manganese dioxide nanowires/nanorods," *Chemistry—A European Journal*, vol. 9, no. 1, pp. 300–306, 2003.
- [25] Y. Yang and C. Huang, "Effect of synthetical conditions, morphology, and crystallographic structure of MnO₂ on its electrochemical behavior," *Journal of Solid State Electrochemistry*, vol. 14, no. 7, pp. 1293–1301, 2010.
- [26] P. M. de Wolff, "Interpretation of some γ -MnO₂ diffraction patterns," *Acta Crystallographica*, vol. 12, pp. 341–345, 1959.

Research Article

Preparation and Characterization of Nano-Polyaniline Film on ITO Conductive Glass by Electrochemical Polymerization

Qi Qin^{1,2} and Yunxia Guo³

¹ School of Materials and Chemical Engineering, Zhongyuan University of Technology, 41 Zhongyuan Road, Zhengzhou 450007, China

² School of Materials Science and Engineering, Zhengzhou University, 100 Kexue Road, Zhengzhou 450001, China

³ College of Material Science and Technology, Nanjing University of Aeronautics and Astronautics, 29 Yuda Street, Nanjing 210016, China

Correspondence should be addressed to Qi Qin, qq821223@126.com

Received 16 October 2011; Accepted 10 December 2011

Academic Editor: Arava Leela Mohana Reddy

Copyright © 2012 Q. Qin and Y. Guo. This is an open access article distributed under the Creative Commons Attribution License, which permits unrestricted use, distribution, and reproduction in any medium, provided the original work is properly cited.

Polyaniline (PANI) films were synthesized on a conducting ITO glass by potentiostatic techniques to construct a low-cost counter electrode for dye-sensitized solar cell (DSSC). The compact layer, nanoparticles, nanorods- and fibrils were observed on the top of PANI films with different constant potentials by SEM. Then the conductivity test illuminated that a polyaniline film with the highest conductivity was electrodeposited at 1.0 V. Finally, the photoelectric measurement showed that the energy conversion efficiency of DSSC with the PANI electrode was increased with the potential decreasing. And the efficiency of DSSC with PANI counter electrode at 1.0 V was higher than that with Pt electrode, owing to the high surface area, high conductivity, and excellent catalytic activity of PANI electrode. Therefore, the PANI counter electrode with excellent catalytic performance is a potential substitute for platinized electrode to save cost of DSSC.

1. Introduction

Dye-sensitized solar cells have been one of the most promising photovoltaic devices due to their high conversion efficiency and low cost. In general, a DSSC comprises a dye-sensitized titanium dioxide (TiO_2) electrode, an iodide/triiodide redox electrolyte solution, and a counter electrode (CE). The function of the CE is to transfer electrons from the external circuit back to the redox electrolyte and to catalyze the reduction of the triiodide ion [1–4]. Usually, a Pt electrode formed on a transparent conductive glass substrate is used as the CE for DSSC. Although Pt exhibits excellent catalytic activity for triiodide reduction and good electric conductivity, it is extremely expensive and has the problem of reserves for large-scale application [5, 6]. Meanwhile, the shape limitation will bring transport problem for the Pt counter electrode. Future large solar electric conversion systems will prefer materials abundantly available and easily handled. Therefore, it is necessary to develop cheap materials for CEs which also exhibit high electrical conductivity, good

chemical stability, and good catalytic activity to the reduction of triiodide ion.

So far, inexpensive carbonaceous materials and conducting polymers such as graphite, carbon black, carbon nanotube, graphene, poly(3,4-propylenedioxythiophene) (PProDOT), and poly(3,4-ethylenedioxythiophene) (PEDOT) have been employed as the catalytic materials on indium tin oxide (ITO) glass for the CEs. Yen et al. reported a DSSC using the carbon nanotube composite plate had a cell efficiency of 4.73% [7]. Meanwhile, Saito et al. used chemically polymerized PEDOT on fluorine-doped tin oxide (FTO) glass as the counter electrodes and obtained a conversion efficiency of 3.6% under 100 mWcm^{-2} [8]. Fukuri and coworkers also developed PEDOT-based solid-state electrolytes, but the cell efficiencies were <1% [9].

Recently, the conducting PANI was applied as the counter electrode materials for DSSC to replace the platinized counter electrode due to its easy synthesis, high conductivity, and unique redox properties [10]. Among the previous research, the electrode with a layer of conductive PANI coated on

conducting glass is achieved by using several methods, such as the spreading of a solution of conductive polymer on the surface of the material followed by the evaporation of the solvent [11], the *in situ* chemical polymerization, and then deposition on the surfaces of various materials immersed in the polymerization solution [12] or the electropolymerization of the monomers on an electrode [13–16]. Wu et al. researched on using polyaniline [5] or polypyrrole [6] as counter electrode in DSSCs by the vertical dip-tugging method [17, 18]. Moreover, it was reported that PANI was deposited on the surface of ITO conductive glass by *in situ* chemical polymerization [19], and the energy conversion efficiency of DSSC with PANI counter electrode reached 2.64%. However, these methods were difficult to obtain a homogeneous and compact film owing to the insolubility or poor solubility of PANI in nearly all solvents [20].

Hence, the method of electropolymerization to prepare a compact film of polyaniline is considered in this study. The PANI counter electrodes are prepared on the surface of conducting glass by using potentiostatic techniques, and the photoelectric performances of DSSC with these electrodes are also discussed.

2. Experimental

2.1. Materials. Aniline (An, analytical grade from Sinopharm Chemical Reagent Co., Ltd) was purified by distillation under reduced pressure prior to usage. Analytical-grade reagents, H₂SO₄, iodine, lithium perchlorate, acetonitrile, ethanol, and acetone (Sinopharm Chemical Reagent Co., Ltd), were used without any pretreatment. All solutions were prepared from deionized water. ITO glasses from the Institute of Plasma Physics (CAS) were used as the substrates. Anhydrous lithium iodide, 4-*tert*-butylpyridine, 1-methyl-3-propylimidazolium iodide, methoxypipronitrile were provided by Fluka Chemical Corporation. TiO₂ colloid and dye N719 were the commercial product purchased from Solaronix SA (Switzerland). Pt counter electrode bought from Dyesol Limited was used in the contrast test.

2.2. Preparation of PANI Electrode. ITO glasses were rinsed with deionized water and immersed in ethanol ultrasonically for 15 min, then immersed in acetone ultrasonically for 15 min before PANI electropolymerization. One ITO glass sheet was used as working electrode for PANI deposition. The deposited area was 1 cm² with other area insulated by an adhesive tape coating. A Pt sheet was used as the counter electrode. PANI was electrodeposited on the surface of ITO glass by potentiostatic method at different constant potential (1.0 V, 1.1 V, 1.2 V, and 1.3 V) for 500 s in a 0.2 M aniline/0.5 M sulphuric acid (H₂SO₄) electrolyte solution. Finally, PANI-modified glass electrode was immersed in 0.5 M H₂SO₄ statically in order to expel aniline monomer and oligomer PANI from the polymeric film and then rinsed with deionized water and ethanol for several times and dried in a vacuum at 60°C for 24 h.

2.3. Assembling of DSSCs. Nano-TiO₂ colloid was dropped on the ITO glass plate by a doctor scraping technique to form

a porous film. Then the TiO₂ porous film was sintered by annealing at 450°C for 30 min. After cooling to 100°C, the TiO₂ film was immersed in an ethanol solution of N719 dye for 24 h. Finally, DSSC was assembled by injecting a drop of electrolyte with I₂, LiI, 1-methyl-3-propylimidazolium iodide, 4-*tert*-butylpyridine in methoxypipronitrile into the aperture between the TiO₂ porous film electrode and the PANI electrode.

2.4. Measurement and Characterization. The SEM image of the sample was performed using a scanning electron microscopy (LEO1550, GER). FTIR spectrum of the PANI was recorded in the range of 500–4000 cm⁻¹ using FTIR spectroscopy (Perkin Elmer 1760, USA). The conductivity of PANI was measured by manual four probe instrument (MP 1008, WENTWORTH, UK). Photocurrent-voltage characteristics of the DSSCs were obtained by a Keithley model 2400 digital source meter using an Oriel 91192 solar simulator equipped with AM 1.5 filter and intensity of 100 mW/cm². All the polymerization experiments were performed on an electrochemical workstation (CHI660A, CHInstrument, CHN).

3. Results and Discussion

3.1. Micromorphology of PANI. The photograph of the polyaniline films electrodeposited at 1.0, 1.1, 1.2, and 1.3 V on the ITO substrate is shown in Figure 1. It can be seen the emerald PANI thin layer is deposited on glass from Figure 1(a). With the electropolymerization potential rising, the thickness of PANI layer has a significant increase, and the color of PANI film becomes darker and darker. The PANI film electrodeposited at 1.3 V closes to dark green.

Figure 2 shows the SEM images of PANI electrodes at different constant potentials. At the low potential (1.0 V), PANI nuclei grow on the bare electrode to form a compact layer, which adhered to the electrode surface strongly. Increasing the potential to 1.1 V, some PANI particles with the diameter in range of 800 nm appear on the top of PANI nodules layer. As the potential shifts to more positive potential, the PANI particles disappear and the nanorods emerge on the surface of PANI film. At 1.2 V, PANI mainly forms the short nanorods with the length of 500 nm and with the diameter of 100 nm. At the higher potential, the PANI deposition shows an extensive fibril growth. At 1.3 V, PANI forms the long fibril with the length of 1 μm and with the diameter of 100 nm. This growth of PANI has no directional alignment, and the nanorods or fibrils are nonuniform. It is clearly demonstrated that the formation of thick, short nanorods is preferred at low polymerization potential while the development of thin, long fibrils is more easily achieved at higher potential.

3.2. Molecular Structure of PANI. Figure 3 shows the FTIR spectra of PANI deposited on conductive glass at different potentials. It is clear that the characteristic peaks of polyaniline (KBr, thin film, cm⁻¹) present near the wavenumbers of 1561 (C–C stretching mode for the quinoid ring), 1484 (benzenoid rings vibration), 1295 (C–N stretching mode),

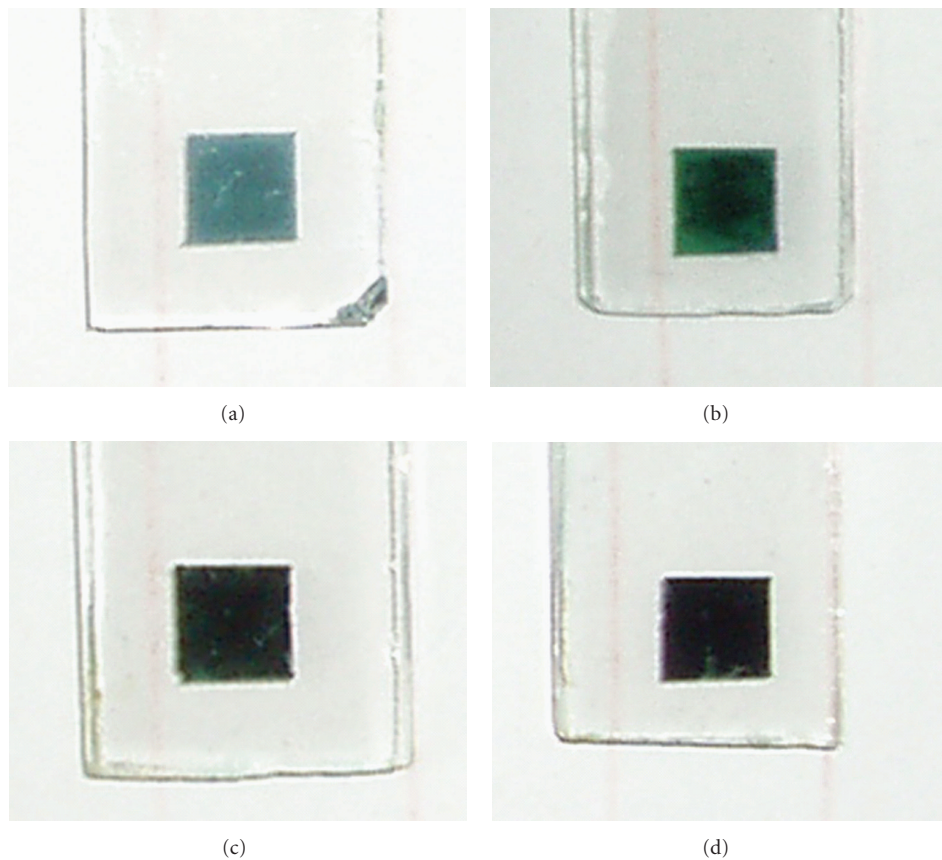


FIGURE 1: The photograph of PANI films electrodeposited at (a) 1.0, (b) 1.1, (c) 1.2, (d) 1.3 V.

1240 (C–N⁺ stretching vibration), 1077 (a vibration mode of the –NH⁺= structure), and 792 (out-of-plane bending vibration of C–H) cm⁻¹ [21–27]. As the potential reaches to 1.3 V, the characteristic peaks of PANI become stronger, and the band intensity significantly enhances with the gradual rise of constant potential. It indicates that the PANI can be formed by potentiostatic polymerization at 1.0 V, and the more PANI obtained with the potential increasing can make the peak intensity of PANI stronger.

3.3. Conductivity Measurement. The conductivity of PANI deposited at different potentials is measured by four-point probes instrument and then calculated by this equation:

$$\sigma = \frac{\ln 2}{\pi d} \cdot \frac{I_{12}}{U_{34}}, \quad (1)$$

where σ is the conductivity, d is the thickness of films, I_{12} is the current from 1 to 2 points, and U_{34} is the potential difference between 3 and 4 points. The schematic diagram of four-point probes method is shown in Figure 4.

Meanwhile, polymer thickness is estimated from the amount of charge Q_A according to the equation [28]:

$$d = \frac{Q_A M_w}{z F A \rho}, \quad (2)$$

where Q_A is the charge under the potentiostatic electrodeposition, M_w is molecular weight of aniline, $z = 0.5$ (number

of electrons/aniline unit), A is area of the electrode, ρ is specific density of aniline, and F is Faraday's constant. Table 1 presents the thickness and the conductivity of PANI layers at 1.0, 1.1, 1.2, and 1.3 V. It can be found that the film thickness of PANI increases with the polymerization potential increasing, but the conductivity of PANI decreases. As the potential is 1.0 V, the PANI film is very thin (about 33 nm). With the polymerization potential rising, the current density on the PANI/glass electrode is increased, leading to the thickness of PANI film increased also; however, the more thickness of PANI film results in the reduction of conductivity. The best conductivity of PANI deposited on conducting glass substrate reached to 62.59 S/cm when the polymerization potential was 1.0 V. Otherwise, the increase of current density on the PANI/glass electrode caused by the rise of potential leads to the peroxidation of PANI, and the conducting emeraldine form is converted into a nonconducting full-oxidation state. This transformation process among the different redox states of PANI also results in the reduction of conductivity.

3.4. Photoelectric Performance of PANI Electrode. The photoelectric properties of DSSCs with PANI/glass and Pt counter electrode are shown in Figure 5, and the results are also listed in Table 2. The result indicates that the PANI/glass electrode deposited at low potential (1.0 V) with the high conductivity and electrocatalytic activity can obtain the best

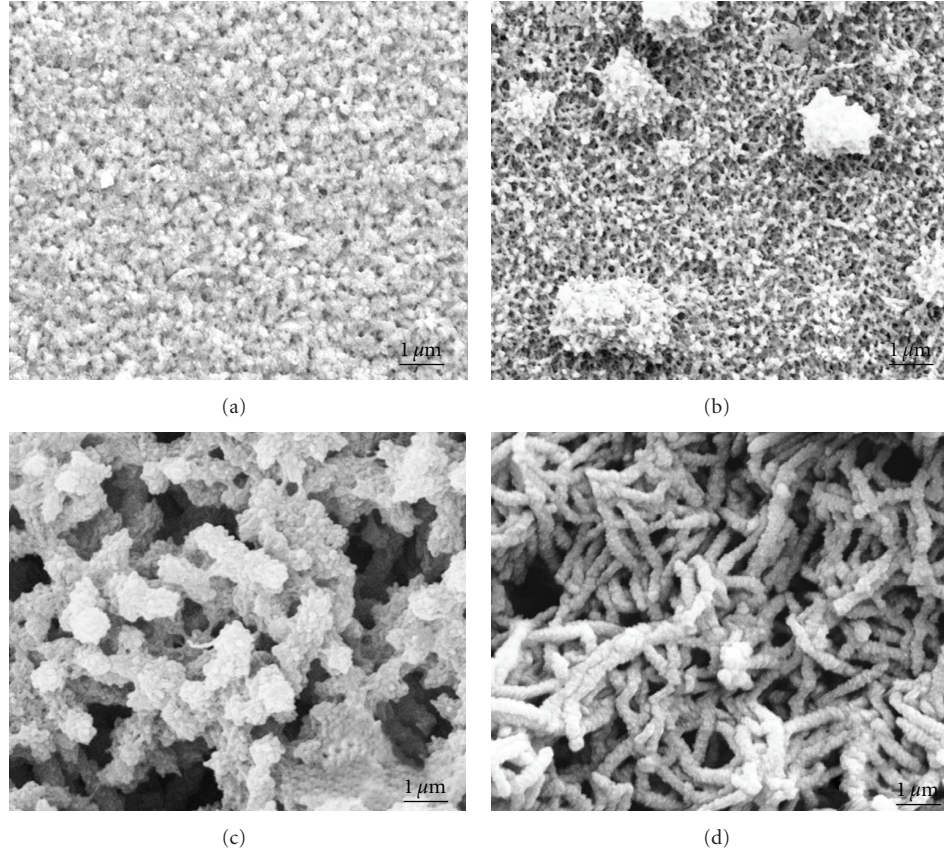


FIGURE 2: SEM images of polyaniline electrodeposited at (a) 1.0 V, (b) 1.1 V, (c) 1.2 V, (d) 1.3 V.

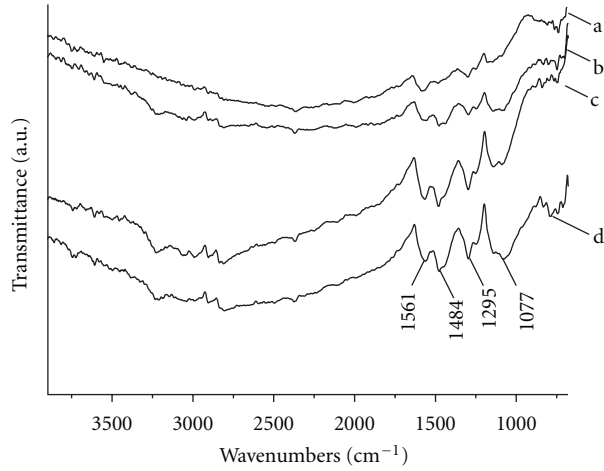


FIGURE 3: FTIR spectrum of PANI at (a) 1.0 V, (b) 1.1 V, (c) 1.2 V, (d) 1.3 V.

photoelectric conversion efficiency, which reaches to 5.68%. This photoelectric conversion efficiency of DSSC with PANI counter electrode is higher than that with Pt electrode (4.51%), and the fill factor (FF) is about 0.488, which is higher than Pt electrode (0.483). This improvement of the photoelectric efficiency is referred to the PANI electrode

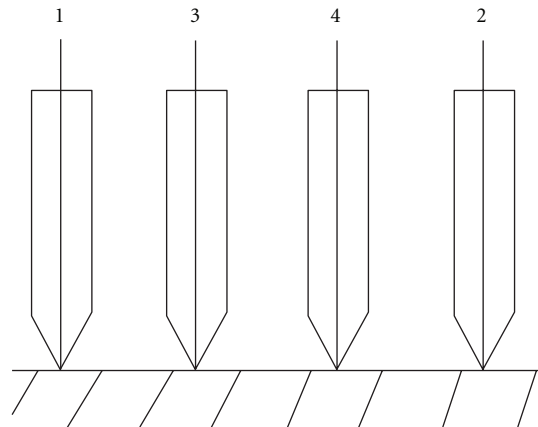


FIGURE 4: The schematic diagram of four-point probes method.

with the higher surface area, the higher electrocatalytic activity, and the lower charge-transfer resistance, compared to Pt electrode. Moreover, with the potential rising from 1.0 to 1.3 V, the FF has a little change, the J_{sc} of DSSC with PANI counter electrode has a remarkable decrease, and the energy conversion efficiency of DSSC with PANI electrode descends from 5.68% to 4.03%. It is due to the reduction of the conductivity and increase of the charge

TABLE 1: The thickness and conductivity of PANI films under different potential.

Sample	Thickness d [μm]	Conductivity σ [S/cm]
PANI-1.0 V	0.033	62.59
PANI-1.1 V	0.212	42.97
PANI-1.2 V	0.651	25.18
PANI-1.3 V	1.367	10.41

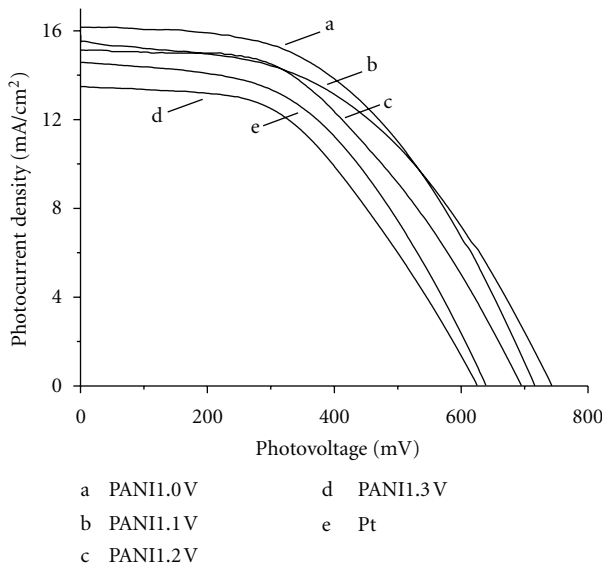


FIGURE 5: Photoelectric properties of DSSCs with different PANI and Pt counter electrodes.

TABLE 2: Photovoltaic performance of DSSCs with different PANI and Pt counter electrode.

Electrode	J_{SC} [mA/cm²]	V_{OC} [mV]	FF	Efficiency [%]
PANI-1.0 V	16.18	720	0.488	5.68
PANI-1.1 V	15.56	740	0.476	5.48
PANI-1.2 V	15.19	700	0.466	4.95
PANI-1.3 V	13.49	620	0.482	4.03
Pt	14.60	640	0.483	4.51

transmission impedance of PANI electrode with the polymerization potential increasing. As a result, the new PANI counter electrode prepared by electrochemical synthesis method has more predominant photoelectric performance than Pt electrode. Thus, the PANI counter electrode can replace the conventional Pt counter electrode for reducing the production cost of DSSC.

4. Summary

In summary, the PANI counter electrode was successfully fabricated on conducting ITO glass by electrochemical

polymerization method. The results showed that the compact layers, nanoparticles, nanorods, and fibrils of PANI successively grew on the surface of glass as the potential rising from 1.0 V to 1.3 V. The conductivity and photoelectric test indicated that the optimal constant potential of PANI electrodeposition is 1.0 V. The energy conversion efficiency of DSSC with PANI counter electrode at 1.0 V reached 5.68%, which was higher than Pt electrode. This improvement corresponds to higher conductivity, higher electrocatalytic activity, and smaller charge-transfer resistance of PANI electrode. Therefore, the PANI counter electrode with the simple preparation procedure, low fabrication cost, and excellent catalytic properties will be a credible alternative of the counter electrode from DSSCs in the future.

References

- [1] P. K. Singh, K. W. Kim, and H. W. Rhee, "Ionic liquid (1-Methyl 3-propyl imidazolium iodide) with polymer electrolyte for DSSC application," *Polymer Engineering and Science*, vol. 49, no. 5, pp. 862–865, 2009.
- [2] B. O'Regan and M. Grätzel, "A low-cost, high-efficiency solar cell based on dye-sensitized colloidal TiO_2 films," *Nature*, vol. 353, no. 6346, pp. 737–740, 1991.
- [3] M. Grätzel, "Dye-sensitized cells," *Journal of Photochemistry and Photobiology C*, vol. 4, pp. 145–153, 2003.
- [4] C.-W. Tu, K.-Y. Liu, A.-T. Chien et al., "Enhancement of photocurrent of polymer-gelled dye-sensitized solar cell by incorporation of exfoliated montmorillonite nanoplatelets," *Journal of Polymer Science, Part A*, vol. 46, no. 1, pp. 47–53, 2008.
- [5] Q. Li, J. Wu, Q. Tang et al., "Application of microporous polyaniline counter electrode for dye-sensitized solar cells," *Electrochemistry Communications*, vol. 10, no. 9, pp. 1299–1302, 2008.
- [6] J. Wu, Q. Li, L. Fan et al., "High-performance polypyrrole nanoparticles counter electrode for dye-sensitized solar cells," *Journal of Power Sources*, vol. 181, no. 1, pp. 172–176, 2008.
- [7] M. Y. Yen, C. Y. Yen, S. H. Liao et al., "A novel carbon-based nanocomposite plate as a counter electrode for dye-sensitized solar cells," *Composites Science and Technology*, vol. 69, no. 13, pp. 2193–2197, 2009.
- [8] Y. Saito, W. Kubo, T. Kitamura, Y. Wada, and S. Yanagida, "I-/I₃- redox reaction behavior on poly (3,4-ethylenedioxythiophene) counter electrode in dye-sensitized solar cells," *Journal of Photochemistry and Photobiology A*, vol. 164, no. 1–3, pp. 153–157, 2004.
- [9] N. Fukuri, Y. Saito, W. Kubo et al., "Performance improvement of solid-state dye-sensitized solar cells fabricated using poly(3,4-ethylenedioxythiophene) and amphiphilic sensitizing dye," *Journal of the Electrochemical Society*, vol. 151, no. 10, pp. A1745–A1748, 2004.
- [10] J. Han, Y. Liu, and R. Guo, "A novel templateless method to nanofibers of polyaniline derivatives with size control," *Journal of Polymer Science Part A*, vol. 46, pp. 740–746, 2008.
- [11] F. D. R. Amado, L. F. Rodrigues, M. M. C. Forte, and C. A. Ferreira, "Properties evaluation of the membranes synthesized with castor oil polyurethane and polyaniline," *Polymer Engineering and Science*, vol. 46, no. 10, pp. 1485–1489, 2006.
- [12] I. Sapurina, A. Riede, and J. Stejskal, "In-situ polymerized polyaniline films: 3. Film formation," *Synthetic Metals*, vol. 123, no. 3, pp. 503–507, 2001.

- [13] A. U. H. A. Shah and R. Holze, "Spectroelectrochemistry of two-layered composites of polyaniline and poly(o-aminophenol)," *Electrochimica Acta*, vol. 53, no. 14, pp. 4642–4653, 2008.
- [14] P. R. Solanki, S. Singh, N. Prabhakar, M. K. Pandey, and B. D. Malhotra, "Application of conducting poly(aniline-co-pyrrole) film to cholesterol biosensor," *Journal of Applied Polymer Science*, vol. 105, no. 6, pp. 3211–3219, 2007.
- [15] A. Tiwari and S. Gong, "Electrochemical synthesis of chitosan-co-polyaniline/WO₃·n₂O composite electrode for amperometric detection of NO₂ gas," *Electroanalysis*, vol. 20, no. 16, pp. 1775–1781, 2008.
- [16] P. R. Solanki, N. Prabhakar, M. K. Pandey, and B. D. Malhotra, "Nucleic acid sensor for insecticide detection," *Journal of Molecular Recognition*, vol. 21, no. 4, pp. 217–223, 2008.
- [17] H. Ding, C. Zhu, Z. Zhou, M. Wan, and Y. Wei, "Hydrophobicity of polyaniline microspheres deposited on a glass substrate," *Macromolecular Rapid Communications*, vol. 27, no. 13, pp. 1029–1034, 2006.
- [18] R. Singhal, A. Chaubey, K. Kaneto, W. Takashima, and B. D. Malhotra, "Poly-3-hexyl thiophene langmuir-blodgett films for application to glucose biosensor," *Biotechnology and Bioengineering*, vol. 85, no. 3, pp. 277–282, 2004.
- [19] Q. Qin, J. Tao, Y. Yang, and X. Dong, "In situ oxidative polymerization of polyaniline counter electrode on ITO conductive glass substrate," *Polymer Engineering and Science*, vol. 51, no. 4, pp. 663–669, 2011.
- [20] A. Malinauskas, "Chemical deposition of conducting polymers," *Polymer*, vol. 42, no. 9, pp. 3957–3972, 2001.
- [21] M. Trchová, I. Šeděnková, E. Tobolková, and J. Stejskal, "FTIR spectroscopic and conductivity study of the thermal degradation of polyaniline films," *Polymer Degradation and Stability*, vol. 86, no. 1, pp. 179–185, 2004.
- [22] M. Khalid and F. Mohammad, "Preparation, FTIR spectroscopic characterization and isothermal stability of differently doped fibrous conducting polymers based on polyaniline and nylon-6,6," *Synthetic Metals*, vol. 159, no. 1-2, pp. 119–122, 2009.
- [23] T. Prabhakaran and J. Hemalatha, "Synthesis and characterization of magnetoelectric polymer nanocomposites," *Journal of Polymer Science, Part B*, vol. 46, no. 22, pp. 2418–2422, 2008.
- [24] C. Zhou, J. Han, G. Song, and R. Guo, "Fabrication of poly(aniline-co-pyrrole) hollow nanospheres with triton X-100 micelles as templates," *Journal of Polymer Science, Part A*, vol. 46, no. 11, pp. 3563–3572, 2008.
- [25] S. Zhou, T. Wu, and J. Kan, "Effect of Co²⁺, Ni²⁺, Cu²⁺, or Zn²⁺ on properties of polyaniline nanoparticles," *Journal of Applied Polymer Science*, vol. 106, no. 1, pp. 652–658, 2007.
- [26] L. Yan and W. Tao, "Synthesis of achiral PEG-PANI rod-coil block copolymers and their helical superstructures," *Journal of Polymer Science, Part A*, vol. 46, no. 1, pp. 12–20, 2008.
- [27] X. Lei and Z. Su, "Conducting polyaniline-coated nano silica by in situ chemical oxidative grafting polymerization," *Polymers for Advanced Technologies*, vol. 18, no. 6, pp. 472–476, 2007.
- [28] M. Kraljić, Z. Mandić, and L. Duić, "Inhibition of steel corrosion by polyaniline coatings," *Corrosion Science*, vol. 45, no. 1, pp. 181–198, 2003.